Sound generation by coherent structures in mixing layers

Ge Song

2012-ENAM-0024

École doctorale n° 432 : Science des Métiers de l'Ingénieur

Doctorat ParisTech

T H È S E

pour obtenir le grade de docteur délivré par

l'École Nationale Supérieure d'Arts et Métiers

Spécialité " Acoustique "

présentée et soutenue publiquement par

Ge SONG

le 10 juillet 2012

Sound generation by coherent structures in mixing layers

Directeur de thèse : **Jean-Christophe ROBINET**
Co-encadrement de la thèse : **Xavier GLOERFELT**

Jury

M. Yves GERVAIS, Professeur à l'institut PPRIME, Poitiers	Président
M. Christophe AIRIAU, Professeur à l'université de Toulouse	Rapporteur
M. Christophe BOGEY, Chargé de Recherche au CNRS, LMFA, Lyon	Rapporteur
M. Laurent CORDIER, Chargé de Recherche au CNRS, l'institut PPRIME, Poitiers	Examinateur
M. Lutz LESSHAFFT, Chargé de Recherche au CNRS, LadHyx, Paris	Examinateur
M. Jean-Christophe ROBINET, Professeur, DynFluid, ENSAM PARIS	Directeur
M. Xavier GLOERFELT, Maître de Conférences, DynFluid, ENSAM PARIS	Co-directeur

T H È S E

Arts et Métiers ParisTech - Centre de Paris
Laboratoire DynFluid

Contents

Chapter 1

Introduction

A mixing layer is formed by bringing two streams of fluid, moving at different velocities U_1 and U_2, together downstream of a splitter plate, as sketched in figure 1.1. Such a flow configuration is generally considered as a prototype of free shear flows which occur in a very broad spectrum of applications from natural phenomena to the engineering science, such as internal flows in propulsion and combustor system (figure 1.2). Because of viscous diffusion a shear occurs between the two streams giving rise to an inflectional velocity profile. Following the hydrodynamic stability theory (Lin [69] and Drazin & Reid [37]), this velocity profile is known to be unstable relative to small perturbations through the Kelvin-Helmholtz (K-H) instability mechanism: waves are generated as they travel downstream leading to the formation of large spanwise vortex structures. The process in which interaction between neighbouring vortices results in the formation of a larger vortex was referred to as *vortex pairing*, and has been experimentally observed to govern the streamwise growth of the mixing layer (Winant & Browand [121]). Furthermore, these organized quasi-two-dimensional structures were observed not only in laminar flows but also in turbulent flows where they coexisted with fine-scale motions, as pictured in figure 1.3. They have been generally acknowledged to be an intrinsic feature of free shear layers. The so-called *coherent structures* have been extensively documented by numerous researchers (Crow & Champagne [34], Brown & Roshko [25], Winant & Browand [121], Browand & Weidman [24], among others). The discovery of quasi-ordered coherent structures has changed our trend of thought about turbulence which was previously viewed as a random process, which could be treated by a stochastic approach. After recognition of the paramount role of large structures with a long coherence length in free shear flows, traditional stochastic methods seemed incapable of determining totally the characteristics of these structures. Some researchers chose to rest upon classical hydrodynamic stability theory to study these flow structures in the downstream development. Within this stability approach, large-scale vortical structures were conceptualized as a superposition of several instability waves of different frequency in Fourier space. The goal was to reveal the downstream evolution of these spatially growing waves (Ho & Huerre [52]). Two distinct approaches have traditionally been adopted in the linear stability problems: spatial and temporal approach. The so-called spatial stability approach in which the behaviours of spatially (complex wavenumber and real frequency) growing perturbations were determined, has been chosen by

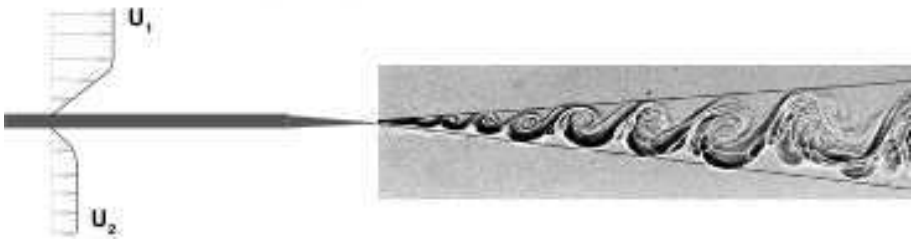

Figure 1.1: Sketch of a spatially developing mixing layer (Brown & Roshko [25]).

Michalke ([75], [76]) and Monkewitz & Huerre [79], to determine numerically the temporal and spatial inviscid instability characteristics of a hyperbolic-tangent velocity profile which is a good approximation of a shear layer. The spatial approach has been reasonably successful in describing the spatial evolution of vortical structures in forced experiments and seemed more adapted to a comparison with experiments. Such a behaviour was also observed for a spatially developing boundary layer. For example, in the experiments of Schubauer & Skramstad [102], the form of the perturbation created by an oscillating ribbon, thus a real frequence, suggested a spatial evolution of the perturbation. On the other hand, as demonstrated by Michalke [75], [76], Freymuth [40] and Huerre & Monkewitz [55], the temporal (real wavenumber and complex frequency) approach dealing with the temporal evolution of an initial perturbation in the flow failed to describe the forced instability waves in mixing layers.

1.1 From Amplifiers to oscillators

Crow & Champagne [34] were the first to discover that the shear layer of a jet operated as a finely tuned amplifier of upstream perturbations. The sensitivity of the shear layer to initial conditions has been subsequently studied by varying the excitation frequency (Ho & Huang [51]). They have also shown that the vortex merging could be manipulated by forcing the flow with a very low-level near a subharmonic of the most-amplified frequency according to a linear stability analysis. Indeed, this observed strong sensitivity of the evolution of the flow structures to outside disturbances is associated with the noise amplifier characteristics of the flow. The power spectrum of a measured signal is generally broadband in the flow which displays extrinsic dynamics. Otherwise, the flow can behave as an oscillator characterized by a well-defined frequency that is insensitive to external low-level noise. Thus, they display intrinsic dynamics. For example, co-flowing mixing layers and homogeneous jets belong to the former class of flow whereas counterflow mixing layers, bluff-body wakes and hot jets are known to be prototypes of oscillator-type flows (see Huerre & Monkewitz [57], Huerre [54]). In order to describe these two distinct qualitative nature of open flow dynamical behaviours, the concepts of convective and absolute instabilities, first introduced in the context of plasma physics by Briggs [23] and Bers [13], were developed in fluid mechanics by Huerre & Monkewitz [56]. These two instability categories can be distinguished by characterizing the impulse flow response localized in space and time of an open flow within the parallel-flow ap-

(a)

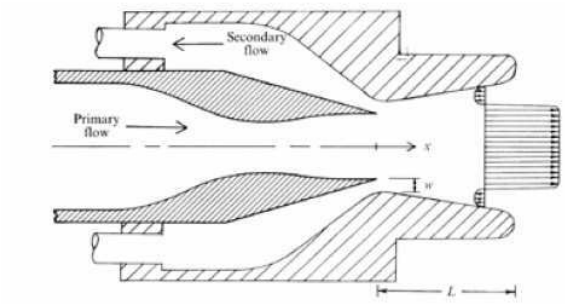

(b)

Figure 1.2: (a) Kelvin-Helmholtz vortices in a cloud. (b) Internal mixing layer flow in a propulsion system.

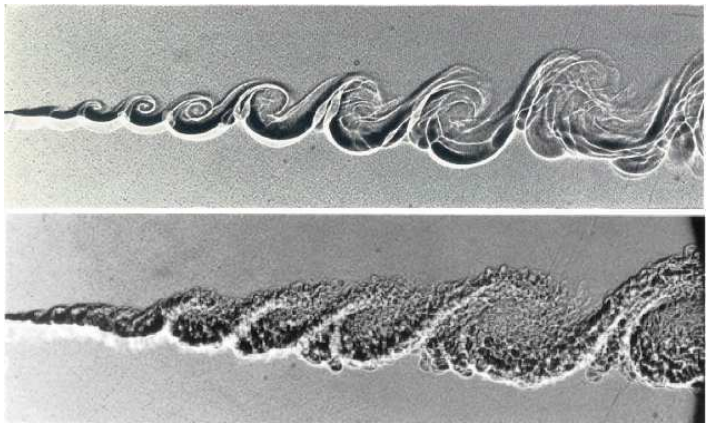

Figure 1.3: Large-scale coherent structures in a laminar and turbulent mixing layer at the top and bottom (experiments by Brown & Roshko [25]).

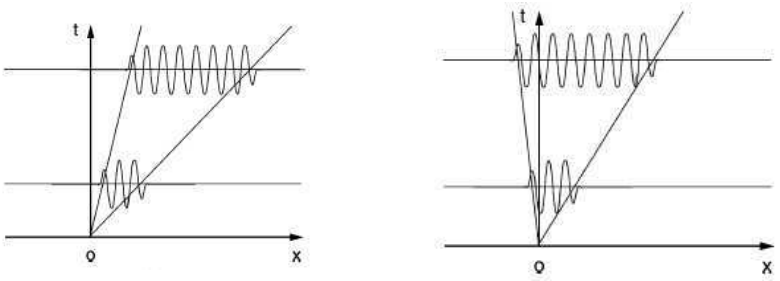

(a) (b)

Figure 1.4: Space-time wavepacket evolution, according to (a) convective instability; (b) absolute instability (Chomaz [27]).

proximation locally at each streamwise station. If perturbations taking the form of a wavepacket is advected and amplify in time along the flow direction, the velocity profile is said to be locally convectively unstable. In absence of continued disturbance, the flow relaxes back to its initial state. A convectively unstable flow behaves then as a noise amplifer. By contrast, perturbations can spread throughout until the entire flow field is contaminated. The velocity profile is said to be locally absolutely unstable. The flow behaves then as an oscillator. The strict definition of convective/absolute instability for parallel open flows can be found in Huerre & Monkewitz [57]. The distinction is highlighted in figure 1.4, in which we observe two different behaviours of wavepacket according to the sketches of typical impulse responses in space and time. Within this context, Lesshafft [64] has studied a hot jet flow that is absolutely unstable when the inlet shear layer is sufficiently thick and strongly heated. He has highlighted the onset of highly periodic oscillatory state in an asymptotic regime by DNS (see figure 1.5). The synchronized asymptotic state is also demonstrated in the spatio-temporal diagram in figure 1.6. It is worth noting that the flow gives rise to a vortex pairing near the inlet even without the continued external forcing caused by the absolutely unstable pocket at the inflow. Given the above discussions, we may remark that, even though a shear flow such as a mixing layer presented a very simple configuration, the spatio-temporal behaviour of perturbations is a relatively complex phenomenon depending on a wide range of parameters, such as the shear layer thickness, the heating and degree of the shear.

1.2 Understanding of coherent structures by the stability theory

It should be mentioned that the above linear stability theory is cast under the parallel-flow assumption. That is, base flows are invariant with respect to translations in the streamwise x direction. However, most of shear flows are not uniform in x direction, and the base flow thickness θ increases with the downstream distance. The generalization to slowly diverging flows with small spreading rate $d\theta/dx = O(\varepsilon)$, where $\varepsilon \ll 1$ was first proposed by Crighton & Gaster

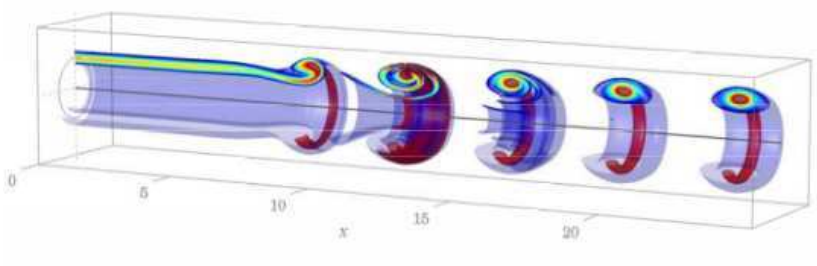

a) $R/\theta = 10$, $S = 0.4$

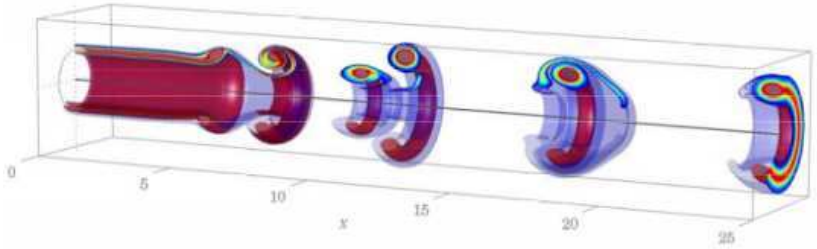

b) $R/\theta = 20$, $S = 0.6$

Figure 1.5: Snapshots of synchronized oscillations in two absolutely unstable jets: (a) no vortex pairing inside the thick shear layer jet (R/θ and S refer to the shear layer thickness of the inlet profile and ambien-to-jet temperature ratio, respectively); (b) vortex pairing inside the thin shear layer jet (Lesshafft [64]).

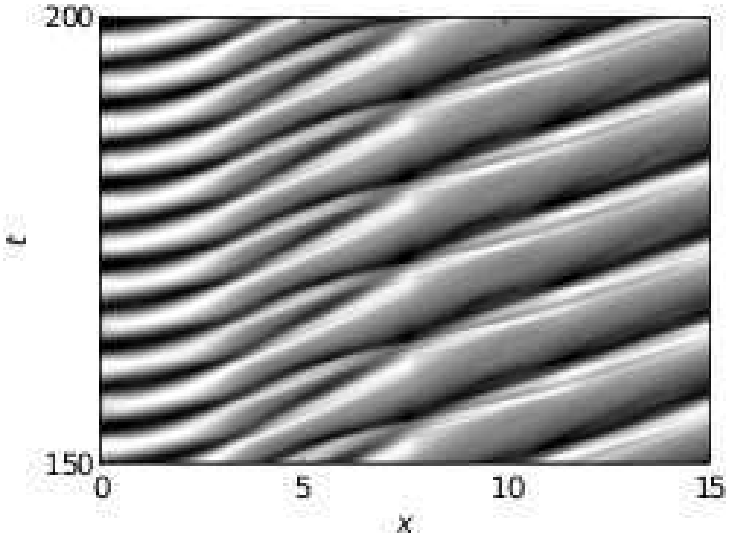

Figure 1.6: Spatio-temporal diagrams of the radial perturbation velocity $v(r = 1, x, t)$ in the long-time regime for the absolutely unstable case $R/\theta = 25$, $S = 0.55$ (Lesshafft [64]).

[32] within a Wentzel-Kramers-Brillouin-Jeffreys (WKBJ) approach. The base flow becomes $U_b(y;\theta(X))$ and changes over a slow space scale $X = \varepsilon x$. We can note that the WKBJ formulation has been afterwards applied satisfactorily to boundary layers (Bouthier [21]), jets (Crighton & Gaster [32]) and mixing layers (Gaster, Wygnanski & Kit [41]). Furthermore, these non-parallel flow corrections have been confirmed by the advancements in computing power and the algorithms in the seventies. Later, a new numerical method emerged in the middle of the eighties, clever and little expensive, which consisted of transforming the solutions of the stability equations to an evolution in space, calculated by a simple marching procedure in x, commonly called Parabolized stability equations (PSE) (Herbert & Bertolotti [50]). In addition, this approach authorized a detailed and efficient understanding of the linear and nonlinear effects, combined with a weakly non-parallel correction (Bertolotti [14]). Henceforth, the PSE has been used in numerous relevant studies of mixing layer dynamics. More recently, Day, Mansour & Reynolds [36] used this technique to examine the structure and stability of compressible reacting mixing layers. Cheung & Lele [26] have investigated linear and nonlinear processes in mixing layer dynamics and acoustic radiation through the linear and nonlinear PSE.

These stability theories, first valid for strictly parallel flows, and then were subsequently extended to the weakly non-parallel flows. The perturbation envelope was thus weakly dependent on x. As a result, the stability problem defined an eigenvalue problem where the two directions x and y were considered as the eigendirections. With the help of a WKBJ development of the solution, Chomaz, Huerre & Redekopp [29] have established that the existence of a pocket of local absolute instability was a necessary, but non sufficient condition, of a global instability appearance. This implies an intrinsic dynamics of the flow, imposing the formation of coherent structures at the frequency of the global instability. Here, the term *global* refers to the instability of the entire flow field. Such self-sustained states are described by the so-called *global modes* taking the following form (Chomaz, Huerre & Redekopp [29] and Monkewitz, Huerre & Chomaz [80])

$$\mathbf{q} = \hat{\mathbf{q}}\,(X, y)\, e^{-i\omega_G t}$$

The associated dynamical structures are the global modes $(\hat{\mathbf{q}}, \omega_G)$. The complex vector field $\hat{\mathbf{q}}$ characterize their spatial structures whereas the temporal behaviour is described by the complex global frequency ω_G. For instance, this frequency has been successively predicted for a weakly-non-parallel shear flow through a global linear stability analysis (Monkewitz, Huerre & Chomaz[80]). Also Pier [91] has discussed the fundamental criterion regarding the frequency selection of global modes in cylinder wakes.

1.3 Noise sources of mixing layers

Because coherent structures are considered as a manifestation of instability waves developing in fluid flows, the understanding of emergence of these structures have been thus studied finely by the stability analyses. However, the question of whether these coherent structures in form of instability waves had a sizable effect on the downstream evolution of the shear layer and the resulting acoustic radiation was not addressed until the seventies. Bishop, Ffowcs

Williams & Smith [15] discovered that the main noise sources of the high-speed jets were very large-scale wave-like undulations of the jet flow. Later, Liu [70] has modelled these large-scale instabilities by decomposing the total flow into three components: the time-dependent mean flow, the instability wave and the fine-scale turbulence. The development of waves could then be described through a shape assumption: the amplitude was determined by the energy equation; the shape function and local characteristics were obtained from the local linear stability theory. The role of shear-layer instability waves in mixing layer and jet noise was also examined by Moore [82]. In his study, coherent structures present in a subsonic jet were shown to govern the production of the turbulent fluctuations that radiate broad-band jet noise. He noted that forcing the shear layer at specific frequencies with a fluctuating pressure of only 0.08% of the jet dynamics head might increase the noise over the whole subsonic Mach number range. Furthermore, most of his flow features agreed well with the linear inviscid instability theory. One year later, the importance of large-scale coherent structures of jet as a noise source were assessed by Ffowcs Williams & Kempton [120]. They proposed two models of the acoustic sources in a turbulent jet: the first model referred to the instability waves that initially growed but eventually saturated and decayed. This wave model has been shown to be able to increase the radiated broad-band noise of a jet by forcing at one frequency. The second model relating to the sudden pairing of eddies supported the idea that the vortex pairing could be the mechanism primarily responsible for the jet noise production. Inspired by the work of Crighton & Gaster [32] in which they developed methods to model the growth of instability waves in a slowly diverging jet flow through the multiple-scales expansion method, Tam & Morris [113] demonstrated that the linear stability solution could be extended into the far field to calculate the noise radiation associated with the instability waves. In an attempt to construct a uniformly valid instability wave solution inside and outside the jet. Tam & Burton [110], [111] then used the method of matched asymptotic expansions. The resulting solution revealed that the sound generation mechanism in high-speed supersonic mixing layers was associated with the Mach wave radiation generated by the large turbulence structures/instability waves of the flow. From that time, it is well-established that in Mach wave radiation, the instability wave is directly coupled to the acoustic field. It is worth noting that all of these analyses cited above dealt with the high-speed supersonic mixing layers or jets and were restricted to the direct sound radiation of linear instability waves.

Nevertheless, the role of coherent structures/instability waves in the sound radiation are less established. It was in 1964 that Powell [92] showed the vortex pairing radiated sound with the quadrupole signature of jet noise, and Winant & Browand [121] have suggested that the vortex pairing was the mechanism primarily responsable for the jet noise generation. Then Ffowcs Williams & Kempton [120] have proposed modelling the jet as a series of eddies that convected downstream at a constant subsonic speed until they merged in pair and then continued convecting downstream. Their vortex-pairing model have been shown to support satisfactorily the vortex pairing mechanism suggested earlier by Winant & Browand [121]. Later, Kibens [61] observed the natural broadband noise of the jet to be suppressed and important radiated sound at the subharmonic frequencies by exciting a circular jet at the most amplified frequency of the shear layer instability. He also identified the stationary sources inside the jet

with the vortex pairing locations. Laufer & Yen [63] found that the stationary acoustic sources were associated with the nonlinear saturation of the unstable wave amplitudes of the shear layer at the vortex pairing locations. The corresponding acoustic radiation varied nonlinearly with the source strength and was highly directional and exponential. This was later confirmed by the observations of Bridges & Hussain [22]. It is thus shown that the noise characteristics of subsonic flows are quite different from their supersonic counterparts.

1.4 Computational aeroacoustics

Previously, we have seen that the emergence of the coherent structures in shear flows could be understood by the stability calculations. The correct description of these structures in the fluid flows can be accomplished in two ways: direct computations or reduced-order models (or acoustic analogy for compressible flows). As discussed by Lighthill [67], direct computations of aerodynamic sound generation can be widely divided into three categories: the first computes only the near-field region and subsequently an acoustic analogy is solved to obtain the acoustic field; the second computes the near-field region and a small extent of the acoustic region, the acoustic far-field is determined by solving the wave equation in the exterior domain given boudary data from the near field: and the third computes both the near field and an important portion of the acoustic field by solving the compressible Navier-Stokes equations in both regions. In particular, owing to the time-dependent characteristics of the aeroacoustic problems, several computational challenges of the Computational aeroacoustics (CAA) arose with respect to the third category [109]: the very short wavelengths of the high frequency waves; the extremely small amplitudes of the acoustic waves relative to the mean flow; computational schemes must have minimal numerical dispersion and dissipation; and radiation and outflow boundary conditions must be imposed at the artificial exterior boundaries to assist the waves to exit smoothly and avoid the reflection of outgoing sound waves back into the computation domain and thus the contamination of solution. Thanks to significant advances in CAA algorithms, the latter have been applied to several interesting noise prediction problems. For example, for supersonic flows, Mitchell, Lele & Moin [78] computed the Mach wave radiation in an axisymmetric supersonic jet. Freund, Lele & Moin [39] have performed the DNS of a Mach number 1.92 supersonic turbulent jet to investigate its radiated sound field (see figure 1.7 (a)). In the context of subsonic regime, Colonius, Lele & Moin [30], Bogey, Bailly & JuvÃ© [20] and Mitchell, Lele & Moin [77] have investigated sound generated by vortex pairing in a two-dimensional compressible mixing layer and a co-rotating vortex pair by using the direct numerical simulations (DNS). Besides, large eddy simulation (LES) of a subsonic laminar jet performed by Bogey & Bailly [19] is shown in figure 1.7 (b)). It should be mentioned that there exist numerous noise sources in a turbulent jet, such as mixing noise and breakdown of coherent structures at the end of potential core for subsonic jets, and broadband shock-associated noise and screech tones in imperfectly expanded supersonic jets (see the review by Tam [108]). In the present discussion, we focus on the sources in the shear layer developing just after the nozzle exit. From the previous numerical simulations, two different mechanisms of sound generation in mixing layers are clearly illustrated and contrasted: Mach

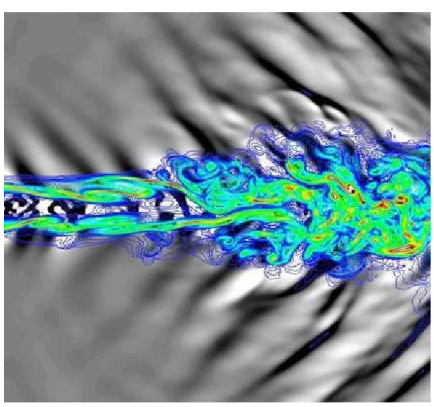

(a)

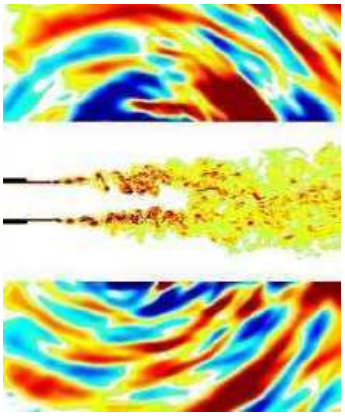

(b)

Figure 1.7: (a)DNS of a Mach 1.92 turbulent perfectly expanded jet and its sound radiation (Freund, Lele & Moin [39]). (b) LES of a subsonic laminar jet (Bogey & Bailly [19]).

wave radiation and vortex pairing sound (figure 1.7).

1.5 Modal decompositions

Nevertheless, the accurate description of coherent structures in two or three dimensions requires a large number of degrees of freedom, yielding a high-dimensional dynamical system representing the complex flow phenomena occurred over the wide range of scales in both space and time. Solving such problems by direct methods can become a prohibitively expensive computational task. Therefore, in practice, the identification of dominant structures are often achieved by decomposing them into modes that are representative of the principal flow dynamics. The dynamics is thus projected onto a low-dimensional subspace with significantly fewer degrees of freedom. Within a linear approach, global eigenmodes with respect to the linearized dynamics can be used to describe the underlying physical mechanisms (Bagheri *et al.* [8]). Furthermore, the role of global modes in the acoustic radiation has been studied for globally stable flows. For instance, Lesshafft [64] have investigated the acoustic field associated with the global mode in a hot jet. Nichols & Lele [85] have examined the sound generated by a superposition of global modes in a cold supersonic jet. They have identified a mechanism of transient growth with a propagating aerodynamic wavepacket which radiated an acoustic wavepacket to the far field. The emission of an acoustic wavepacket is illustrated by plotting the snapshots of the optimal transient response, as shown in figure 1.8. The most common method remains is the Proper Orthogonal or Karhunen-Loève Decomposition (POD), first introduced in the context of turbulence by Lumley [72] (see also Holmes, Lumley, & Berkooz [53]). This method consisting of extracting *modes* or *empirical eigenfunctions* that contain the highest kinetic energy on average provides an optimal subspace in the sense that the error in the projection onto

the subspace is minimized. A reduced-order model (ROM) can be obtained by Galerkin projection of the governing equations onto the optimal POD subspace. This stragegy has been applied to different variety of flow situations. From the early work of Lumley [72], Sirovich [104], Aubry *et al.* [3], Rajaee, Karlsson & Sirovich [93] and Ukeiley *et al.* [117] in incompressible regime to the more recent studies undertaken by Rowley, Colonius & Murray [96] and Gloerfelt [43] in a compressible regime, these works have formed the basis for explaining the dynamics of the predominant coherent structures in boundary layer, mixing layer and cavity flow dynamics through the POD technique and further constitute a reduced-order model based on global and POD modes. Another important perspective concerns flow control applications, where the low-dimensional models have been incorporated into flow control strategies, (see Bergman, Cordier & Brancher [12] for flow around a cylinder wake, and Barbagallo, Sipp & Schimid [9] for the closed-loop control of an open cavity flow). However, we may point out a principal disadvantage which is linked to the flow structures hierarchy in term of energy representation (Noack *et al.* [86], Schmid [100]). More recently, Schmid & Sesterhenn [101] and Rowley *et al.* [97]) have proposed an alternative tool to POD by decomposing the flow into *Koopman modes* or *dynamic modes* to describe the global behaviour of complex nonlinear flows. This technique is based on the spectral analysis of a linear Koopman operator defined for any nonlinear dynamical systems [73], and referred to as *Dynamic Modes Decomposition*. This technique may be viewed as a nonlinear generalization of global eigenmodes of a linearized system (Rowley *et al.* [97]). Since then, the DMD has been applied to various fluid flows both numerically and experimentally (Rowley *et al.* [97], Schmid [100] and Schmid *et al.* [98]). From these evidences, the DMD algorithm has been proven as a reliable algorithm to extract spatio-temporal coherent structures from a sequence of data. Moreover, in the investigation of the jet in crossflow for example (Rowley *et al.* [97]), the Koopman modes seemed to capture the relevant frequencies more accurately than global eigenmodes of the linearized dynamics, and decoupled the different frequency components more effectively than modes determined by POD.

1.6 Acoustic analogy for sound prediction

Concerning the far-field sound prediction, another efficient way is the use of acoustic analogy. It should be mentioned that earlier studies of the sound generated aerodynamically, that is, sound radiated from a fluid flow, have been used to explain the production of frequencies in the flow by instability. It was not until 1952 that Lighthill [65], [66] first proposed an acoustic analogy approach to explain the behaviour of jet mixing noise. In this theory, he rearranged the compressible equations of motion of gas into the form of a linear wave propagation for a medium at rest with a quadrupole-type source term. The mixing region is then replaced by a distribution of the acoustic sources. The original Lighthill's equation did not take into consideration of the mean flow interaction effects, that is why Phillips [90], Lilley [68], and many others sought to improve this by rearraging the Navier-Stokes equations into the form of an inhomogeneous convective, or moving-medium, wave equation (Goldstein [47]). To take into account for the effects of solid boundaries, the acoustic analogy was then extended by Curle [35] and Ffowcs Williams & Hawkings (FW-H)

[119]. The acoustic solution can be basically obtained through an appropriate acoustic analogy using near-field source terms calculated from DNS calculation (e.g. Bogey [17]). However, we can mention that Cheung & Lele [26] combined the instability wave solution (PSE in their case) with the Lilley-Goldstein acoustic analogy and their predicted far-field sound showed a good agreement with the direct calculation. Kierkegaad *et al.* [62] were the first to use global modes rather than the entire flow field to calculate the acoustic field through the Curle's equations on a two-dimensional flow over a cavity with smoothed corners. Therefore, we believe that using this combined model-acoustic analogy approach makes the computational effort significantly less expensive.

1.7 Proposed approach

All of studies cited previously underline the necessity of performing a global stability analysis to understand the emergence of the fundamental frequencies in the underlying fluid flow as well as a modal decomposition within both a linear and a nonlinear framework to characterize the coherent structures primarily responsable for the sound generation. The development of tools to analyse and understand the emergence of coherent structures associated with the noise production remains a fundamental issue in the fields of aeroacoustics. Thus, in the context of this thesis, we propose to develop the methods of global stability with respect to the compressible flows as well as a technique of calculation of coherent structures applied to the nonlinear regimes based upon the DMD method. In order to validate and illustrate the relevance of these tools, we consider a co-flowing mixing layer, a typical noise amplifer, from a very simple case where a single source is implicated in the far-field acoustic radiation to a more complex case where two sources are present. We can emphasize that these tools developed during this thesis may be applied to the more general flow case without any assumptions about the parallelism.

1.8 Outline

The organization of this thesis is as follows. Chapter 2 gives a description of flow parameters and the implementation of the nonlinear disturbance governing equations. The numerical methods for computational aeroacoustics used to compute the mixing layer directly, algorithms for extracting global and Koopman modes as well as the convected FW-H equations in the acoustic analogy approach are also presented. In chapter 3, the sound generated by only one single vortex pairing in a mixing layer is investigated, as depicted in figure 1.9. The results through the direct calculations, global modes stability within the linear framework are presented, followed by a DMD analysis in a nonlinear approach. Finally, the combined DMD-acoustic analogy is shown. Chapter 4 considers the double vortex pairings case, as represented in figure 1.10. The sound computed from DNS and DMD are provided and contrasted. Chapter 5 contains a discussion of important conclusions from this work, followed by recommendations for future work on the mixing layer noise problem.

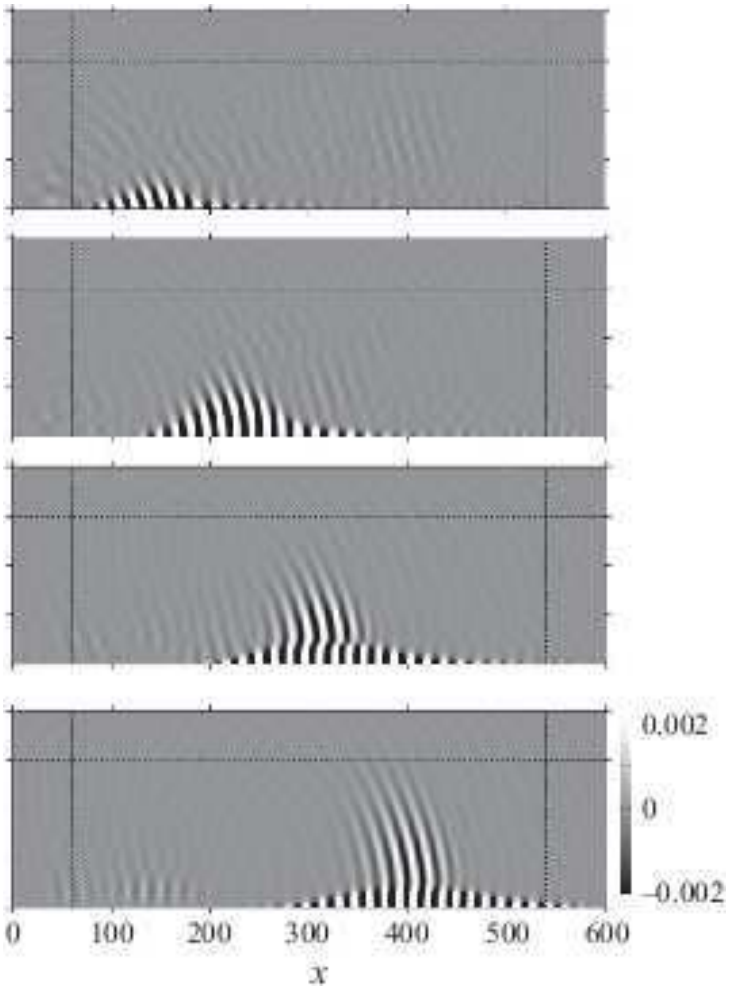

Figure 1.8: Snapshots of the superposition of global modes for the supersonic jet. An acoustic wavepacket detaches from the jet between the second and third frames (Nichols & Lele [85]).

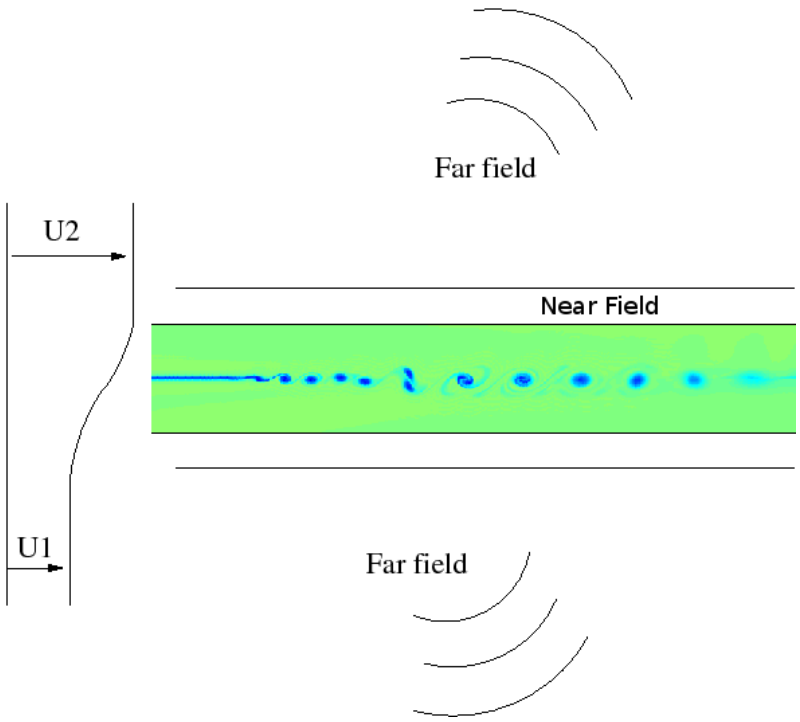

Figure 1.9: Schematic representation of a compressible forced mixing layer: one single pairing case.

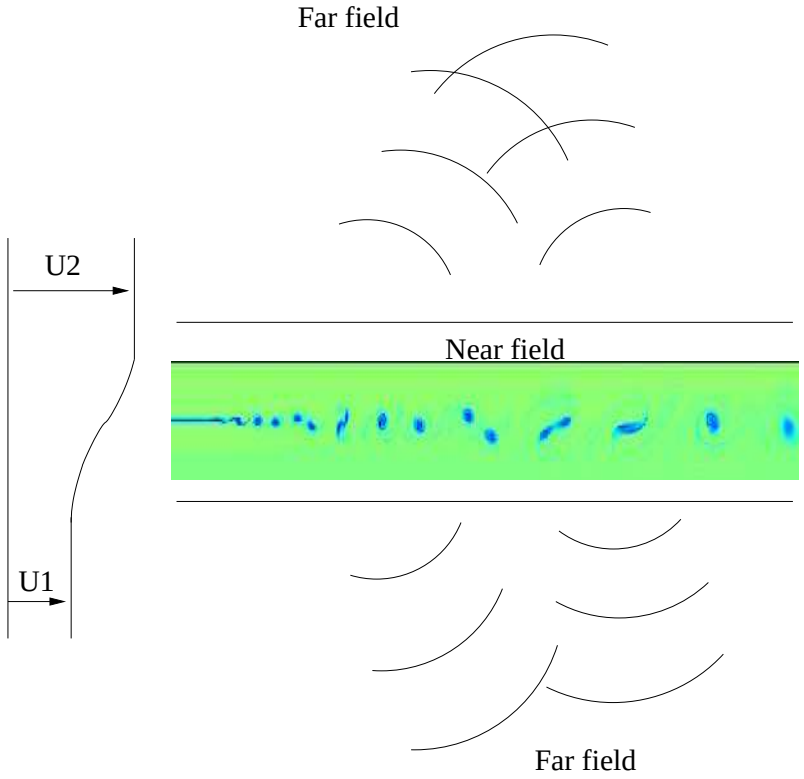

Figure 1.10: Schematic representation of a compressible forced mixing layer: double pairing case.

Chapter 2

Numerical Methods

In this chapter, we provide a detailed description of numerical methods and algorithms that will be used during the next parts of this thesis. During this thesis, starting from an existing homemade Navier-Stokes solver, i have developed two perturbative versions in two and three dimensions for the investigation of the aeroacoustics of subsonic mixing layers. The code is based on the perturbation equations that govern the temporal evolution of the fluctuating quantities and are obtained by substracting the Navier-Stokes equations written in terms of a certain base flow from the same equations in terms of total flow variables. Performed in this way, the perturbations are obtained directly.

2.1 Flow configuration

We consider the example of the hyperbolic-tangent mixing layer periodic in the spanwise direction, as shown in figure 2.1, which is a legitimately accurate representation of the mean velocity profiles. For compressible forced mixing layer, it is common to divide the domain into a near-field region, where the aerodynamics is dominant, and a far-field region, where the acoustics is to be established. In addition, the base flow is given by:

$$u_b(y) = \frac{U_1 + U_2}{2} + \frac{U_2 - U_1}{2} \tanh\left(\frac{2y}{\delta_\omega(0)}\right) \tag{2.1}$$

where U_1 and U_2 are the speeds in the lower and upper streams, with vorticity thickness $\delta_\omega(x)$ characterizing the growth of the shear layer by measuring locally the vorticity thickness

$$\delta_\omega(x) = \frac{\Delta U}{|(\partial U/\partial y)|_{max}} \tag{2.2}$$

where $\Delta U = U_2 - U_1$ is the velocity difference across the layer. A compressible mixing layer is characterized by two flow parameters: U_c and M_{c_i} (Papamoschou & Roshko [88]). In general, U_c is the velocity of the dominant waves and structures. In mixing layers, it is related to the large vortex structures in the flow.

$$U_c = \frac{c_2 U_1 + c_1 U_2}{c_1 + c_2} \tag{2.3}$$

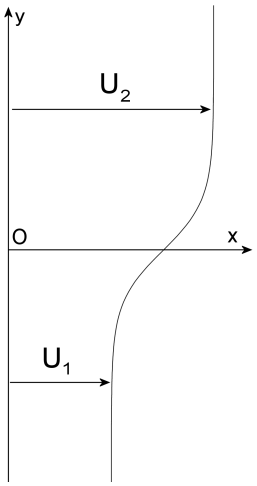

Figure 2.1: Schematic representation of the velocity profile for a mixing layer.

where the speeds of sound in the upper and lower streams are denoted by c_1 and c_2. By assuming the equality of speeds of sound $c_1 = c_2 = c_\infty$ and temperature in the two free streams, we have

$$U_c = \frac{U_1 + U_2}{2} \tag{2.4}$$

For a compressible flow, the convective Mach numbers in either of the two streams can be defined as follows

$$M_{c_i} = \frac{U_i - U_c}{c_i} \tag{2.5}$$

where $i = 1, 2$. In the same way, the global convective Mach number is then deduced

$$M_c = \frac{\Delta U}{2c_\infty}$$

The Reynolds number based on the initial vorticity thickness $\delta_\omega(0)$ and the net shear ΔU, is defined as

$$Re_{\delta_\omega(0)} = \frac{\Delta U \delta_\omega(0)}{\nu} \tag{2.6}$$

where ν denotes the kinematic viscosity which is taken to be constant.

2.2 Equation of motion

The full three-dimensional compressible Navier-Stokes equations along with the perfect gas equation of state are used as a mathematical model to describe the dynamic behaviour of the mixing layer. The governing equations in conservative form may be written in the vector form

$$\frac{\partial \mathbf{U}}{\partial t} + \frac{\partial \mathbf{E_e}}{\partial x} + \frac{\partial \mathbf{F_e}}{\partial y} + \frac{\partial \mathbf{G_e}}{\partial z} - \frac{\partial \mathbf{E_v}}{\partial x} - \frac{\partial \mathbf{F_v}}{\partial y} - \frac{\partial \mathbf{G_v}}{\partial z} = 0 \tag{2.7}$$

The conservative variable vector is given by

$$\mathbf{U} = \begin{pmatrix} \rho \\ \rho u \\ \rho v \\ \rho w \\ e \end{pmatrix}$$

where ρ is the fluid density and u, v, w are the velocity components in the three directions, respectively. The total energy per unit volume of fluid is defined as

$$e = \rho[C_v T + \frac{1}{2}(u^2 + v^2 + w^2)] = \frac{p}{\gamma - 1} + \frac{1}{2}\rho(u^2 + v^2 + w^2) \qquad (2.8)$$

where p, T, c_v and γ are the pressure, temperature, specific heat at constant volume and specific ratio, respectively. The ratio of specific heats $\gamma = c_p/c_v$ is taken to be 1.4 in all computations. Note that, in (2.8), the ideal gas law $p = \rho r T$ is used to relate between the thermodynamic variables, where the gas constant r is fixed to 287.06. The specific heat at constant pressure c_p and specific heat at constant volume c_v are defined as $c_v = c_p/\gamma$ and $c_p = r\gamma/(\gamma - 1)$. $\mathbf{E_e}, \mathbf{F_e}$ and $\mathbf{G_e}$ are the inviscid convective fluxes in the three directions, respectively, and are given by

$$\mathbf{E_e} = \begin{pmatrix} \rho u \\ \rho u^2 + p \\ \rho uv \\ \rho uw \\ (e+p)u \end{pmatrix}, \ \mathbf{F_e} = \begin{pmatrix} \rho v \\ \rho uv \\ \rho v^2 + p \\ \rho vw \\ (e+p)v \end{pmatrix},$$

$$\mathbf{G_e} = \begin{pmatrix} \rho w \\ \rho uw \\ \rho vw \\ \rho w^2 + p \\ (e+p)w \end{pmatrix}$$

while $\mathbf{E_v}, \mathbf{F_v}$ and $\mathbf{G_v}$ are the viscous fluxes including both viscous stresses and thermal conduction:

$$\mathbf{E_v} = \begin{pmatrix} 0 \\ \tau_{11} \\ \tau_{12} \\ \tau_{13} \\ u\tau_{11} + v\tau_{12} + w\tau_{13} - q_1 \end{pmatrix}, \ \mathbf{F_v} = \begin{pmatrix} 0 \\ \tau_{21} \\ \tau_{22} \\ \tau_{23} \\ u\tau_{21} + v\tau_{22} + w\tau_{23} - q_2 \end{pmatrix},$$

$$\mathbf{G_v} = \begin{pmatrix} 0 \\ \tau_{31} \\ \tau_{32} \\ \tau_{33} \\ u\tau_{31} + v\tau_{32} + w\tau_{33} - q_3 \end{pmatrix}$$

The viscous stress tensor τ_{ij} for a Newtonian fluid is defined as

$$\tau_{ij} = \mu(\frac{\partial u_i}{\partial x_j} + \frac{\partial u_j}{\partial x_i} - \frac{2}{3}\delta_{ij}\frac{\partial u_k}{\partial x_k})$$

The dynamic viscosity μ is taken to be constant. The heat flux q_i is related to the temperature gradients following the Fourier's law for heat conduction

$$q_i = -k\frac{\partial T}{\partial x_i}$$

where k is the coefficient of thermal conductivity. The Prandtl number is $Pr = \mu c_p/k$, and we assume a constant value of $Pr = 0.723$.

Nonlinear Disturbance equations (NDE) have first been proposed by Morris *et al.* [83] in the CAA methodology application to the prediction of the jet noise. By decomposing the instantaneous flow variable into a mean flow and fluctuating part, they obtained the disturbance equations. In their work, the mean flow are calculated with a Reynolds averaged Navier-Stokes (RANS) solver, and the pertubations quantities are determined directly. This NDE approach has been used rather satisfactorily to calulate the acoustic fields in a supersonic jet or a hot jet (Morris *et al.* [84] and Lesshafft [64]). This perturbative version of the Navier-Stokes allows a better control of the base flow and the investigation of the linear regime by omitting the nonlinear terms in the equations. To investigate the behavior of small perturbations about the base flow, the flow vector $\mathbf{q}$ is decomposed into the steady base flow $\mathbf{q}_b$ and a perturbation component $\mathbf{q}'$

$$\mathbf{q} = \mathbf{q}_b + \mathbf{q}' \tag{2.9}$$

Note that the base flow is frozen throughout the simulation. Substitution of (2.9) into (2.7) results in a set of base flow and perturbation terms. After rearrangement of these terms, the NDE in conservative form can be written as

$$\frac{\partial \mathbf{U}'}{\partial t} + \frac{\partial \mathbf{E_e}'}{\partial x} + \frac{\partial \mathbf{F_e}'}{\partial y} + \frac{\partial \mathbf{G_e}'}{\partial z} - \frac{\partial \mathbf{E_v}'}{\partial x} - \frac{\partial \mathbf{F_v}'}{\partial y} - \frac{\partial \mathbf{G_v}'}{\partial z} = 0 \tag{2.10}$$

where

$$\mathbf{U}' = \begin{pmatrix} \rho' \\ \rho_b u' + \rho' u_b + \rho' u' \\ \rho_b v' + \rho' v_b + \rho' v' \\ \rho_b w' + \rho' w_b + \rho' w' \\ e' \end{pmatrix} \tag{2.11}$$

the convective perturbation fluxes $\mathbf{E_e}', \mathbf{F_e}'$ and $\mathbf{G_e}'$ containing both linear and nonlinear terms are given by

$$\mathbf{E_e}' = \begin{pmatrix} \rho u' + \rho' u_b \\ \rho' {u_b}^2 + 2\rho u_b u' + \rho {u'}^2 + p' \\ \rho(u'v + u_b v') + \rho' u_b v_b \\ \rho(u'w + u_b w') + \rho' u_b w_b \\ u'(e_b + p_b) + u(e' + p') \end{pmatrix}, \mathbf{F_e}' = \begin{pmatrix} \rho v' + \rho' v_b \\ \rho(uv' + v_b u') + \rho' u_b v_b \\ \rho' {v_b}^2 + 2\rho v_b v' + \rho {v'}^2 + p' \\ \rho(wv' + v_b w') + \rho' v_b w_b \\ v'(e_b + p_b) + v(e' + p') \end{pmatrix}, \tag{2.12}$$

$$\mathbf{G_e}' = \begin{pmatrix} \rho w' + \rho' w_b \\ \rho(uw' + w_b u') + \rho' u_b w_b \\ \rho(w'v + w_b v') + \rho' w_b v_b \\ \rho' {w_b}^2 + 2\rho w_b w' + \rho {w'}^2 + p' \\ w'(e_b + p_b) + w(e' + p') \end{pmatrix} \tag{2.13}$$

and the viscous perturbation stresses $\mathbf{E_v}'$, $\mathbf{F_v}'$ and $\mathbf{G_v}'$ are given by

$$\mathbf{E_v}' = \begin{pmatrix} 0 \\ \tau'_{11} \\ \tau'_{12} \\ \tau'_{13} \\ u'\tau'_{11} + v'\tau'_{12} + w'\tau'_{13} - q_1' \end{pmatrix}, \mathbf{F_v}' = \begin{pmatrix} 0 \\ \tau'_{21} \\ \tau'_{22} \\ \tau'_{23} \\ u'\tau'_{21} + v'\tau'_{22} + w'\tau'_{23} - q_2' \end{pmatrix},$$

$$\mathbf{G_v}' = \begin{pmatrix} 0 \\ \tau'_{31} \\ \tau'_{32} \\ \tau'_{33} \\ u'\tau'_{31} + v'\tau'_{32} + w'\tau'_{33} - q_3' \end{pmatrix}$$

The components of the perturbation viscous stress tensor τ'_{ij} are

$$\tau'_{ij} = \mu(\frac{\partial u'_i}{\partial x'_j} + \frac{\partial u'_j}{\partial x'_i} - \frac{2}{3}\delta_{ij}\frac{\partial u'_k}{\partial x'_k}) \tag{2.14}$$

and the perturbation heat flux components ${q_i}'$ are written as follows

$${q_i}' = -k\frac{\partial T'}{\partial x_i} \tag{2.15}$$

As soon as the conservative perturbation variable $\mathbf{U}'$ is obtained from the solution of (2.10), the velocity perturbation u', v', w' may be obtained from $\mathbf{U}'$ and the base flow values using (2.11), while the fluctuating pressure p' may be deduced from

$$e' = \frac{p'}{\gamma - 1} + (\rho_b + \rho')(u'u_b + v'v_b + w'w_b) + \frac{1}{2}(\rho_b + \rho')({u'}^2 + {v'}^2 + {w'}^2) + \frac{1}{2}\rho'({u_b}^2 + {v_b}^2 + {w_b}^2) \tag{2.16}$$

2.3 Numerical methods for computational aeroacoustics

Two main difficulties should be considered when solving a computational aeroacoustics (CAA) code : propose an efficient algorithm for the acoustic wave progagation and to use accurate boundary conditions for the truncated computional domain truncated. Traditional computational fluid dynamics (CFD) schemes are designed for their robustness, but are not really adapted for acoustic problems. In fact, acoustic waves have some typical features that should be taken into account: their nondissipative and nondispersive character; the extremely low amplitude of acoustic perturbations; and the need to be solved of their high frequencies. Therefore, high-order centered finite difference schemes are generally retained in CAA which are by construction non dissipative. The use of such derivatives allows to obtain a very weak discretization error. These schemes are optimized in the Fourier space: we minimize the error over a large range of wavenumbers, and optimize the resolvability (i.e. meshgrid). The goal is thus to control the resolvability limit, and to know the cut-off between resolved and non-resolved scales.

2.3.1 Time advancement

We consider the time integration of the set of equations

$$\frac{\partial \mathbf{U}'}{\partial t} = \mathcal{F}(\mathbf{U}')$$

The conservative pertubation variables $\mathbf{U}'$ are advanced in time using a high-order optimized p substeps Runge-Kutta algorithm.

$$(\mathbf{U}')^{n+1} = (\mathbf{U}')^n + \delta t \sum_{i=1}^{p} b_i K^i \quad \text{with} \quad K^i = \mathcal{F}\left((\mathbf{U}')^n + \sum_{j=1}^{i-1} a_{ij} K^j, t^n + c_j \delta t \right)$$

where $c_i = \sum_{j=1}^{i-1} a_{ij}$ for $i = 1, ...p$. Here, the $p = 6$ substep low-storage Runge-Kutta algorithm with coefficients optimized in the frequency space by Bogey & Bailly [18] is used since it provides a very good trade-off accuracy-stability and cost.

As for all explicit methods, the time step δt has to be chosen to satisfy the conditions of stability of the numerical scheme related to the convective and the conduction-diffusion terms. Within one time step δt, no information is transported further than one computional cell. For convective transport,

$$\text{CFL} = \delta t \times \max_i \left[\frac{|u_i| + c_\infty}{\Delta x_i} \right] \leq 1.73,$$

and for viscous transport:

$$C_{\text{viscous}} = \delta t \times \max_{i,j} \left[\frac{\nu}{\Delta x_i \Delta x_j} \right] \leq \frac{1}{2},$$

where CFL is the Courant-Friedrichs-Lewy (CFL) number. It is clear that the time step has to be chosen according to the more restrictive of the two criteria. For subsonic flows at moderate Reynolds numbers, the CFL criterion associated with the convective transport is always the most restrictive.

2.3.2 Spatial derivatives

In order to calculate accurately the extremely small amplitudes of the acoustic waves relative to the aerodynamic fields, a great care should be given to the choice of the spatial discretization of the flux of the equation. The convective flux are responsible for the aerodynamically generated noise through the nonlinear velocity terms. They describe also the acoustic wave propagation, in particular all interactions between the velocity field and the acoustic fluctuations. They should be discretized with a very accurate numerical scheme. Here, we use the eleven-point-stencil DRP (*Dispersion Relation Preserving*) scheme, introduced by Tam & Webb [114]

$$\left(\frac{\partial \mathbf{E_e}}{\partial x} \right)_{i,j} = \frac{1}{\Delta x} \sum_{l=-5}^{5} a_l \mathbf{E_e}_{i+l,j,k}$$

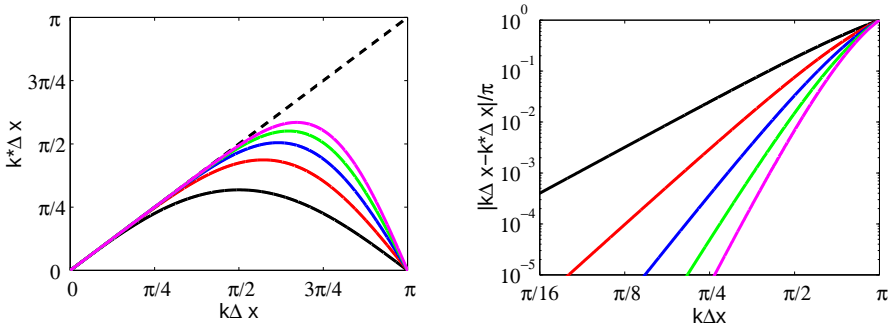

Figure 2.2: Properties of the discretization schemes in the wavenumber space. The exact relationship is displayed in the dotted line. (a) Effective wavenumber of the standard schemes of order 2 (——), 4 (——), 6 (——), 8 (——), 10 (——) as a function of $k\Delta x$. (b) Discretization errors on a logarithmic scale.

The originality of this kind of scheme is that the coefficients a_l have not been determined to to minimize the order of scheme, but to minimize the error between the real wavenumber k and the effective wavenumber $k^\star$ written as

$$k^\star \Delta x = 2 \sum_{j=1}^{5} a_j \sin\left(jk\Delta x\right)$$

In figure 2.2, several effective wavenumbers of standard schemes of different orders are plotted to study the properties of the discretization schemes in the wavenumber space. Note that the dispersion error is given by $\left|k^\star \Delta x - k\Delta x\right| / \pi$.

As noted previously, the coefficients are determined by minimizing the dispersion error, rather than maximizing the formal truncature order of the corresponding Taylor expansion. Bogey & Bailly [18] define the dispersion error as

$$E = \int_{\ln(k\Delta x)_l}^{\ln(k\Delta x)_h} \left|k^\star \Delta x - k\Delta x\right| \, d(\ln(k\Delta x)) \qquad \rightarrow \qquad \frac{\partial E}{\partial a_j} = 0$$

where the two limits $(k\Delta x)_l$ et $(k\Delta x)_h$ have to be chosen. On a stencil of $2N+1$ points, the coefficients a_j for an optimized scheme of order $2M$ $(M < N)$ are calculated by satisfying the M first relationships canceling the terms of the Taylor expansion until Δx^{2M-1}, and by adding $M-N$ relationships $\partial E / \partial a_j = 0$ for $1 \leq j \leq M - N$. For instance, for eleven-point-stencil optimized scheme used in this study, the system $\sum_{j=1}^{N} 2ja_j = 1$; $\sum_{j=1}^{N} j^3 a_j = 0$; $\frac{\partial E}{\partial a_1} = 0$; $\frac{\partial E}{\partial a_2} = 0$; $\frac{\partial E}{\partial a_3} = 0$ is solved with $(k\Delta x)_l = \pi/16$ and $(k\Delta x)_h = \pi/2$. The coefficients are given in Bogey and Bailly [18]. The effect of the optimization procedure is clearly visible in figure 2.3, where the dispersion error of the eleven-point-stencil optimized scheme is significantly reduced in the range between $\pi/4$ and

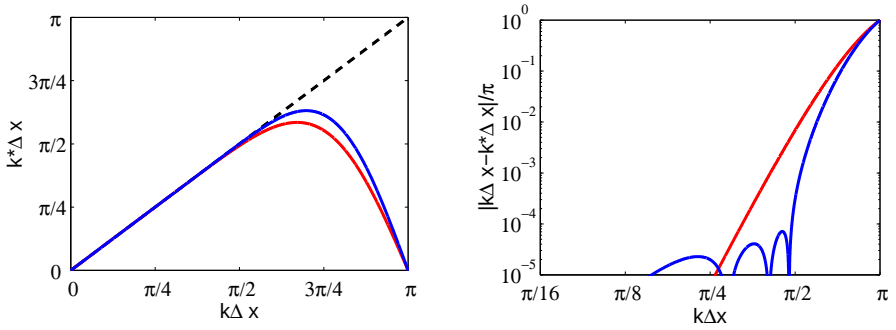

(a) (b)

Figure 2.3: Properties of the discretization schemes in the wavenumber space. The exact relationship is displayed in the dotted line. (a) Effective wavenumber of the tenth-order standard scheme (——), and of the eleven-point-stencil optimized scheme (——) as a function of $k\Delta x$. (b) Discretization errors on a logarithmic scale.

$\pi/2$ when compared with the standard tenth-order scheme. Furthermore, the evaluation of the viscous terms is realized with a fourth-order central finite differences.

2.3.3 Selective filtering

Centered finite difference schemes are non-dissipative and known to give rise to grid-to-grid oscillations (every two points, *i.e.* $k\Delta x = \pi$). These under-resolved spurious short waves are generally created in presence of discontinuities, such as boundary treatment or grid stretching. Unphysical solutions can spread throughout the whole domain, polluting the solutions and leading to numerical instabilities. As a consequence, a centered selective filtering is introduced to eliminate the high-frequency oscillations without affecting the physical solutions.

$$\mathbf{U}'(x_0) = \mathbf{U}'(x_0) - \sigma_d D_f(x_0) \quad \text{and} \quad D_f(x_0) = \sum_{j=-N}^{N} d_j f(x_0 + j\Delta x)$$

with $0 \leq \sigma_d \leq 1$. By applying the Fourier transform, we obtain the damping function

$$D_k(k\Delta x) = d_0 + \sum_{j=1}^{N} 2d_j \cos(jk\Delta x)$$

The damping functions of the standard filters are plotted in figure 2.4.

A centered filter is non-dispersive, so that we minimize the dissipative error, defined as

$$E = \int_{\ln(\pi/16)}^{\ln(\pi/2)} D_k(k\Delta x)\ d(\ln(k\Delta x))$$

In the present study, an optimized centered filter on an 11-point stencil whose coefficients are given in [18] is used. When comparing to the standard 10^{th}

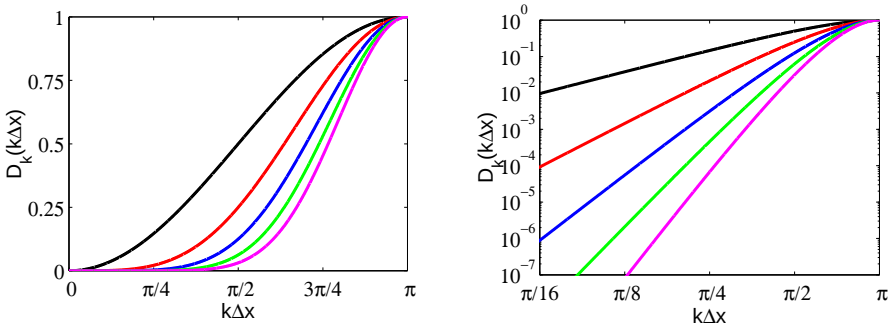

(a) (b)

Figure 2.4: Properties of the selective filters in the wavenumber space. (a) Damping function of the standard centered filters of order 2 (——), 4 (——), 6 (——), 8 (——), 10 (——) as a function of $k\Delta x$. (b) Dissipation errors on a logarithmic scale.

order filter in figure 2.5, it turns out that, for values of $k\Delta x$ close to $\pi/2$, the dissipation error is reduced. The optimization procedure however leads to a greater residual dissipation error for low wavenumbers. In the test case and DNS calculations, only the interior points are filtered with an amplitude of $\sigma_d = 0.2$.

2.3.4 Boundary conditions

Within a theoretical framework, we often assume that the flow domain extends to infinity in all directions. This is not the case for the computational domain which is inevitably finite. Efficient boundary conditions must therefore be imposed along the finite computational domain to mimic a infinite continuous medium. Despite numerous studies, there is no ideal formulation, and the chosen conditions should be compatible with the physical conditions to be imposed, and with the numerical schemes used to discretize them. With dissipative CFD codes, acoustic waves are often strongly attenuated, or even completely dissipated before reaching the boundaries of the computational domain. In a CAA simulation, low-dispersive and low-dissipative schemes are used, so that the waves hit the boundaries, and must exit without generating spurious reflections which can overwhelm the physical waves. It is well-known that Euler equations support small amplitude acoustic, vorticity and entropy waves. Thus, the outgoing disturbances should contain a combination of these three waves. In the present study, a set of radiation and outflow boundary conditions, proposed by Tam & Dong [112], are used. They are applied to five rows of points with decentered DRP scheme, and are advanced in time with the same 6 substeps Runge-Kunta algorithm as for the interior points. We distinguish the outflow conditions at the outflow boundary from the radiation conditions at the inflow, top and bottom boundaries.

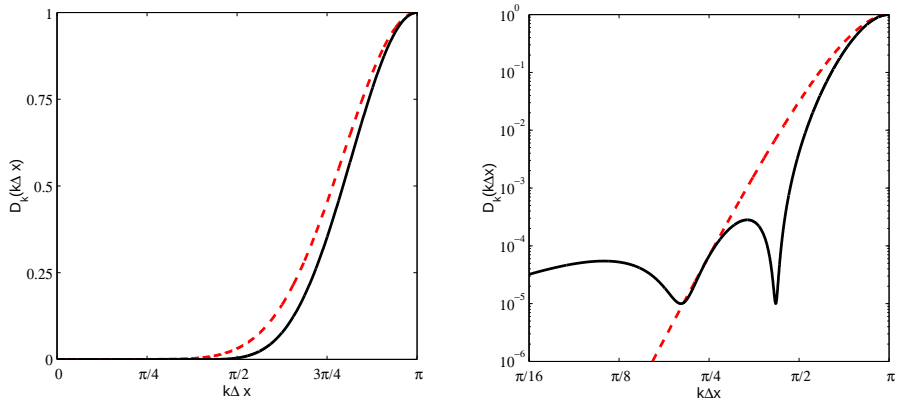

(a) (b)

Figure 2.5: Properties of the selective filters in the wavenumber space. (a) Damping function of the eleven-point stencil optimized filter of Bogey et Bailly [18] (——), and of the tenth-order standard filter (− − −) are compared. (b) Dissipation errors on a logarithmic scale.

Tam and Dong radiation boundary condition

By using the asymptotic solutions of the linearized Euler equations, Tam & Dong have shown that in the far field the outgoing acoustic waves propagate in the radial direction with respect to the noise source in the presence of a mean flow. The boundary conditions which are applied at the inflow and the lateral boundaries are expressed, in 2-D, cylinder coordinate system as

$$\frac{1}{V_g}\frac{\partial}{\partial t}\begin{pmatrix}\rho'\\ u_j\\ p'\end{pmatrix}+\left(\frac{\partial}{\partial r}+\frac{1}{2r}\right)\begin{pmatrix}\rho-\bar{\rho}\\ u_j-\bar{u}_j\\ p-\bar{p}\end{pmatrix}=0 \tag{2.17}$$

where (ρ, u_j, p) are the density, velocity components and pressure, while the mean flow variables are denoted by an overbar. Locally, the acoustic waves propagate out of the computational domain in the direction of θ where (r,θ) is the cylindrical coordinate centered at the noise source. In the presence of the mean flow $\bar{\mathbf{u}} = (\bar{u_j})$, the acoustic waves propagate at a speed and direction equal to the vector sum of the mean flow velocity and the mean sound speed $\bar{c} = \sqrt{\gamma\bar{p}/\bar{\rho}}$. Therefore, in 2-D, the group velocity of wave propagation V_g is given by

$$V_g = \bar{\mathbf{u}}.\mathbf{e_r} + \sqrt{\bar{c}^2 - (\bar{\mathbf{u}}.\mathbf{e}_\theta)^2} \quad \text{with} \quad \begin{cases}\mathbf{e_r} = (\cos\theta, \sin\theta)\\ \mathbf{e}_\theta = (-\sin\theta, \cos\theta)\end{cases}$$

The 3-D formulation is obtained by following similar reasoning as in 2-D, the group velocity becomes

$$V_g = \bar{\mathbf{u}}.\mathbf{e_r} + \sqrt{\bar{c}^2 - (\bar{\mathbf{u}}.\mathbf{e}_\theta)^2 - (\bar{\mathbf{u}}.\mathbf{e}_\varphi)^2} \quad \text{with} \quad \begin{cases} \mathbf{e_r} = (\sin\theta\cos\varphi, \sin\theta\sin\varphi, \cos\theta) \\ \mathbf{e}_\theta = (\cos\theta\cos\varphi, \cos\theta\sin\varphi, -\sin\theta) \\ \mathbf{e}_\varphi = (-\sin\varphi, \cos\varphi, 0) \end{cases} \tag{2.18}$$

and a spherical spreading is assumed for the far-field solution

$$\frac{1}{V_g}\frac{\partial}{\partial t}\begin{pmatrix} \rho' \\ u_j \\ p' \end{pmatrix} + \left(\frac{\partial}{\partial r} + \frac{1}{r}\right)\begin{pmatrix} \rho - \bar{\rho} \\ u_j - \bar{u}_j \\ p - \bar{p} \end{pmatrix} = 0 \tag{2.19}$$

Tam and Dong outflow boundary condition

In addition to the acoustic waves, the vorticity and entropy waves are assumed to be advected downstream by the mean flow as well. The equation governing the fluctuating pressure remains unchanged, but the three other ones are modified in order to allow the exit of the aerodynamic fluctuations convected by the mean flow. The following system is used for the outflow boundary conditions.

$$\begin{cases} \dfrac{\partial \rho'}{\partial t} + \bar{\mathbf{u}}.\nabla(\rho - \bar{\rho}) = \dfrac{1}{\bar{\mathbf{c}}^2}\left(\dfrac{\partial p'}{\partial t} + \bar{\mathbf{u}}\nabla(p - \bar{p})\right) \\ \dfrac{\partial u'}{\partial t} + \bar{\mathbf{u}}.\nabla(u - \bar{u}) = \dfrac{1}{\bar{\rho}}\dfrac{\partial(p - \bar{p})}{\partial x} \\ \dfrac{\partial v'}{\partial t} + \bar{\mathbf{u}}.\nabla(v - \bar{v}) = \dfrac{1}{\bar{\rho}}\dfrac{\partial(p - \bar{p})}{\partial y} \\ \dfrac{1}{V_g}\dfrac{\partial p'}{\partial t} + \dfrac{\partial(p - \bar{p})}{\partial r} + \dfrac{(p - \bar{p})}{2r} = 0 \end{cases} .$$

The 3-D counterpart is given by

$$\begin{cases} \dfrac{\partial \rho'}{\partial t} + \bar{\mathbf{u}}.\nabla(\rho - \bar{\rho}) = \dfrac{1}{\bar{\mathbf{c}}^2}\left(\dfrac{\partial p'}{\partial t} + \bar{\mathbf{u}}\nabla(p - \bar{p})\right) \\ \dfrac{\partial u'}{\partial t} + \bar{\mathbf{u}}.\nabla(u - \bar{u}) = \dfrac{1}{\bar{\rho}}\dfrac{\partial(p - \bar{p})}{\partial x} \\ \dfrac{\partial v'}{\partial t} + \bar{\mathbf{u}}.\nabla(v - \bar{v}) = \dfrac{1}{\bar{\rho}}\dfrac{\partial(p - \bar{p})}{\partial y} \\ \dfrac{\partial w'}{\partial t} + \bar{\mathbf{u}}.\nabla(w - \bar{w}) = \dfrac{1}{\bar{\rho}}\dfrac{\partial(p - \bar{p})}{\partial z} \\ \dfrac{1}{V_g}\dfrac{\partial p'}{\partial t} + \dfrac{\partial(p - \bar{p})}{\partial r} + \dfrac{(p - \bar{p})}{2r} = 0 \end{cases} .$$

2.3.5 Test case of boundary conditions

The numerical techniques described in the previous sections are now applied to an acoustic pulse in a moving medium. In this validation study, the radi-

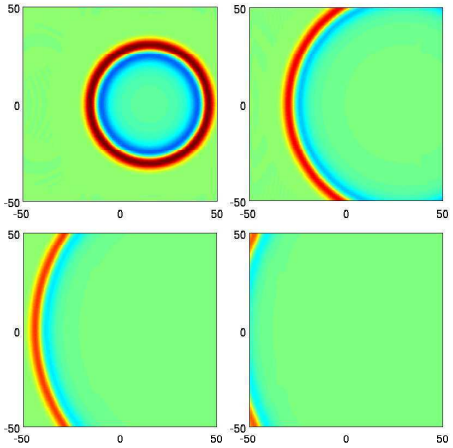

Figure 2.6: Acoustic pressure for the moving pulse in a mean flow Mach number of $M = 0.5$ at four successive instants. Levels from -10 to 10 Pa.

ation and outflow boundary conditions are tested. The computational grid is a Cartesian grid with uniform spacing in all two directions. The grid size is 101×101 and the computational domain is $(L_x, L_y) = (\pm 50, \pm 50)$. The time step is defined for the CFL number of 1, and is given by $t = \Delta x / c_\infty (1+M)$. The acoustic pulse problem being an initial value problem is solved by prescribing the inital condition in pressure. At the initial time, a Gaussian distribution is thus introduced at the center $(0, 0)$ of the computational domain, given by

$$p' = 100 \exp\left[-\frac{\ln 2}{9}(x^2 + y^2)\right]$$

where $u_0 = M c_\infty$ is the mean flow velocity of the moving medium. Figure 2.6 shows the four instants during the calculation. We may observe that most of the acoustic waves has exited the computational domain at the last instant. This indicates that there is no visible numerical reflection from the boundaries. Therefore, the Tam and Dong radiation and outflow conditions have been well validated for the NDE solver.

2.3.6 Sponge zone

The Tam and Dong outflow condition is used at the outflow boundary to allow the exit of vortical structures; nevertheless, some perturbations can still be reflected. It is thus necessary to design a sponge zone to damp out the disturbances before they interact with the boundaries. An obvious way to accomplish this is to apply a Laplacian filter in each direction. Inside the sponge zone, the damping coefficient increases smoothly in space. The perturbations $\mathbf{U}'$ are filtered every time step in the outflow region according

$$\mathbf{U}'_{i,j,k} = \mathbf{U}'_{i,j,k} - \gamma_{max}\left(\frac{x_i - x_{nx-nsx1}}{x_{nx-nsx2} - x_{nx-nsx1}}\right)^{1.5}\left[0.5\mathbf{U}'_{i,j,k}\right.$$
$$\left.-0.25\left(\mathbf{U}'_{i-1,j,k} + \mathbf{U}'_{i+1,j,k} + \mathbf{U}'_{i,j-1,k} + \mathbf{U}'_{i,j+1,k} + \mathbf{U}'_{i,j,k-1} + \mathbf{U}'_{i,j,k+1}\right)\right] \tag{2.20}$$

for $nx - nsx1 \leq i \leq nx - nsx2$, and

$$\mathbf{U}'_{i,j,k} = \mathbf{U}'_{i,j,k} - \gamma_{max}\left[0.5\mathbf{U}'_{i,j,k}\right.$$
$$\left.-0.25\left(\mathbf{U}'_{i-1,j,k} + \mathbf{U}'_{i+1,j,k} + \mathbf{U}'_{i,j-1,k} + \mathbf{U}'_{i,j+1,k} + \mathbf{U}'_{i,j,k-1} + \mathbf{U}'_{i,j,k+1}\right)\right]$$

for $nx - nsx2 < i \leq nx - 1$.

nx denotes the indice of the last grid point in the x-direction. And $x_{nx-nsx1}$ and $x_{nx-nsx2}$ correspond to the abscissae of the beginning and the end of the zone. One may remark that the upstream boundary of the sponge zone itself tends to be reflective, which makes the choice of the damping coefficient subtle. In most cases, γ_{max} is chosen between 0.02 and 0.5 in such way that the damping increases gradually from zero on a relatively long distance to obtain a satisfactorily result. In addition to the artificial damping, a grid stretching (around 3% to 5% for the last grid points) is used to dissipate the vortical structures which are hardly accounted for by the coarser grid, Note that this type of sponge zone has been used successfully by Gloerfelt et Lafon [46] in the simulation of the flow through a diaphragm in a duct.

2.4 Coherent structures: eigenmodes of the propagator

In classical dynamical system theory, the evolution of flow variables $\mathbf{q}'$ may be rewritten into a dynamical system:

$$\mathbf{q}'(\cdot + \Delta\cdot) = \mathcal{B}(\Delta\cdot)\,\mathbf{q}'(\cdot) \tag{2.21}$$

where $\mathcal{B}$ is called the propagator. In particular, we distinguish between temporal analysis and spatial analysis. The first one is associated with $\cdot = t$, where t represents the time evolution. In this context, the mapping between two consecutive times will be realized by the propagator $\mathcal{B}$. The spatial counterpart treats the up- or downstream evolution of perturbations that are generated at a fixed position in space. In this second strategy, $\cdot = x$, where x represents a privileged spatial direction of the flow. For instance, in the near-field analysis, x is the streamwise direction of the mixing layer, whereas in the far-field analysis, x may be the radial direction of the propagating acoustic waves. The action of the propagator according to these two point of views are represented schematically in figures 2.7, 2.8. Therefore, the idea is to associate coherent structures with eigenmodes of the propagator $\mathcal{B}$. In the next sections, we will detail how this theory may be applied to both a linear and a nonlinear framework.

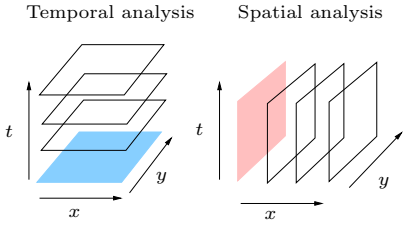

Figure 2.7: Schematic representation of the action of the propagator $\mathcal{B}$ in a spatial and temporal framework (1).

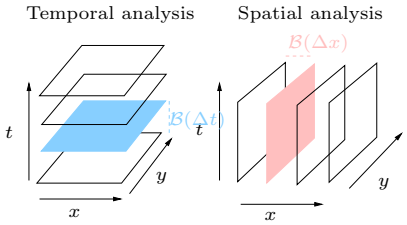

Figure 2.8: Schematic representation of the action of the propagator $\mathcal{B}$ in a spatial and temporal framework (2).

2.5 Linear model: global stability analysis

Global linear stability analysis is interested in the behaviour of the pertubations evolving in a neighborhood of the steady state solution for large times, that is the linear perturbation dynamics after a transient period. These exponentially growing perturbations, the so-called linear global eigenmodes, represent spatially coherent structures that grow or decay exponentially and pulsate with one frequency. If any unstable global eigenmodes exist, pertubations will grow until they saturate nonlinearly. To acquire a complete picture of the flow dynamics, we choose to study the global behavior of the flow within a more general global framework without assumption of parallelism of base flow in this first section.

2.5.1 Governing equations

Recall that throughout this thesis the equations governing the nonlinear space-time dynamics of the flow are the compressible Navier-Stokes equations. They can be written in the following form

$$\frac{\partial \mathbf{q}}{\partial t} = \mathcal{F}(\mathbf{q}) \tag{2.22}$$

where $\mathbf{q} = (\rho, u, v, w, p)^T$ denotes the primitive flow variables and $\mathcal{F}$ the Navier-Stokes operator. A two-dimensional steady solution of (2.22), the so-called base flow is hereafter defined by $\mathbf{q}_b$ such that $\mathcal{F}(\mathbf{q}_b) = 0$. The dynamics of a small perturbation $\mathbf{q}'$ superimposed on this steady base flow $\mathbf{q}_b$ is governed by the linearized Navier-Stokes equations

$$\begin{cases} \dfrac{\partial \mathbf{q}'}{\partial t}\left(\mathbf{x},t\right) = \mathcal{A}\left(\mathbf{q}'\left(\mathbf{x},t\right)\right) \\ \\ \mathbf{q}'\left(\mathbf{x},t=0\right) = \mathbf{q}'_0 \end{cases} \tag{2.23}$$

where $\mathbf{x} = (x,y,z)^T$, and $\mathcal{A}$ is the Jacobian operator of the Navier-Stokes equations $\mathcal{F}$ linearized about the base flow $\mathbf{q}_b(x,y)$ which is given by: $\mathcal{A} = \partial\mathcal{F}/\partial\mathbf{q}|\mathbf{q}_b$. Therefore, the asymptotic stability of the system (2.23) is determined by resolving the spectrum of the governing linear operator $\mathcal{A}$ (Schmid [99]). Solutions of (2.23) may be thought in the form of normal modes

$$\mathbf{q}'\left(\mathbf{x},t\right) = \hat{\mathbf{q}}\left(\mathbf{x}\right)e^{-i\omega t} \tag{2.24}$$

The associated dynamical structures are referred to as global modes $(\omega, \hat{\mathbf{q}})$ of the base flow $\mathbf{q}_b$. Their spatial structure is characterized by the complex vector field $\hat{\mathbf{q}}$ and their temporal behaviour by the complex $\omega = \omega_r + i\omega_i$. In this way, the initial value problem (2.23) will be transformed into an eigenvalue problem of the form

$$\mathcal{A}\hat{\mathbf{q}} = -i\omega\hat{\mathbf{q}} \tag{2.25}$$

The eigenvalues and eigenvectors of $\mathcal{A}$ correspond to the global modes. In particular, if $\omega_i < 0$, the base flow is asymptotically stable, the global modes will decay for large times. Otherwise, if $\omega_i > 0$, then the solution $\mathcal{F}\left(\mathbf{q}_b\left(x,y\right)\right) = 0$ is asymptotically unstable, whose unsteadiness is characterized by the angular frequency ω_r.

2.5.2 Matrix-free method: timestepper approach and propagator

Global modes are computed by using the matrix-free method which are based on flow field snapshots. That is, very large eigenvalue problems are solved based only on snapshots of the flow field at different points in time whihout any large matrices stored. Within the temporal framework, the snapshots are obtained by abstract notion of a time stepper $\mathcal{B}(\Delta t)$. In this timestepper approach (Tuckerman & Barkley [116]), starting with an initial perturbation $\mathbf{q}_0$, $\mathcal{B}(\Delta t)$ is the evolution operator representing the action of the operator (2.23) from one flow field to the next over a equidistant time interval Δt.

$$\mathbf{q}'\left(t=\Delta t\right) = \mathcal{B}\left(\Delta t\right)\mathbf{q}'_0, \text{ where } \mathcal{B}\left(\Delta t\right) \text{ is formally } e^{\mathcal{A}\Delta t} \tag{2.26}$$

The temporal evolution of our input data sequence from the flow field can be represented schematically in figures 2.7, 2.8. The flow dynamics is thus associated with this propagator. In most cases, our analysis is based on the flow fields sampled at discrete time, it is then convenient to adopt the discrete-time setting. This allows us to write (2.26) in a discrete dynamical system

$$\mathbf{q}'_{k+1} = \mathcal{B}\left(\Delta t\right)\mathbf{q}'_k \tag{2.27}$$

where $\mathbf{q}'_k$ is the kth perturbation field.

In the previous section, the linear global eigenmodes have been defined as the eigenvectors and eigenvalues of the discretized and linearized Navier–Stokes

equations $\mathcal{A}$. The dimension of the matrix $\mathcal{A}$ in (2.23) is so large that we cannot compute the eigenvalues of $\mathcal{A}$ using direct methods, such as QR method. Furthermore, since we are often interested in a small portion of the spectrum which represents main instability mechanisms only, solving such an enormous eigenvalue problem becomes also pointless. For instance, Bagheri [5] showed several examples of state-space dimension n for some flow cases, all of the computations scale at least $O(n^3)$. Therefore, iterative methods, such as the Arnoldi, are often adopted to find approximates of the eigenvalues of $\mathcal{A}$, in which the original large-scale problem (2.23) is projected onto a dynamical system of significantly fewer degrees of freedom. The resulting low-dimensional system can then be solved by direct methods. The idea is to associate the coherent structures with the eigenmodes of the propagator $\mathcal{B}$. A subspace spanned by snapshots sampled from flow fields may then be represented in the form of a snapshot sequence, given by a matrix S_N

$$S_N = \{\mathbf{q}'_0, \mathcal{B}(\Delta t)\,\mathbf{q}'_0, [\mathcal{B}(\Delta t)]^2\mathbf{q}'_0, ..., [\mathcal{B}(\Delta t)]^{N-1}\mathbf{q}'_0\} = \{s_0, s_1, \cdots, s_{N-1}\} \tag{2.28}$$

where $\mathbf{s}_0$ and $\mathbf{s}_{N-1}$ denote the first and the last entry of the sequence, respectively. This time-stepper technique has become increasingly popular in both stability analysis (Barkley, Gomes & Henderson[11], Barkley, Blackburn & Sherwin [10], Blackburn, Barkley & Sherwin [16], Bagheri *et al.* [7] and Alizard & Robinet [2]) and control design (Bagheri, Brandt & Henningson [6]). The time step Δt between two consecutive snapshots should be chosen properly and will be further discussed in the next chapter.

2.5.3 Arnoldi algorithm

The well-known Arnoldi algorithm is a type of iterative method that successively orthogonalizes the vectors of the sequence (2.28), and therefore yields an orthonormal sequence : ${S_N}^{\perp} = \{\ s_0^{\perp}, \cdots,\ s_{N-1}^{\perp}\}$. The orthonormalization has been achieved by a Gram-Schmid method resulting in a decomposition of the form

$$\mathcal{B}(\Delta t)\,{S_N}^{\perp} = \ {S_N}^{\perp}\mathcal{H} + \mathbf{r}\mathbf{e}^T S_N^{\perp} \tag{2.29}$$

with $\mathbf{r}$ a residual, $\mathbf{e}^T = (0, \cdots, 1)$ a unit vector of dimension N, $S_N^{\perp}$ a normalized vector of dimension N such as $S_N^{\perp} \perp \mathcal{S}_{N-1}^{\perp}$ and $\mathcal{H}$ an upper Hessenberg matrix of dimension $N \times N$.

And hence the dominant eigenmodes of $\mathcal{B}(\Delta t)$ are approximated by computing the eigenmodes of the reduced matrix $\mathcal{H}$: the so-called Ritz values and Ritz vectors of $\mathcal{B}(\Delta t)$ which are denoted by d_k and ϑ_k with $k \in (0, .., N-1)$. A residual value for each eigenmode of $\mathcal{B}(\Delta t)$ is evaluated according to

$$\mathbf{r}|(\vartheta_k)_m|,\ k \in (0, .., N-1) \tag{2.30}$$

The dominant eigenvalues of $\mathcal{A}$ are derived from the latter

$$\begin{cases} (\omega_i)_k = Re\left(\log(d_k)/\Delta t\right) \\ (\omega_r)_k = Im\left(\log(d_k)/\Delta t\right) \end{cases} \tag{2.31}$$

where $(\omega_i)_k$ and $(\omega_r)_k$ are the temporal amplification rate and the angular frequency of the mode k respectively. The sampling period Δt has to be sufficiently small to verify the Nyquist criterion. The underlying eigenvectors of $\mathcal{A}$ are recovered through a simple matrix product

$$\mathbf{q}'_k = {S_N}^{\perp} \vartheta_k \tag{2.32}$$

This yields a more stable algorithm resulting a rapid convergence with a satisfactory accuracy in the orthonormal basis.

2.5.4 Numerical implementation

The major task of the algorithm described above is to compute the upper Hessenberg matrix. Instead of the standard software ARPACK package commonly used, we use a more generic self-made algorithm. For instance, our algorithm allows to start with a chosen initial perturbation rather than some random noise. Moreover, the choice of inner product in the projection step may also be influential in compressible flows. We will demonstrate the eventual influence of the inner products in the next part. Thus, the sequence of snapshots S_N is orthonormalized with respect to the chosen inner product denoted by $(,)$, through a Gram-Schmidt algorithm. This process is repeated until the following criterion is satisfied.

$$\max_{i,j}(\ s_i^{\perp},\ s_j^{\perp}) < 10^{-16}\ \text{, for } i \neq j \text{ with } (i,j) \in (0,..,N-1)^2 \tag{2.33}$$

By considering the system (2.29), the Hessenberg matrix of components $H_{i,j}$ is easily recovered by

$$H_{i,j} = (\mathcal{B}(\Delta t)\ s_i^{\perp},\ s_j^{\perp}) \tag{2.34}$$

where $s_i^{\perp}$ represents the sample of the sequence ${S_N}^{\perp}$. For $(i = 0,..,N-1)$, $\mathcal{B}(\Delta t)\ s_i^{\perp}$ are derived successively from the following Gram-Schmidt step

$$\begin{aligned}
\mathcal{B}(\Delta t)\ s_i^{\perp} &= \mathcal{B}(\Delta t)\left(s_i - \sum_{k=1}^{i-1} \frac{(\ s_k^{\perp}, s_i)}{(\ s_k^{\perp},\ s_k^{\perp})}\right)\ s_k^{\perp} \\
&= \mathcal{B}(\Delta t)(s_i) - \sum_{k=1}^{i-1} \frac{(\ s_k^{\perp}, s_i)}{(\ s_k^{\perp},\ s_k^{\perp})} \mathcal{B}(\Delta t)\left(\ s_k^{\perp}\right) \\
&= (s_{i+1}) - \sum_{k=1}^{i-1} (\ s_k^{\perp}, s_i) \mathcal{B}(\Delta t)\left(\ s_k^{\perp}\right)
\end{aligned} \tag{2.35}$$

with $S_N = \mathcal{B}(\Delta t)(S_{N-1})$ and $(\ s_k^{\perp},\ s_k^{\perp}) = 1$ from the normalization. The dimension of the Krylov sequence S_N is increasing until to reach a residual (2.30) fixed to the machine precision for the considered eigenmodes. The eigenvalues of $\mathcal{H}$ are computed using a QR algorithm from LAPACK library.

2.6 Nonlinear model: Dynamic mode decomposition analysis

When small flow disturbances grow exponentially until they reach a stage where nonlinear effects become important and have to be taken into account, it is necessary to undertake a modal analysis of the fully nonlinear flow. To study the behaviour of complex nonlinear flow, a technique is used by decomposing the flow into a set of Koopman modes (Rowley & al. [97]), determined from the spectral analysis of the Koopman operator.

2.6.1 Koopman operator and Koopman modes

Consider a nonlinear evolving dynamical system as follows:

$$\mathbf{q}'_{k+1} = \mathbf{f}(\mathbf{q}'_k)$$

where $\mathbf{f}$ denotes a nonlineaire operator representing the underlying flow dynamics. A linearization in the phase space yields to the dynmical system

$$\mathbf{q}'_{k+1} = \mathcal{B}\left(\Delta t/\Delta x\right)(\mathbf{q}'_k)$$

$\mathcal{B}\left(\Delta t/\Delta x\right)$ is therefore a linear operator as defined in the previous section (2.21). Here, $\mathbf{q}'$ is the vector-valued observable which may be any quantities of interest, such as a velocity, pressure or density fields at various grid points in the flow from either a physical experiment or a numerical simulation. In our work, we have assumed that the propagator $\mathcal{B}\left(\Delta t/\Delta x\right)$ remains unchanged in the phase space. As in Mezić [73], the vector-valued observable $\mathbf{q}'$ may be expanded in terms of the eigenfunctions ψ_j as

$$\mathbf{q}' = \sum_{j=1}^{N} \psi_j \mathbf{v}_j \tag{2.36}$$

where the eigenfunctions ψ_j are referred to as Koopman eigenfunctions, and the associated vectors $\mathbf{v}_j$ are the Koopman modes. The observable can be expressed in term of the first entry $\mathbf{q}'_0$ in the input snapshot sequence by iterating $\mathbf{q}'_0$, then the kth sample is given by

$$\mathbf{q}'_k = \sum_{j=1}^{N} \lambda_j^k \psi_j(\mathbf{q}'_0)\mathbf{v}_j \tag{2.37}$$

Henceforth, the constant $\psi_j(\mathbf{q}'_0)$ will be encompassed into $\mathbf{v}_j$ for simplicity. The Koopman eigenvalues, λ_j, therefore characterize the temporal behaviour of the corresponding Koopman mode $\mathbf{v}_j$: the phase of λ_j determines its frequency, and the magnitude determines the growth rate. As demonstrated in Rowley & al. [97], for linear systems, these modes coincide with the global eigenmodes, and for the special case of periodic systems, the modes can be determined by the discrete temporal Fourier transform. In this nonlinear framework, the coherent structures are associated with the propagator $\mathcal{B}$ defined as the Koopman operator.

2.6.2 Dynamic Mode Decomposition

The Dynamic Mode Decomposition (DMD) algorithm which is described in Rowley et 2009; Schmid 2010, will be summarized here. In contrast to the Arnoldi algorithm, Rowley & al. [97] and Schmid [100] have proposed an algorithm in which no normalization procedure is required. Consider the discrete dynamical system (2.27) and the spanned Krylov subspace (2.28). Assuming that the vector s_N of the Krylov sequence become linearly dependent for certain N. Therefore, the vector s_N can be considered as a linear combination of the previous vectors, that is

$$s_N = c_0 s_0 + c_1 s_1 + \cdots + c_{N-1} s_{N-1} + \mathbf{r} \tag{2.38}$$

where $\mathbf{c}^T = (c_0, c_1, \cdots, c_{N-1})$ and $\mathbf{r}$ is a residual given by

$$\mathbf{r} = s_N - S_N \mathcal{C} \tag{2.39}$$

which is minimized when c_i is chosen such that $\mathbf{r} \perp \{s_0, s_1, \cdots, s_{N-1}\}$. (2.38) is rewritten in matrix form

$$\mathcal{B} S_N = S_N \mathcal{C} + \mathbf{r}\mathbf{e}^T \tag{2.40}$$

Recall that $\mathcal{B}$ denotes the propagator from one data field to the next over a time interval (spatial) Δt (Δx). Here, $\mathbf{e}^T = (0, \cdots, 1)^T$ is the unit vector, and $\mathcal{C}$ is a companion matrix with

$$\mathcal{C} = \begin{bmatrix} 0 & 0 & \cdots & 0 & c_0 \\ 1 & 0 & \cdots & 0 & c_1 \\ 0 & 1 & \cdots & 0 & c_2 \\ \vdots & & \ddots & & \vdots \\ 0 & 0 & \cdots & 1 & c_{N-1} \end{bmatrix} \tag{2.41}$$

The spatial structures in the flow can be thus decomposed into Koopman modes. The corresponding Koopman eigenvalues describe the temporal behaviour of the Koopman modes. In other words, the phase of λ_j gives its frequency, and the magnitude provides the growth rate. Regarding ψ_j, the Koopman eigenfunction determines the amplitude of the associated Koopman mode. It is straightforward to show that, if the dynamics (2.27) is linear, then the eigenvalues of $\mathcal{B}$ are also eigenvalues of the Koopman operator, and the eigenvectors of $\mathcal{B}$ coincide with the Koopman modes. The eigenvalues and corresponding eigenvectors of $\mathcal{C}$ are then approximations to the eigenvalues and eigenvectors of $\mathcal{A}$, which we call Ritz values and Ritz vectors, respectively.

2.7 Orthogonal projection

A solution of (2.23) may be decomposed into a basis formed by following global modes/Koopman modes:

$$\mathbf{q}'(\mathbf{x}) = \sum_{k=0}^{m-1} K_k e^{-i\omega_k t} \hat{\mathbf{q}}_k(\mathbf{x}) \tag{2.42}$$

where $e^{-i\omega_k t}\hat{\mathbf{q}}_k(\mathbf{x})$ are the global modes/Koopman modes and K_k are the scalar expansion coefficients. Since the global mode and Koopman mode bases are non-orthogonal, we need to perform a projection procedure in order to orthonormalize the basis of interest. For non-normal flow problems, a bi-orthogonal projection of the system (2.23) onto a set of global modes is conventionally used (see Barbagallo, Sipp & Schmid [9], Ehrenstein,Passaggia & Gallaire [38]). In this context, the bi-orthogonal condition is employed to determine the components of the initial condition of disturbance into the global modes expansion by:

$$K_k = \frac{< \hat{\mathbf{q}'_k}^*, \mathbf{q}'_0 >}{< \hat{\mathbf{q}'_k}^*, \mathbf{q}'_k >}$$

with $<,>$ a standard Hermitian scalar product. Nevertheless, when performing a projection through a Hermitian inner product by using adjoint modes, a numerical difficulty arises from the non-normality of the evolution operator, thus resulting in the separation between adjoint and direct modes (Chomaz [28]). Indeed, the projection into a global modes basis is governed by the values of $< \mathbf{q}'^*_i, \mathbf{q}'_i >$. The strong non-orthogonality leads to the separation of the spatial support of $\mathbf{q}'_i$ and $\mathbf{q}'^*_i$. As observed for example by Alizard & Robinet [2], the value of $< \mathbf{q}'^*_i, \mathbf{q}'_i >$ decays gradually when increasing the non-orthogonality until to reach a value close to zero 10^{-11}. As a consequence, it becomes almost impossible to numerically verify the biorthogonality condition. To overcome this, Passaggia, Ehrenstein & Gallaire [89], Alizard & Robinet [2] and Ehrenstein, Passaggia & Gallaire [38] proposed an orthogonal projection. Since the basis of global modes is non-orthogonal, a modified Gram-Schmidt procedure is undertaken to orthogonalize the basis. Let us denote the orthogonal basis: $(\mathbf{q}'^{\perp}_0, \mathbf{q}'^{\perp}_1, \cdots, \mathbf{q}'^{\perp}_{m-1})$ from the global modes expansion of dimension m through the orthogonalization. The initial perturbation may be expanded as

$$\mathbf{q}'_0(\mathbf{x}) = \sum_{k=0}^{m-1} \Lambda_k \mathbf{q}'^{\perp}_k(\mathbf{x}) \tag{2.43}$$

Taking the orthogonality of the basis into consideration

$$\Lambda_p = (\mathbf{q}'^{\perp}_p, \mathbf{q}'_0) \tag{2.44}$$

where $(,)$ is an energy-based inner product, defined in (3.3). Therefore, the coordinates in the basis of global modes are recovered by making use of a matrix product

$$\mathbf{K} = \mathcal{P}^{-1}\xi \tag{2.45}$$

with $\mathbf{K} = (\hat{K}_0, \hat{K}_1, \cdots, \hat{K}_{m-1})^T$, and $\mathbf{\Lambda} = (\Lambda_0, \Lambda_1, \cdots, \Lambda_{m-1})^T$. The coefficients of $\mathcal{P}$ are given by: $\mathcal{P}_{i,j} = (\mathbf{q}'^{\perp}_j, \mathbf{q}'_i)$. This orthogonal projection is seen to provide a better accuracy of the perturbation field than using the bi-orthogonal property (See [2], [89], [38]).

2.8 Integral methods for Acoustic analogy

In contrast to direct methods which are often very expensive, integral methods based merely on near-field input provide an alternative to predict the acous-

tic radiated sound, which consist in two steps: an aerodynamic code based on CFD/CAA algorithms is employed to evaluate the flow field, and then an integral formulation is applied to propagate the pressure fluctuations to the acoustic far-field. There exist two major approaches: one is acoustic analogy, which divides the domain into an aerodynamic region where the source terms responsable for sound generation, and an acoustic region governed by a linear wave equation; and the other one is the wave extrapolation method, which evaluates the acoustic far field from the knowledge of the near-field compressible on a control surface. The latter are not limited to the aeroacoustics but are also valid for any phenomena dominated by a linear wave equation, such as optics, acoustics or electromagnetism.

2.8.1 Convected formulation of FW-H equations

To include the effects of solid surfaces in arbitrary motion, the acoustic analogy originally proposed by Lighthill [65] was extended by Curle [35] and Ffowcs Williams and Hawkings [119]. The FW-H equation is a rearrangement of exact continuity and Navier-Stokes equations. A time-domain solution to the FW-H equation can be obtained from the wave equation convolution with the free-space Green function. The solution giving rise to an infinite time integral in two dimensions remains the main difficulty. Indeed, the use of Heaviside function can change the upper limit to a finite value, but the lower limit will always be infinite. In addition, the time integration range needed to capture all of the two-dimensional effects may be quite large (Lockard [71]). Therefore, to avoid the expensive time integration and the evaluation of retarded time which may be delicate to deal with, the FW-H equation is formulated into the frequency domain in two dimensions (Lockard [71], Guo [48]). Besides, in presence of an uniform flow, Ffowcs Williams and Hawkings proposed using a Lagrangian co-ordinate transform assuming that the surface is moving in a fluid at rest. By using the derivatives for an observer moving along with the mean flow in the rewritting of the continuity and momentum equations (Goldstein [47]), an inhomogeneous, uniformly moving medium wave equation is obtained. This convected wave equation contains the convection effects in the wave operator. Details of this spectral formulation in detail are provided in Gloerfelt [44].

In the case of mixing layer, no boundary is involved, the integral solution of the convected FW-H equation is

$$p'(\mathbf{x},\omega) = -\iint_{f>0} T_{ij}(\mathbf{y},\omega)\frac{\partial^2 G(\mathbf{x}|\mathbf{y},\omega)}{\partial y_i \partial y_j}\, d\mathbf{y} \tag{2.46}$$

The observer position and a source point are denoted by $\mathbf{x}$ and $\mathbf{y}$. The angular frequency is ω. Given that the sound sources are aerodynamic, we neglect the entropic and viscous sources. The source terms are given by the following expression

$$T_{ij} \approx \rho(u_i - U_i^\infty)(u_j - U_j^\infty) \tag{2.47}$$

where U_i^∞ are the components of the uniform mean velocity in the observer domain. The Green function is written as

$$G(\mathbf{x}|\mathbf{y},\omega) = F(r_1)H_0^{(2)}\left(\frac{kr_\beta}{\beta^2}\right) \tag{2.48}$$

where $k = \omega/c_\infty$ denotes the wavenumber, and

$$F(r_1) = \frac{i}{4\beta} \exp\left(\frac{i\mathrm{M}kr_1}{\beta^2}\right)$$

The spatial derivatives of the Green functions can be calculated analytically yielding

$$\begin{cases} \dfrac{\partial^2 G(\mathbf{x}|\mathbf{y},\omega)}{\partial y_1 \partial y_2} = -F(r_1)\left\{\dfrac{k^2}{\beta^2}\dfrac{r_1 r_2}{r_\beta^2} H_0^{(2)}\left(\dfrac{kr_\beta}{\beta^2}\right) + \dfrac{kr_2}{r_\beta}\left(\dfrac{i\mathrm{M}k}{\beta^2} - \dfrac{2r_1}{r_\beta^2}\right) H_1^{(2)}\left(\dfrac{kr_\beta}{\beta^2}\right)\right\} \\ \dfrac{\partial^2 G(\mathbf{x}|\mathbf{y},\omega)}{\partial y_1^2} = -F(r_1)\dfrac{k^2}{\beta^4}\left\{\left(\mathrm{M}^2 + \dfrac{r_1}{r_\beta^2}\right) H_0^{(2)}\left(\dfrac{kr_\beta}{\beta^2}\right) + \left(\dfrac{2i\mathrm{M}r_1}{r_\beta} - \dfrac{\beta^2}{k}\dfrac{r_1^2 - \beta^2 r_2^2}{r_\beta^3}\right) H_1^{(2)}\left(\dfrac{kr_\beta}{\beta^2}\right)\right\} \\ \dfrac{\partial^2 G(\mathbf{x}|\mathbf{y},\omega)}{\partial y_2^2} = -F(r_1)\left\{\dfrac{k^2 r_2^2}{r_\beta^2} H_0^{(2)}\left(\dfrac{kr_\beta}{\beta^2}\right) + \dfrac{k}{r_\beta}\left(\dfrac{r_1^2 - \beta^2 r_2^2}{r_\beta^2}\right) H_1^{(2)}\left(\dfrac{kr_\beta}{\beta^2}\right)\right\} \end{cases} \tag{2.49}$$

where $r_i = x_i - y_i$, $\mathrm{M} = U_i^\infty/c_\infty$, $\beta = \sqrt{1-\mathrm{M}^2}$, $r_\beta = \sqrt{(x_1-y_1)^2 + \beta^2(x_2-y_2)^2}$. $H_0^{(2)}$ and $H_1^{(2)}$ are the Hankel functions of second kind, of first and second order, respectively.

2.8.2 Numerical implementation using data from DNS or ROM

Considering the quasi-periodic behaviour of the oscillations in the mixing layer, the first step is to record the aerodynamic quantities during one period of the DNS or ROM computations. Then, the source term T_{ij} is calculated and transformed into the frequency domain using the following Fourier transform

$$\mathcal{F}\left[\phi(\mathbf{x},t)\right] = \phi(\mathbf{x},\omega) = \int_{-\infty}^{\infty} \phi(\mathbf{x},t) e^{-i\omega t}\, dt \tag{2.50}$$

The integrals are thus evaluated at each point of an acoustic meshgrid. Finally, an inverse Fourier transform is applied to recover the acoustic signal in the time domain. Some special precautions should be taken into consideration when transforming a signal that is not perfectly periodic. First, data must be recorded during long enough time to represent low frequency components. Secondly, the sampling rate must be quite high to account for the high frequencies. Lastly, windowing and data segmenting techniques and can be used to compensate the aperiodic components of the signal. This formulation in frequency domain has been validated in the computation of noise radiation by a subsonic cavity flow in Gloerfelt [42].

Chapter 3

Single vortex pairing: from a linear to a nonlinear model

Through the previous studies of Brown & Roshko [25] and Winant & Browand [121], it has been generally acknowledged that large-scale vortex structures can be initiated by exciting the flow with particular instability waves at the inlet location. Note that the linear stability theory allows to determine the fundamental frequency f_0 of the inlet instability wave, chosen based upon the most unstable frequency of the mixing layer. In general, the excitation with f_0 leads to the downstream development of well-organized periodic coherent structures in the flow, and further subharmonic forcing causes vortex pairing occurring near the apparent acoustic source origin. The mechanism of sound generation is due to the vortex pairing initiated by these two instability modes. This is in correlation with the work of Colonius, Lele & Moin [30] and Bogey, Bailly & Juvé [20].

In this chapter, the sound generated by only one single vortex pairing in the flow is investigated. First, the results from the direct calculations are presented. Then, a series of two computations of the mixing layer by means of a modal decomposition method is performed: in the first series, a purely linear model excluding the nonlinear interactions between modes is considered, a global stability analysis based on the global modes is used to calculate and describe the behaviour of the instability waves emerging in the flow. In addition, the absence of nonlinear interactions results in maintained exponential growth of the fundamental and first subharmonic modes. We then highlight the importance of including the nonlinear interactions to capture the large-scale vortex structures and eventually the radiated sound. Therefore, in the second set of computation, a DMD analysis is performed in a fully nonlinear approach, and the results are provided accordingly.

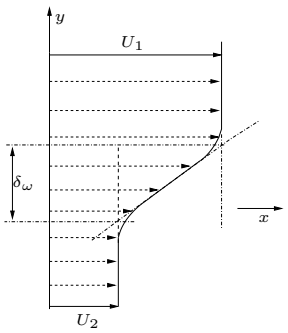

Figure 3.1: The parallel base flow considered hereafter is illustrated.

3.1 Direct computation

First, the relevant numerical parameters for the compressible two-dimensional shear layer are given. The Mach numbers of the high- and low-speed streams are $M_1 = 0.12$ and $M_2 = 0.47$, respectively. The convective Mach number is $M_c = 0.176$. The Reynolds number based on the initial vorticity thickness of the mixing layer $\delta_\omega(0) = 1.6 \times 10^{-3}$m and the velocity difference across the layer ΔU, $Re = \Delta U \delta_\omega(0)/\nu$ is 13692. This parallel tangent hyperbolic profile is chosen as our base flow and is depicted in Figure 3.1.

To take into account several acoustic wavelengths, the grid is extended in normal direction. Thus, a Cartesian grid of 441 by 441 grid points in the $x-$ and $y-$ directions, respectively, is used. The computational domain is $(L_x, L_y) = (290, \pm 300)\delta_\omega(0)$ excluding the sponge zone. The grid in x is uniform with spacing $\Delta x_{min} = 0.32\delta_\omega(0)$ up to $x = 160\delta_\omega(0)$. The grid is then highly stretched in the sponge zone. In the normal direction, the grid is stretched at 1.8% from $\Delta y_{min} = 0.16\delta_\omega(0)$ in the shear region around $y = 0$ to large $y = \pm 300$. To absorb outgoing acoustic waves with minimal reflection, sponge layer defined in (2.20) are employed at the outflow boundary, extending from $x = 160\delta_\omega(0)$ to $x = 340\delta_\omega(0)$. The damping coefficient of the Laplacian filter γ_{max} in (2.20) is chosen as 0.4. The grid resolution is shown in figure 3.2. The CFL number of the simulation is 1 which gives a time-step $\delta t = \Delta y_{min}/c_\infty = 7.56 \times 10^{-7}$ s. Note that test cases of the grid independence have been performed, and the grid resolution is sufficient for the present numerical investigation.

To compute directly the sound generated by vortex pairing in a mixing layer, we force artificially the flow at its fundamental frequency, f_0, and its first subharmonic $f_0/2$, as in the work of Bogey, Bailly & Juvé [20]. The amplitude of f_0 is double that of $f_0/2$ which is the same as their simulation [20]. According to Kelly's analysis [60], the phase difference between the two waves is found to play an important role in the amplification of the subharmonic mode, and consequently, the nature of the vortex-interaction mechanism. More precisely, the larger the initial phase difference β is, the slower the coalescence of the two vortices is. Based on the observation from the temporal simulation of Riley & Metcalfe ([94]), a vortex-pairing interaction occurs for all values of β apart from those close to π. And when β is increased, one structure becomes thinner than

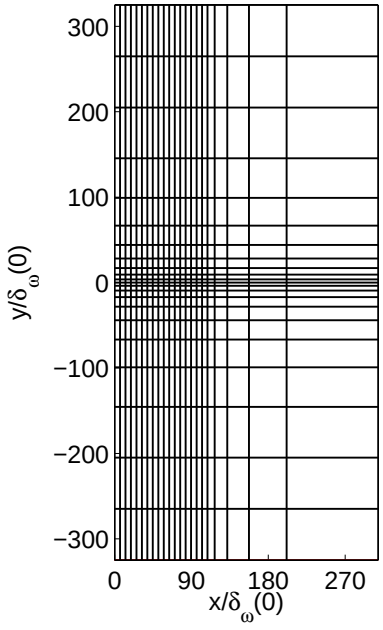

Figure 3.2: Grid resolution for the mixing layer forced at f_0 and $f_0/2$. Every ten points are represented.

the other during the pairing process. Thus, we choose an intermediary value $\beta = \pi/2$. The forcing is applied to the streamwise and cross-stream components of the velocity perturbations, along the plane $i = 6$, at every time-step:

$$\begin{cases} u'(x,y) = \dfrac{(y-y_0)}{\Delta y_0} U_c \left[\alpha_1 \sin(\omega_0 t) + \alpha_2 \sin(\dfrac{\omega_0}{2} t + \beta)\right] Q \\ \\ v'(x,y) = -\dfrac{(x-x_0)}{\Delta y_0} U_c \left[\alpha_1 \sin(\omega_0 t) + \alpha_2 \sin(\dfrac{\omega_0}{2} t + \beta)\right] Q \end{cases} \tag{3.1}$$

where $(x_0, y_0) = (1.5\delta_\omega(0), 0)$ corresponds to the plane $i = 6$. Note that this choice is due to the decentered 11-point stencil near the border of calculation domain. The fundamental frequency f_0 is chosen as determined by Michalke [74] for a hyperbolic-tangent velocity profile: $f_0 = 0.132 U_c/\delta_\omega(0) = 8250$ Hz, and $\omega_0 = 2\pi f_0 = 51836$ rad/s is the associated angular frequency. Hereafter, the angular frequency will be nondimensionalized with the convection velocity and initial vorticity thickness $\delta_\omega(0)$ yielding 0.829 for the fundamental mode. Likewise, the temporal growth rate ω_i and the time t will also be used and represented in non-dimensional form throughout this thesis. The Gaussian function is defined as

$$Q = \exp\left[-\ln 2 \frac{(x-x_0)^2 + (y-y_0)^2}{{\Delta y_0}^2}\right]$$

where its half-width is $\Delta y_0 = 3\Delta y_{min}$. The amplitudes of these two frequencies are $\alpha_1 = 2 \times 10^{-4}$ and $\alpha_2 = 10^{-4}$, respectively. This method of excitation enables us to control the vortex pairings in the mixing layer ([107], [30] and [20]).

An instantaneous vorticity field after the saturated regime in the mixing near-field region is shown in figure 3.3. The spanwise vorticity plot exhibits obviously the roll up and the fixed vortex pairings. The acoustic pattern shown in figure 3.5 (a) illustrates the acoustic field resulting from vortex sound generation mechanism.

The noise production through the nonlinear interaction of instability waves can be as well captured by means of an acoustic analogy method by using the near-field source terms calculated from the DNS. In this thesis, the convected formulation of FW-H analogy is solved as discussed in the chapter 2. Since the lowest frequency to resolve is $f_0/2$, a transform of length at least $2/f_0$ is needed, which corresponds to a pairing period T_{app} during which large vortical structures occur. We run the simulation after the satured regime for a pairing period. The source is recorded and sampled every timestep in the near-field region extending from $x = 0$ to $x = 290\delta_\omega(0)$ and $y = -15\delta_\omega(0)$ to $y = 15\delta_\omega(0)$ in the streamwise and cross-stream directions, respectively. Here, we show the source data in this near-field region by plotting the pressure fluctuations in figure 3.4. A regular Cartesian grid of 101×121 points is used for the acoustic mesh grid. The grid spacings in the $x-$ and $y-$ directions are $\Delta x = \Delta y = 4 \times 10^{-3}$ m. This observation region is characterized by a static pressure $p_\infty = 10^5$ Pa, a density $\rho_\infty = 1.22 kg/m^3$ and a speed of sound $c_\infty = 339$ m/s.

The predicted fluctuating pressure from the acoustic analogy in the above and bottom parts of the far field is shown in figure 3.5 (b). Comparing the results

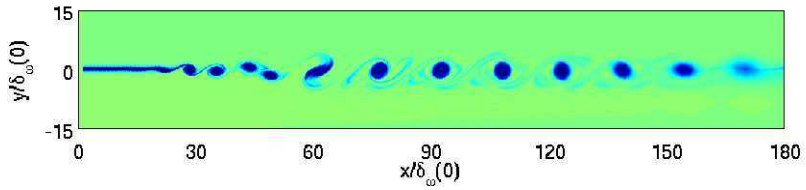

Figure 3.3: Total spanwise vorticity field in the near field. Levels from $5\times10^4\mathrm{s}^{-1}$ to $5 \times 10^4\mathrm{s}^{-1}$.

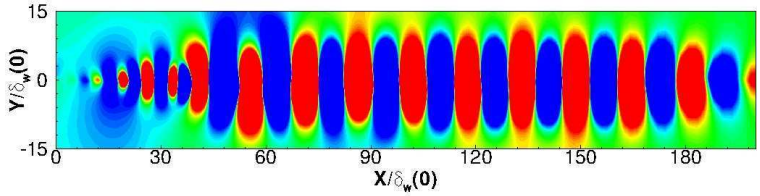

Figure 3.4: Source data during one pairing sampled from the DNS. Pressure fluctuations are shown.

from the DNS (figure 3.5 (a)), the radiation patterns from the acoustic analogy illustrate also that the acoustic waves emanate from the fixed vortex pairing locations. In addition, from figure 3.6, we observe a double spiral structure with four lobes, the sound generation mechanism is identified as a classical rotating quadrupole source. This is in consistence with the findings of Powell [92] and Mitchell, Lele & Moin [77], in which the noise production by a co-rotating vortex pair was investigated theoretically and numerically. The radiated sound from the acoustic analogy is seen to be well predicted by the acoustic analogy qualitatively. To gain an insight into a quantitative knowledge of the acoustic wave propagation in the far field, the sound pressure level, namely directivity, will be measured in the acoustic far field. It is given in decibel according to

$$SPL = 20 \log_{10} \left(\frac{p'_{rms}}{p'_{ref}} \right) \tag{3.2}$$

where $p'_{ref} = 2 \times 10^{-5}$ Pa represents the standard reference sound pressure in the air and p'_{rms} is the root mean square (r.m.s.) values which was integrated during one pairing period T_{app} after the saturated regime. The directivity is then evaluated by interpolating the values p'_{rms} in the equidistant points on an arc of radius $110\delta_\omega(0)$ from the apparent source location: $(x, y) = (64\delta_\omega(0), 0)$. This apparent source location corresponds to the vortex pairing zone which is responsible for the acoustic radiation ([20]). The directivities from DNS and using the acoustic analogy are plotted in figure (3.7). For the upper stream, the peak acoustic radiation appears at $\theta \approx 44°$ from DNS calculation while $\theta \approx 46°$ from the acoustic analogy. And the lower angles lobe at $\theta \approx -45°$ from DNS, at $\theta \approx -43°$ from analogy prediction. Both the directivity and amplitude of the acoustic predictions are consistent with DNS results. The predictions from the acoustic analogy are found to be in good agreement with the acoustic field from the DNS both qualitatively and quantitatively. As a consequence, the DNS supplemented with convected formulation of FW-H acoustic analogy have been used to investigate the sound generated by vortex pairing in a forced mixing layer, and have been proven to been efficient to capture the acoustic wave propagation in the far field. We can be confident about the results obtained from the DNS validated by an appropriate acoustic analogy which are very important since the reduced-order models will be subsequently constructed from the DNS.

3.2 Linear model: global stability analysis

As mixing layers have shown to act as noise amplifiers which are very sensitive to external noise (Huerre & Monkewitz [57] and Huerre [54]), a linear model based on global modes is proposed in order to analyse this classical type of flow. On may remark that this study is performed on the parallel flow based on the hyperbolic tangent profile illustrated in section 3.1. A parallel stability theory is sufficient to determine the most unstable frequency and the corresponding spatial amplification rate. Nevertheless, the aim of the present work is to propose a general theory without any assumption about the flow configuration. A global stability analysis is then performed on such a flow and a precise comparison with a local theory is used to validate our method.

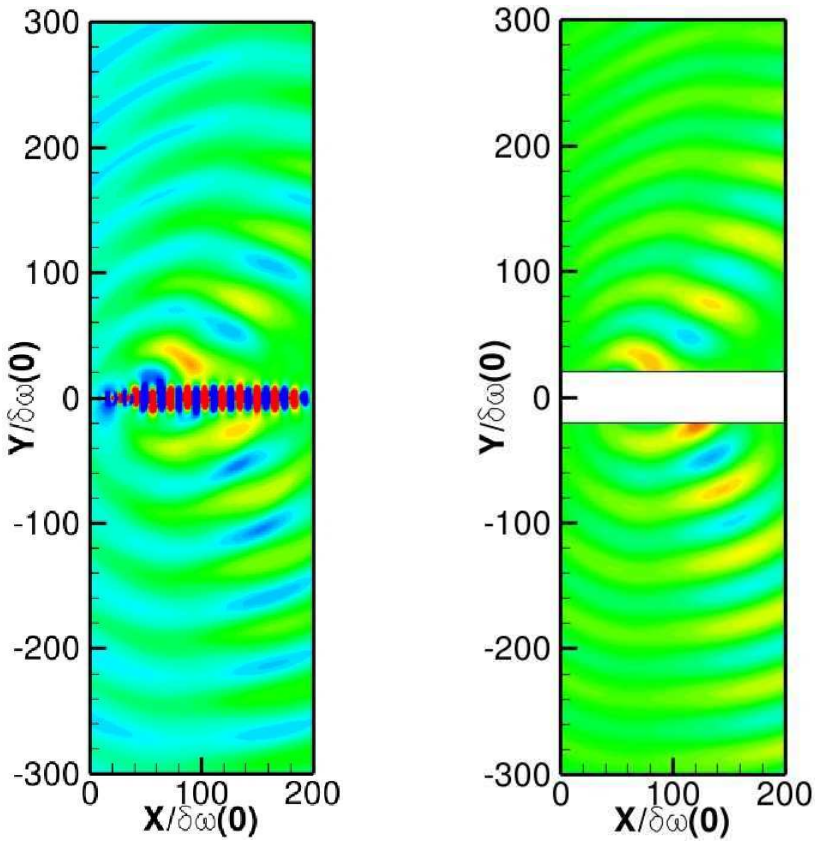

(a) (b)

Figure 3.5: (a)Fluctuating pressure from DNS. (b) Far-field acoustic predictions using the convected formulation of FW-H analogy. Levels from -100 Pa to 100 Pa in both figures.

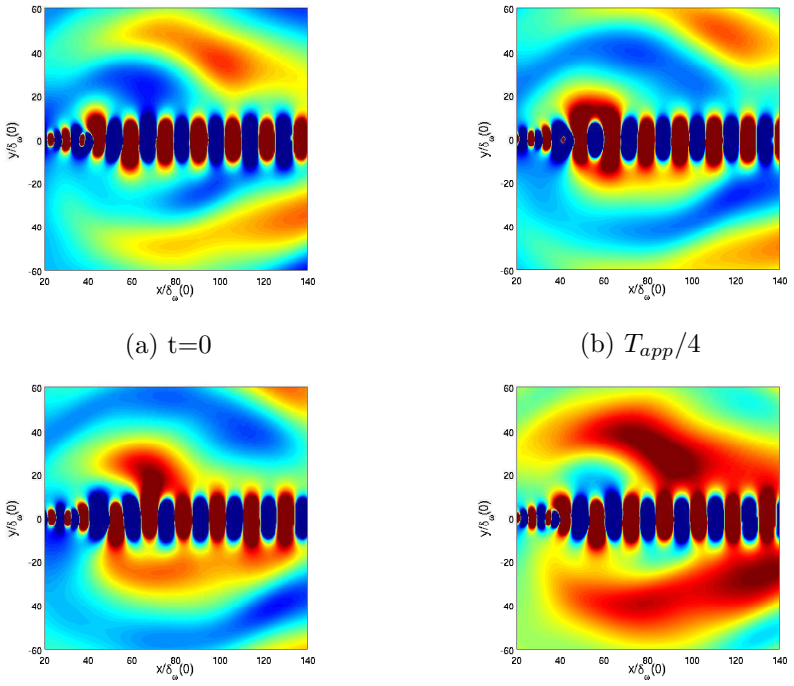

(a) t=0 (b) $T_{app}/4$

(c) $T_{app}/2$ (d) $3T_{app}/4$

Figure 3.6: Vortex pairing process during one pairing period T_{app} in the near-field mixing region from the DNS. Fluctuating pressures are shown.

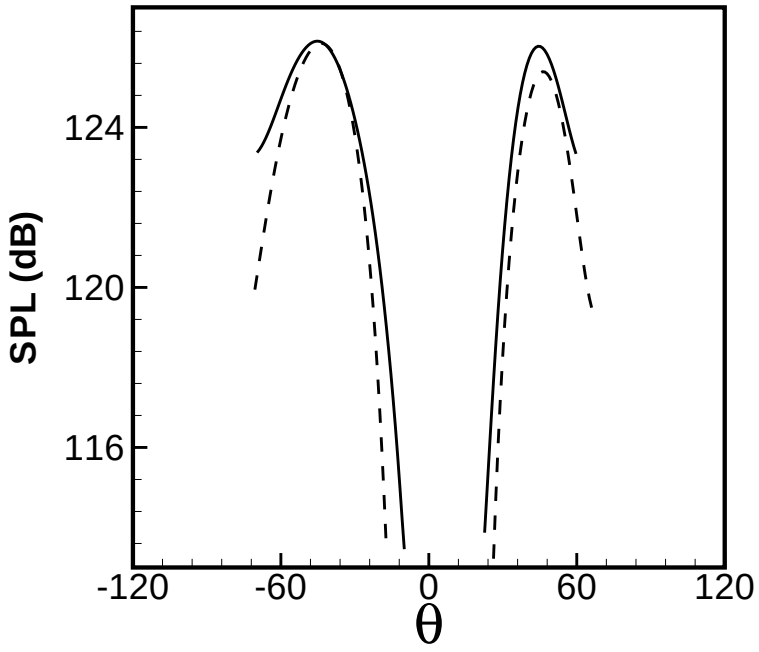

Figure 3.7: Far-field directivity for a radius at $110\delta_\omega(0)$ from the noise source located at $x = 64\delta_\omega(0)$ and $y = 0$ from DNS shown in solid line, using the acoustic analogy shown in dashed line.

3.2.1 Numerical parameters for linearized DNS

In this first series of calculation, a global stability analysis is used to compute the asymptotic behaviour of disturbances evolving near the steady-state solution i.e. the linear perturbation dynamics. For that purpose, the nonlinear terms in the perturbation convective fluxes (2.12) and (2.13) are neglected. In order to compute the global modes, a method based on the snapshots sampled from the linearized DNS is used. Because of the strong convective behaviour of the instability waves in the flow, 601×281 grid points in a computational domain $(L_x, L_y) = (130, \pm 90)\delta_\omega(0)$ excluding the sponge zone are employed. This choice allows to include maximum flow dynamics in the streamwise direction. The grid in x is uniform with spacing $\Delta x_{min} = 0.32\delta_\omega(0)$ up to $x = 130\delta_\omega(0)$. The grid is highly stretched in the sponge zones. In the normal direction, the grid is stretched at 1.8% from $\Delta y_{min} = 0.16\delta_\omega(0)$ in the shear region around $y = 0$ to large $\pm y$. To absorb the eventual outgoing acoustic waves with minimal reflection in the downstream directions, sponge layers defined in (2.20) are used at the outflow boundary, extending from $x = 130\delta_\omega(0)$ to $x = 300\delta_\omega(0)$. The damping coefficient of the Laplacian filter γ_{max} in (2.20) is chosen for 0.4. We have verified that the instability waves corresponding to f_0 and $f_0/2$ are resolved using 25 and 12 grid points, respectively, which are well discretized by our eleven-point stencil DRP scheme.

3.2.2 Coherent structures associated with the global modes

In this section, coherent structures associated with the global modes are investigated through the linear stability analysis. These global eigenmodes of the mixing layer are computed by making use of the Arnoldi algorithm presented in chapter 2. We first consider the influence of several numerical parameters on the computation of the global mode decomposition. Then, the noise-amplifier-type dynamics in a global approach is examined either by a temporal analysis or a frequency domain analysis.

In modal decomposition analyses, the sampling period Δt in the input data sequence is a crucial parameter. The separation should be chosen properly to reflect the characteristic time scale of the physical flow structures. On one hand, to avoid aliasing Δt should be small enough to discretize accurately higher harmonics in the flow given by the Nyquist criterion. On the other hand, the temporal separation should not be too close between the consecutive snapshots since additional snapshots make no further improvement. In this way, Δt is chosen as a balance between the time scale and a sufficient temporal separation of the Krylov vectors to ensure convergence of the iterative method. Based on these observations, the sampling period in the present investigation is fixed to $\Delta t = 13\delta t$ (recall that δt is the time step from the DNS), which guarantees up to $2f_0$ resolution.

Another subtle issue in the computation of global modes by Arnoldi algorithm is the choice of a norm. It is well known that the energy is a convenient quantity to measure the growth of a disturbance. We thus introduce energy-based inner products. For incompressible flows, the standard inner product is directly related to the kinetic energy, the technique is well-known:

$$(\hat{\mathbf{q}_1}, \hat{\mathbf{q}_2})_E = \int_\Omega \left[\frac{1}{2} \rho_b (\hat{u_1}^* \hat{u_2} + \hat{v_1}^* \hat{v_2}) \right] dV \tag{3.3}$$

where the superscript $*$ denotes the complex conjugate. Then the square of the energy norm is defined as

$$\|\hat{\mathbf{q}}\|^2 = (\hat{\mathbf{q}}, \hat{\mathbf{q}}) = E \tag{3.4}$$

For instance Day, Mansour & Reynolds [36] used this kind of inner product to measure the energy of the mode. By contrast, this is not the case for compressible flows, in which no obvious definition of disturbance measures is available. Indeed, not only the kinematic variables are important, both thermodynamic and kinematic variables contribute to the total energy, and must be taken into account. Moreover, how to combine these two variables in a rational way is not immediately apparent. Some choices of inner products for compressible flows are considered. For instance, Rowley, Colonius & Murray [96] have introduced a family of energy-based inner products for isentropic flows. By altering a parameter, they choose to use the integral of the stagnation enthalpy or the stagnation energy as the norm. In this thesis, we define the following form as the compressible inner product that includes both kinetic and internal energies.

$$(\hat{\mathbf{q}_1}, \hat{\mathbf{q}_2})_E = \int_\Omega \left[\frac{1}{2} \rho_b (\hat{u_1}^* \hat{u_2} + \hat{v_1}^* \hat{v_2}) + \frac{\hat{p_1}^* \hat{p_2}}{p_b(\gamma - 1)} \right] dV \tag{3.5}$$

Note that the right-hand side of (3.5) is quadratic. We plot the global modes spectra resulting from these two inner products using the same dimension of Krylov subspace $N = 180$, as shown in figure 3.8. In this figure, the temporal growth rate ω_i of each eigenvalue is less than zero, which means that all of the modes are temporally damped and hence the flow is globally stable. From a local point of view, this globally stable flow is locally convectively unstable because perturbations are constantly transported away from the unstable region. This flow belongs to the noise amplifier class. The connection between the local and global theories has been reviewed by Huerre & Monkewitz [57]. It is also worth noting that the inner product choice has a limited impact on the spectra. This observation is in accordance with our low-Mach-number flow configuration (recall that the convective Mach number in question is $M_c = 0.176$).

Now, the convergence behaviour of the Arnoldi algorithm is illustrated as the number of snapshots N is increased. The global residual of the algorithm is displayed in figure 3.9 (a). Again, we notice that the choice of inner products has no influence on the convergence behaviour of the Arnoldi algorithm. Also, we observe a rapid convergence : at least 160 snapshots are needed. But, if we continue to add snapshots to the Krylov suspace, the residual begins to climb. This may be related to the fact that the Hessenberg matrix is a highly non-normal matrix, which results in an ill-conditioned eigenvalue problem for increasing number of snapshots (an overall discussion of non-normal operators is provided in Trefethen [115]). From figure 3.9 (a), the range from $N = 160$ to $N = 180$ seems to show a good convergence with the residual $< 10^{-10}$ evaluated by (2.30). We plot the eigenvalue spectra as the number of snapshots is increased in this area from $N = 180$ to $N = 200$ to $N = 220$ in figure 3.9 (b). We remark that, apart from $N = 180$, the spectra for $N = 200$ and $N = 220$ begin to pile up for high frequencies. High frequencies are not resolved for more number of

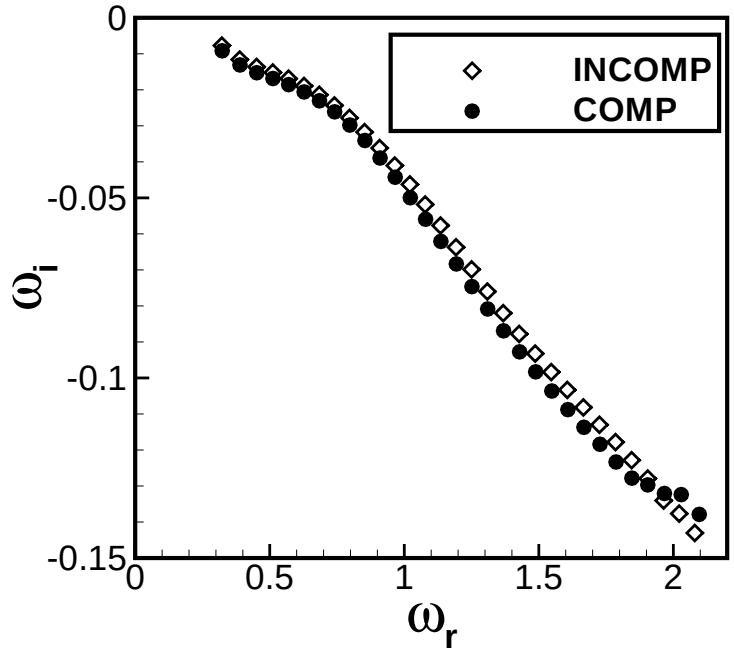

Figure 3.8: Effect of inner product on the eigenvalue spectrum: ◊, incompressible inner product; •, compressible inner product.

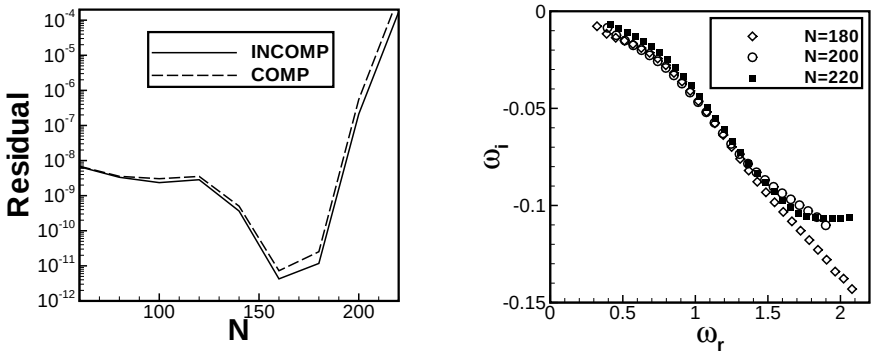

(a) (b)

Figure 3.9: (a) Global residual history of the Arnoldi algorithm with respect to the incompressible inner product (solide line) and compressible inner product (dashed line) as a function of number of snapshots N. (b) Effect of Krylov subspace basis of dimension N on the eigenvalue spectrum.

snapshots. Therefore, 180 snapshots appears to be a good compromise between low and high frequency resolution.

Another important numerical parameter is the choice of streamwise extent. We now demonstrate how the choice of the domain size in the streamwise direction affects the computed global spectrum. based on empirical observations. Thus, three domains of lengths $L_x = 162$, $L_x = 192$ and $L_x = 222$, labelled L_1, L_2 and L_3, respectively are considered. In all cases, the cross-stream extent is fixed as $L_y = 200$. Figure 3.10 (a) shows the global spectra obtained for these three domains. We observe that the temporal growth rate increases as the streamwise extent is increased as well. This can be explained by the strong difference in magnitude between the largest and smallest components (more than about 10^{10} times in our case, see figure 3.14). This phenomenon can be caused by the non-normality of the underlying global evolution operator, and hence strong exponential growth of the global mode eigenvectors displayed in the streamwise direction. Also, we find that the branch of the global mode spectrum is always situated below zero if we continue increasing L_x, but the residual rises again (see figure 3.10 (b)). This is because as the convective non-normality of the system also increases, leading to the increasing residual as L_x increases. These are in consistence with the empirical observations by Heaton, Nichols & Schmid [49] and Bagheri *et al.* [7]. Therefore, to obtain the longest domain to represent the maximum wavelengths of the global mode with a comparatively good convergence property, L_3 turns out to be a good compromise with a global residual equals to 10^{-11}. Furthermore, the fact that a characteristic length along streamwise direction is only associated with the size of the computation domain and not an intrinsic spatial inhomogeneity of the flow leads to a spatial dependency of the spectrum according to the streamwise length L_x.

Given the above parameter studies, $N = 180$ snapshots and $L_3 = 222$ seem to be an appropriate choice for the reference case.

Figure 3.11 show two examples of eigenvectors at two different angular fre-

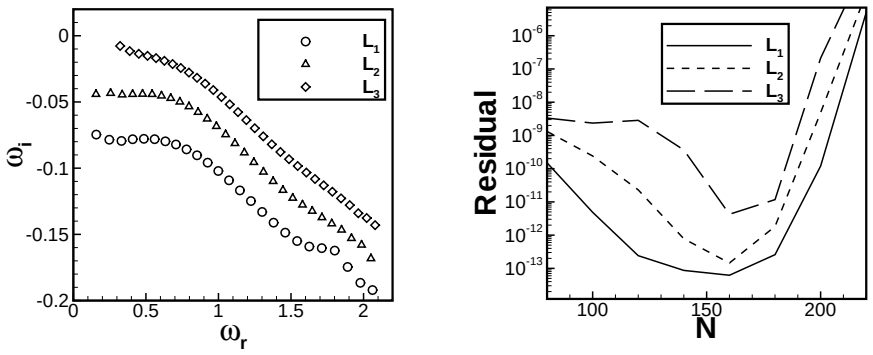

(a) (b)

Figure 3.10: (a) Eigenvalue spectra for three domain lengths: ∘,$L_1 = 162$; △, $L_2 = 192$; ♢, $L_3 = 222$. (b) Corresponding global residual history with respect to the three streamwise domain sizes: L_1, L_2, and L_3.

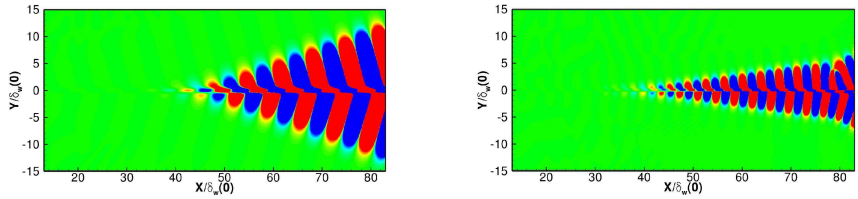

(a) (b)

Figure 3.11: (a) Streamwise velocity component u' of the eigenfunction corresponding to the mode at the angular frequency $\omega_r = 2\pi f_0 = 0.852$. (b) Streamwise velocity component u' of the eigenfunction associated with the mode at a higher angular frequency $\omega_r = 1.606$.

quencies. The wavelength decreases as the angular frequency ω_r increases, which satisfies the dispersion relation. Moreover, as a consequence of the convective nature of the instabilities arising in the mixing layer, where disturbances grow in amplitude as they are convected in the downstream direction, the global eigenmodes are located far downstream, with the largest flow energy.

3.2.3 Temporal analysis: wavepacket dynamics

To characterize the noise amplifier dynamics which is sensitive to external forcing exhibited by the mixing layer, we distinguish between two main approaches: the flow response to a wavepacket localized in space and time in the transient regime, and to a harmonic forcing in the asymptotic regime (Cossu & Chomaz [31]). In this section, we first consider the flow response to a localized impulse in a mixing layer. Thus, an initial perturbation of the form

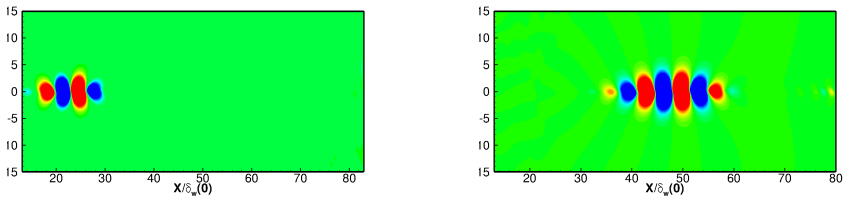

(a) (b)

Figure 3.12: (a) A snapshot from the DNS at initial time $t = 0$. (b) Snapshot of the travelling wavepacket at later time $t_1 > t = 0$. Pressure fluctuations are illustrated in both figures.

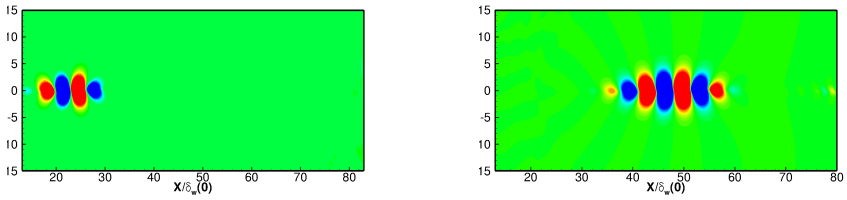

(a) (b)

Figure 3.13: (a) Projected linear response at initial time of the mixing layer to an initial velocity disturbance localized at $(x = 20\delta_\omega(0), 0)$. (b) The wavepacket at later time $t_1 > t = 0$ by using (2.42). Real parts of the pressure fluctuations are shown in both figures.

$$u'(x, y, t = 0) = \alpha U_c \exp\left[-\ln 2 \frac{(x-20)^2 + y^2}{(3\Delta y_{min})^2}\right] \tag{3.6}$$

with amplitude $\alpha = 10^{-10}$, is introduced into the shear layer at $(x = 20\delta_\omega(0), 0)$. The convection velocity is $U_c = 100$ m/s. Disturbances grow in amplitude and propagate downstream for increasing time, resulting in the form of a localized wavepacket. The system (2.23) can be simplified by projecting the linearized Navier–Stokes equations onto a subpace of dimension m, in which the projected perturbation field $\mathbf{q}'(\mathbf{x}) = (\rho', u', v', w', p')^T$ is governed by the system defined in (2.23)

We perform a projection onto a set of $m = 30$ global modes using the orthogonal projection detailed in the previous chapter. The efficiency of the orthogonal projection onto the basis of global modes can be illustrated by depicting the pressure perturbation components in figures 3.12 and 3.13. A snapshot of the wavepacket resulting from the impulsive streamwise velocity perturbation at the inlet of the shear layer from the linearized DNS at initial time $t = 0$ and its projection are shown in figures 3.12 (a) and 3.13 (a). At later time $t_1 > t = 0$, the wavepacket is seen to propagate downstream. The advected wavepacket and its projection obtained from our model (2.42) are shown in figures 3.12 (b) and 3.13 (b). From these figures, we can see that our orthogonal projection procedure is very competitive.

As demonstrated by Cossu & Chomaz [31] in their examination of the linear stability of the Ginzburg-Landau operator with spatially varying coefficients, the streamwise non-normality of global eigenmodes resulting from the local convective instability may produce substantial transient growth of perturbation energy. This non-normality of the linear evolution operator associated with the streamwise separation between the adjoint and direct global modes was first revealed by Chomaz [28] because of the basic flow advection. The adjoint operator $\mathcal{A}^*$ verifying $< \mathbf{q}_a, \mathcal{A}\mathbf{q}_b > = < \mathcal{A}^*\mathbf{q}_a, \mathbf{q}_b >$ for any $\mathbf{q}_a$ and $\mathbf{q}_b$, the operator $\mathcal{A}$ is non-normal if it does not commute with its adjoint

$$\mathcal{A}\mathcal{A}^* \neq \mathcal{A}^*\mathcal{A} \tag{3.7}$$

This short-time, transient behavior often corresponds to a local convective instability within a local framework. We plot the temporal evolution of the perturbation energy $E(t)/E(0)$ in figure 3.14. It is interesting to point out a considerable exponential growth of the energy in the initial stage, and again this tendency is not affected by the choice of the inner products. Through this temporal analysis by considering the flow response to a localized impulse, we see that no sound is produced by the subsonic mixing layer within the linear approach. An additional nonlinear mechanism is responsible for the acoustic radiation. This is not the case for the supersonic jet flows where Mach waves can directly radiate to the far field in the linear regime (Tam & Morris [113], Tam & Burton [110] and Nichols & Lele [85]).

3.2.4 Analysis in frequency domain: response to harmonic forcing

Since the mixing layer behaves as a noise amplifier which is very sensitive to the external forcing, it is then more natural to resort to the frequency domain to characterize the flow response to the external perturbations by exploring the spectral content (Alizard [1], Monokrousos *et al.* [81]). To model this type of excitation in a global stability approach, a certain external forcing term $\mathbf{f}$ is added to the system resulting from the linearization of the Navier-Stokes (2.23).

Let us consider $\mathbf{f} = \hat{\mathbf{f}}e^{-i\omega_f t}$ a small-amplitude forcing, characterized by a forcing angular frequency ω_f and the spatial structure $\hat{\mathbf{f}}$. Concretely, it has the following form

$$v'(x, y, t = 0) = \alpha U_c \sin(\omega_f t) \exp\left[-\frac{y^2}{(\Delta y_{min})^2}\right] \tag{3.8}$$

with amplitude $\alpha = 10^{-12}$, is introduced near the plane $i = 6$. We shall consider the flow response $\mathbf{q}'$ governed by the following harmonically forced problem

$$\frac{\partial \mathbf{q}'}{\partial t} = \mathcal{A}\mathbf{q}' + \mathbf{f} \tag{3.9}$$

The general solution to this problem consists of a homogeneous and a particular part

$$\mathbf{q}' = \mathbf{q}'_0 e^{it\mathcal{A}} - i(\mathcal{A} - \omega_f I)^{-1}\hat{\mathbf{f}}e^{-i\omega_f t} \tag{3.10}$$

$\mathbf{q}'_0$ depends on the initial conditions. As all eigenvalues of $\mathcal{A}$ are damped temporally, the solution has an asymptotic long-time response

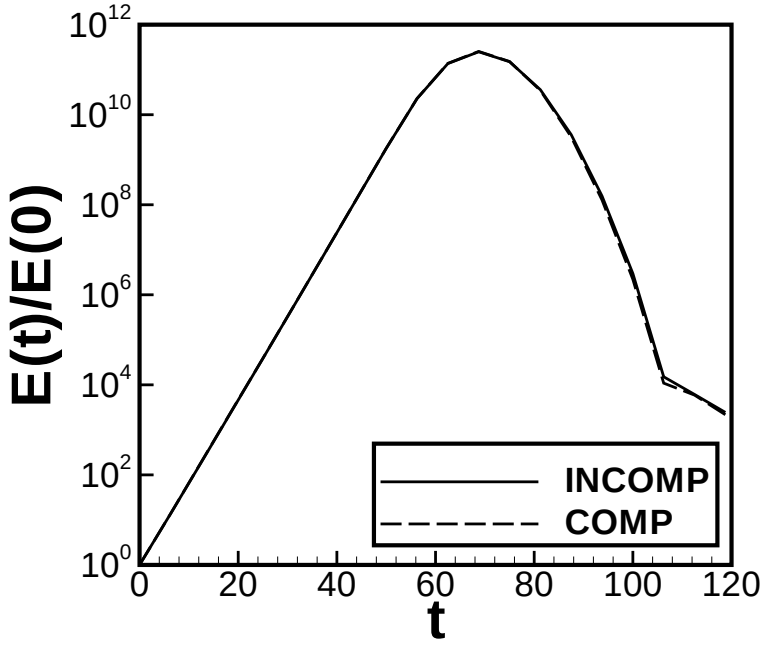

Figure 3.14: Disturbance energies $E(t)/E(0)$ with respect to the incompressible inner product (solid line) and compressible inner product (dashed line) a function of time.

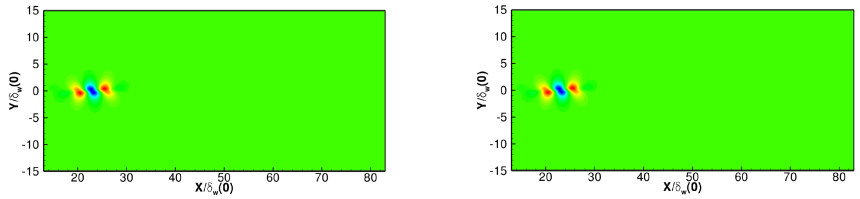

(a) (b)

Figure 3.15: (a) Forcing term. (b) Projected forcing term, demonstration of the accuracy of the projected forcing term onto the global basis. Real parts of the normal velocity perturbations are displayed.

$$\mathbf{q}' = -i(\mathcal{A} - \omega_f I)^{-1}\hat{\mathbf{f}}e^{-i\omega_f t} \tag{3.11}$$

Similarly to the superposition of global modes, the forcing term is decomposed in the basis of global modes, and reads

$$\hat{\mathbf{f}} = \sum_{k=0}^{m-1} K_k^f \hat{\mathbf{q}_k} \tag{3.12}$$

Likewise, the flow response can also be decomposed in the basis of global modes:

$$\hat{\mathbf{f}} = \sum_{k=0}^{m-1} K_k \hat{\mathbf{q}_k} e^{-i\omega_f t} \tag{3.13}$$

where the two coefficients K_k^f and K_k are related by:

$$K_k = \frac{K_k^f}{i\omega_f - i\omega_k}$$

In the asymptotic regime, the response of the flow due to the forcing becomes

$$\mathbf{q}' = -\sum_{k=0}^{m-1} K_k i(\mathcal{A} - \omega_f I)^{-1}\hat{\mathbf{q}_k}e^{-i\omega_f t} \tag{3.14}$$

We project the forcing term in the orthonormalized basis through an orthogonal projection as before. The forcing term has been chosen to take the shape of a wavepacket located at the inlet in the streamwise direction, the cross-stream components of the velocity perturbation before and after the projection are shown in figure 3.15. The good agreement between these two implies that the forcing term has been well projected in the basis of global modes.

To measure the response of a linear system described by $\mathcal{A}$ to a harmonic forcing at a real frequency ω_f, we introduce the following quantity

$$R(\omega_f) = \frac{\|\mathbf{q}'\|^2}{\left\|\hat{f}\right\|^2} \tag{3.15}$$

R is defined with respect to the norm induced by either incompressible or compressible inner products defined previously. The response for each frequency

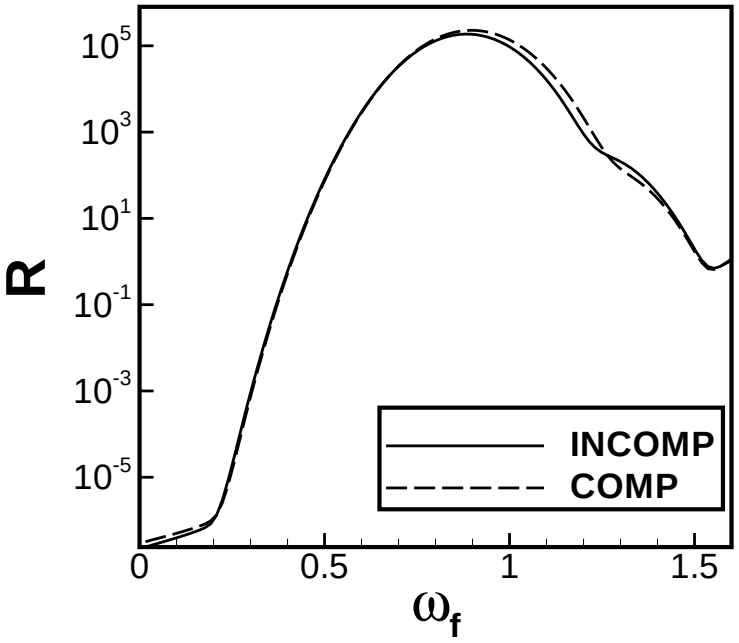

Figure 3.16: Frequency response to the harmonic forcing. Incompressible inner product: solide line, compressible inner product: dashed line.

using these two inner products is evaluated in figure 3.16. In both situations, a pronounced peak for the fundamental frequency $\omega_r = 0.88$ is observed as expected. This phenomenon is in agreement with the local spatial stability analysis performed by Michalke.

Figure 3.17 and figure 3.18 show the temporal evolutions of the asymptotic response to the forcing term $\omega_f = 2\pi f_0$ and $\omega_f = 2\pi f_0/2$ respectively. The corresponding spatial structures are illustrated. In both situations, no acoustic radiation is observed.

Certain stability properties of the instability waves, such as the wavelength, wavenumber or growth rate obtained from the global modes computation can be validated by performing a local stability analysis. First, the wavelength of the instability wave at f_0 can be obtained by depicting the streamwise evolution of the real part of its normal velocity perturbations $v_r{}'$ along the centerline, shown in figure 3.19 (a). The corresponding wavelength is thus derived from: $\alpha = 2\pi/\lambda = 2\pi/7.31 = 0.86$. Then, the temporal growth rates of f_0 and $f_0/2$ are determined by applying a linear regression of $|(v_r'(x, y = 0)|$: 0.27 and 0.19, shown in figure 3.20 (a). Simultaneously, these instability waves are obtained by solving the parallel flow linear stability problem at each streamwise location. It is defined by the following Rayleigh equation in a compressible regime (see Jackson & Grosch [58] and Criminale, Jackson & Joslin [33]):

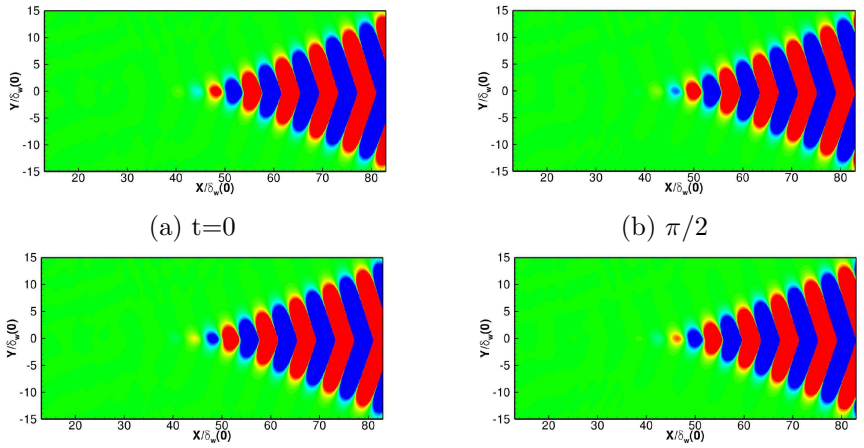

(a) t=0 (b) $\pi/2$

(c) π (d) $3\pi/2$

Figure 3.17: Asymptotic response to the forcing term : $\omega_f = 2\pi f_0$. Real parts of the pressure fluctuations at four instants over one cycle are plotted.

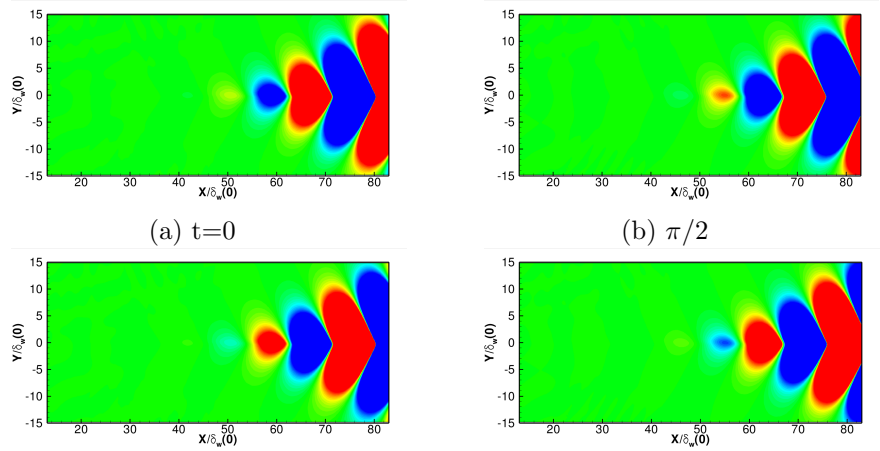

(a) t=0 (b) $\pi/2$

(c) π (d) $3\pi/2$

Figure 3.18: Asymptotic response to the forcing term : $\omega_f = 2\pi(f_0/2)$. Real parts of the pressure fluctuations at four instants over one cycle are plotted.

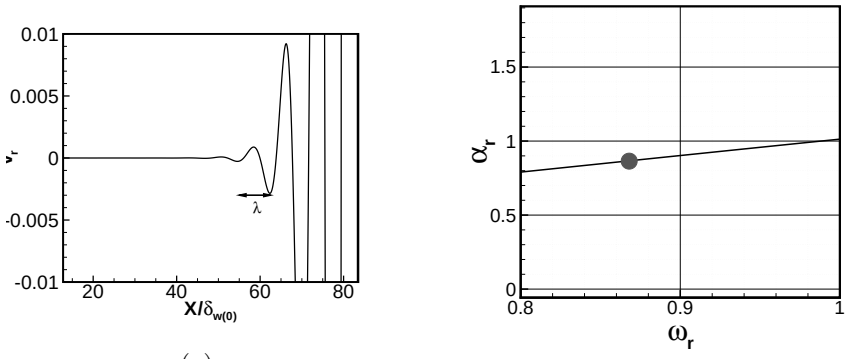

(a) (b)

Figure 3.19: (a) Real part of the normal velocity perturbations $v'_r(x, y = 0)$ at the fundamental frequency f_0 as a function of streamwise distance from the global modes stability analysis. (b) Wavenumber α_r as a function of the angular frequency ω_r from the local stability analysis.

$$\frac{d^2p'}{dy^2} + \left[-\frac{1}{\rho_0}\frac{d\rho_0}{dy} + \frac{2\alpha}{(\omega - \alpha u_0)}\frac{du_0}{dy}\right]\frac{dp'}{dy} + \left[\rho_0(\alpha u_0 - \omega)^2 {M_c}^2 - \alpha^2\right]p' = 0 \tag{3.16}$$

The stability analysis yields the value of the wavenumber for f_0: 0.89 (figures 3.19 (b)) and temporal growth rates $\sigma = -\alpha_i$ for f_0 and $f_0/2$: 0.24 and 0.19 (figure 3.20 (b)). We find again the forcing angular frequency ω_f that leads to a maximum gain. Given these comparisons, we can conclude that for a given instability mode (close to the most unstable or the subharmonic mode) the wavelength and temporal growth rate are correctly predicted by the linear analysis based upon the global modes. Therefore, the present method is validated and should be efficient to deal with other flow configurations where the parallelism hypothesis could not be verified. Nevertheless, one may remark that the difficulty to converge the spectrum was expected since the pioneer work of Cossu & Chomaz [31]. The latter authors illustrated, through a Ginzburg-Landau equation, that an increasing of the parallelism of the flow leads to an increase of the non-normality according to the streamwise direction. As a consequence, the Jacobian matrix $\mathcal{A}$ is more ill-conditioned when the flow is fully parallel.

The eigenmodes behaviour can also be examined by comparing their integrated modal energy from the direct calculation and global stability analysis. To this end, the energy of the eigenmode of interest from the direct computation is transformed in frequency domain by means of a Fourier discrete transform, and instability wave energies are computed accordingly

$$\hat{\mathbf{q}}(x, y, \omega_m) = \frac{1}{N}\sum_{j=0}^{N-1} \mathbf{q}'(x, y, t_j)\, e^{-i\omega_m t_j} \tag{3.17}$$

The period $T = 2\pi/\omega_m$ at the frequency of interest ω_m is discretized by N samples. This procedure is achieved by using DFT Lapack library. The instability

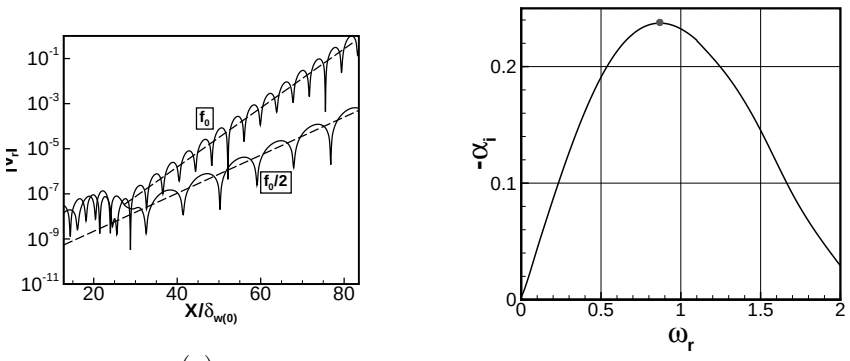

(a) (b)

Figure 3.20: (a) Global modes analysis: logarithmic plots of the streamwise evolution of the real part of the normal velocity perturbations $|(v'_r(x, y = 0)|$ for frequencies f_0 and $f_0/2$. Linear regressions are depicted in long dashed lines. (b) Local stability analysis: temporal growth rate versus the angular frequency.

wave energy is computed by every portion in $x-$ direction using (3.3). The local measure of the perturbation energy E at each streamwise station obtained from the fully nonlinear DNS is displayed in figure 3.21. Focused on the linear stage, we see that the two instability waves associated with f_0 and $f_0/2$ grow both exponentially. However, f_0 grows with more energy and more abruptly than $f_0/2$. This tendancy is in good agreement with the behaviours of eigenmodes observed in figure 3.20 (a). One may observe that, beyond the initial exponential growth region, both of the eigenmodes begin to saturate once they join the nonlinear stage of the flow.

Now we will see if this linear model produces sound when combining the two frequencies f_0 and $f_0/2$. Figure 3.22 shows the asymptotic response to this combined forcing through the total spanwise vorticity. No pairing phenomenon is observed. Thus we can conclude that the linear global modes analysis fail to model the vortex pairing mechanisms and consequently to predict the acoustic radiation. It appears that the nonlinearity must be incorporated to obtain an accurate description of vortex pairing process. The vital implications of nonlinear effects have also been observed by Cheung & Lele [26], who compared the linear PSE with or without the mean flow correction and nonlinear PSE simulations of a two-dimensional mixing layer. Nevertheless, we should recognize the efficiency of the global modes stability analysis in predicting stability characteristics for any flow configurations. The DMD analysis will be performed within a fully nonlinear framework in the next section.

3.3 Nonlinear model: DMD analysis

The above linear global stability computation in which only the linear effects are accounted for has been proven to be insufficient to capture accurately the shear layer dynamics and consequently its acoustic behaviour. The inclusion

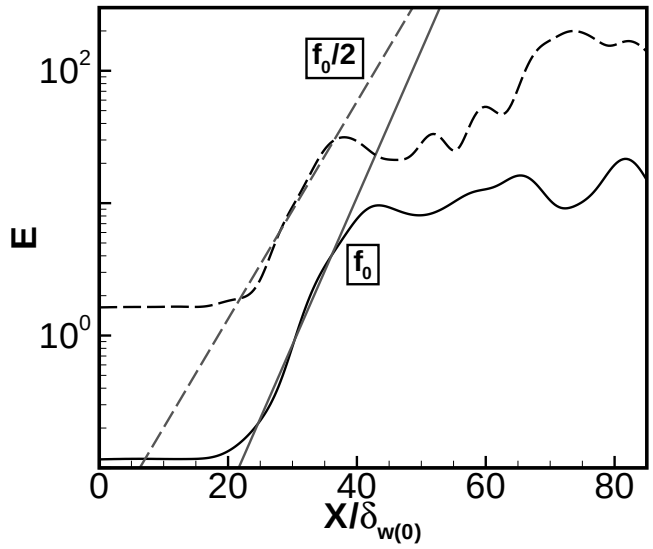

Figure 3.21: Modal energy E for the fundamental mode f_0 and first subharmonic $f_0/2$ with Fourier analysis from the fully nonlinear DNS calculation.

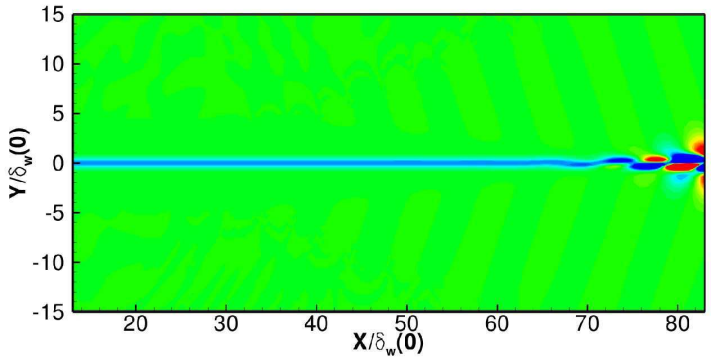

Figure 3.22: Asymptotic response to the combined forcing for f_0 and $f_0/2$. Total spanwise vorticity are shown.

N	$f_0/2$	f_0	$3f_0/2$	$2f_0$
100	0.416	0.831	1.247	1.663
150	0.416	0.834	1.249	1.667
200	0.418	0.837	1.248	1.664
250	0.417	0.835	1.252	1.672
300	0.417	0.834	1.258	1.667

Table 3.1: Peak values of the angular frequency ω_r as the number of snapshots N is increased from 100 to 300 using the compressible inner product.

of nonlinear interactions between modes seems necessary to recover both the hydrodynamics and aeroacoustics of the mixing layer. As pointed out in chapter 2, the nonlinear model consists in carrying out the DMD analyses within a temporal and spatial framework. The dynamic information associated with the coherent structures extracted from these two analyses will thus be illustrated.

3.3.1 DMD analysis within a temporal framework: coherent structures extraction

The analysis is performed for the entire domain. 300 snapshots of the density, velocity and pressure fluctuations at a sampling rate $\Delta T = 1.36 \times 10^{-5}$ s are saved during the direct computation. This sampling rate corresponds to 17 samples per pairing period T_{app} and ensures especially the resolution of higher harmonics in the flow. As we are in compressible flow regime, both incompressible and compressible inner products defined in (3.5) will be tested in the DMD algorithm. Tables 3.1 and 3.2 list the dominant values of angular frequency ω_r when the number of snapshots N is increased from 100 to 300 by using these two inner products. We observe that each peak frequency is almost stagnant and the choice of norm does not affect the values of the maximum frequencies. The latter remark is in consistence with the fact that we are in presence of a low-Mach-number flow ($M_c = 0.176$ in our flow configuration). Afterwards, 300 snapshots and the incompressible inner product will be used. The eigenvalues are displayed in figure 3.23 (a). Nearly all the Ritz values are found to lie on the unit circle $|\lambda_j| = 1$, which means that the sample points lie on or near an attracting set. Figure 3.23 (b) plots the energies of the extracted modes as a function of the frequency. Since the Koopman eigenvalues appear in complex conjugate pairs, we only show their positive parts. Each mode represented by its norm is depicted with a vertical line. The peak frequencies containing highest energy are then identified and marked with the symbols $1, 2, 3, 4$, which have the same colouring as in the eigenvalues plots. These peak modes are referred as to the the first subharmonic $f_0/2$, the fundamental mode f_0, the harmonic $2f_0$, and marked 1, 2 and 4, respectively. Higher modes are also excited because of all linear combinations of the frequencies, for instance, the nonlinear interaction of $f_0/2$ and f_0 results in $3f_0/2$ marked 3 and so on.

These four representative Koopman modes as well as the mode 0 corresponding to the mean perturbation will be projected onto the initial DNS data to obtain their respective weight:

N	$f_0/2$	f_0	$3f_0/2$	$2f_0$
100	0.416	0.831	1.247	1.663
150	0.416	0.834	1.250	1.667
200	0.418	0.842	1.248	1.667
250	0.417	0.835	1.252	1.672
300	0.417	0.834	1.258	1.672

Table 3.2: Peak values of angular frequency ω_r as the number of snapshots N is increased from 100 to 300 by using the incompressible inner product.

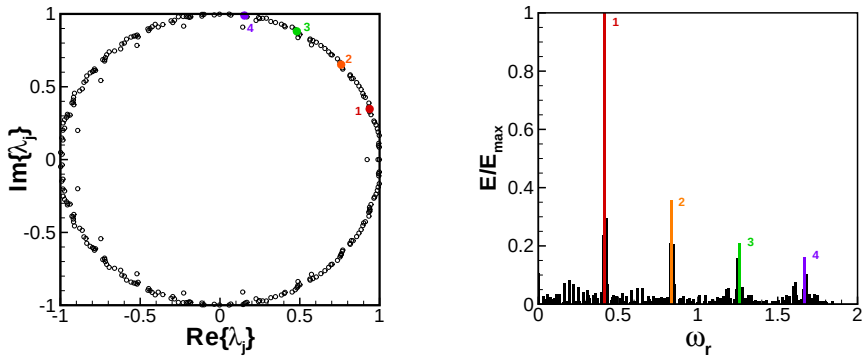

(a) (b)

Figure 3.23: DMD analysis performed over the entire computational domain using 300 snaphots: (a) Ritz values λ_j. (b) Energy spectrum of the Koopman modes at each angular frequency ω_r. In both figures, the Ritz values associated with the most energetic modes are marked with 1, 2, 3 and 4, respectively.

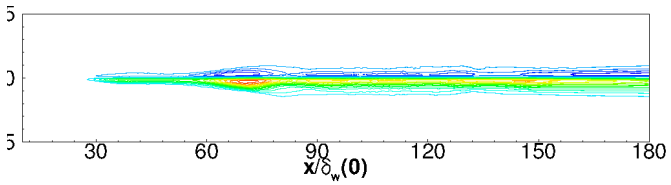

Figure 3.24: The real part of the vorticity fluctuations for the Koopman mode at zero frequency is depicted.

$$\mathcal{P} = (\mathbf{q}', \mathbf{q}'_0) \tag{3.18}$$

where $(,)$ represents the incompressible inner product defined in (3.3). $\mathbf{q}'$ is any projected Koopman mode onto the initial data $\mathbf{q}'_0$ from the DNS. The Koopman mode associated with the zero frequency is shown in figure 3.24. One may observe that it corresponds to the mean deformation of the perturbation due to nonlinear effects. It has for consequence to increase the mean vorticity thickness of the mixing layer along the streamwise position. As expected, no acoustic radiation is observed for this particular mode.

The projected modes in both the entire and the near-field domains are displayed using the pressure fluctuations component in figures 3.25, 3.26, 3.27 and 3.28, respectively. We immediately observe that the acoustic waves at $f_0/2$ emanate from the region where the pairings occur (figure 3.25). Besides, the modes f_0, $3f_0/2$ or $2f_0$ produce little far-field noise (see levels in figures 3.26, 3.27 and 3.28), compared to the mode at $f_0/2$. Therefore, the first subharmonic mode contribute mainly to the acoustic radiation in the mixing layer. An another observation is also made: when forcing the flow with f_0 and $f_0/2$, these structures associated with the Koopman modes can radiate sound directly to the far field which totally differ from the global modes from the linear analysis. Therefore, the DMD analysis in this nonlinear approach appears a relevant tool to describe accurately the aeroacoustics of the mixing layer.

Now, to assess the ability of the DMD analysis to describe the spatial and temporal structures, the associated dispersion relation that relates frequencies of waves to their corresponding wavenumbers will be examined through a local stability analysis. We first consider the evolutions of the two dominant modes $f_0/2$ and f_0 by plotting the modal energy defined in (3.3) as a function of x. The results are shown in figure 3.29. In the linear region before the vortex roll up, the growth of f_0 dominates over $f_0/2$. And for each of the fundamental and first subharmonic this exponential growth of the energy is followed by saturation and then decay. The saturation of the fundamental frequency, f_0, and its subharmonics $f_0/2$ occurs near $x = 35$, 60, respectively. The developments of these modes can also be confirmed by depicting the streamwise variations of their pressure perturbations inside the sheared near-field region (along the centerline $y = 0$), shown in figures 3.30 and 3.31, respectively. During the initial linear exponential growth region, the mode f_0 exibits a stronger growth rate than that of $f_0/2$. Then, the wavelength of the instability waves at the frequency of interest is obtained through a spatial Fourier analysis. The corresponding wavenumber α_r can be derived from the relation: $\alpha_r = 2\pi/\lambda$. In this way, the dispersion relation can be illustrated by plotting the wavenumber

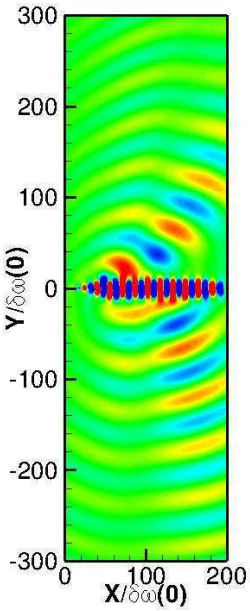

(a)

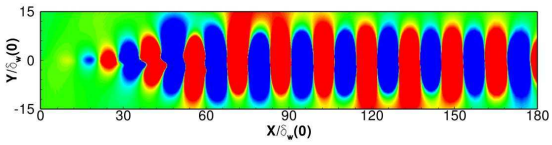

(b)

Figure 3.25: (a) Real part of the pressure fluctuations for Koopman mode at $f_0/2$. Levels are shown from -80 Pa to 80 Pa. (b) A zoom in of this mode inside the near-field region.

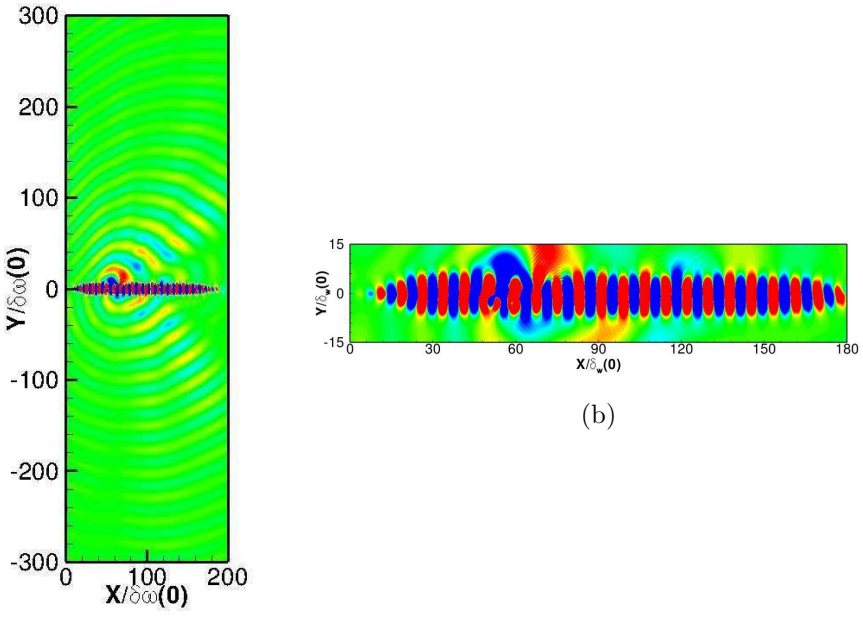

(a) (b)

Figure 3.26: Real part of the pressure fluctuations for Koopman mode at f_0. Levels are shown from -30 Pa to 30 Pa. (b) A zoom in of this mode inside the near-field region.

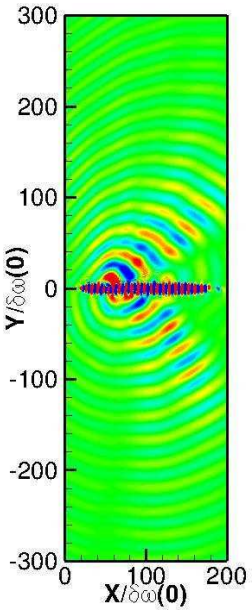

(a)

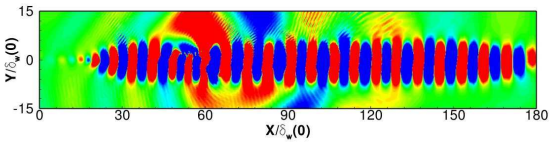

(b)

Figure 3.27: Real part of the pressure fluctuations for Koopman mode at $3f_0/2$. Levels are shown from -20 Pa to 20 Pa. (b) A zoom in of this mode inside the near-field region.

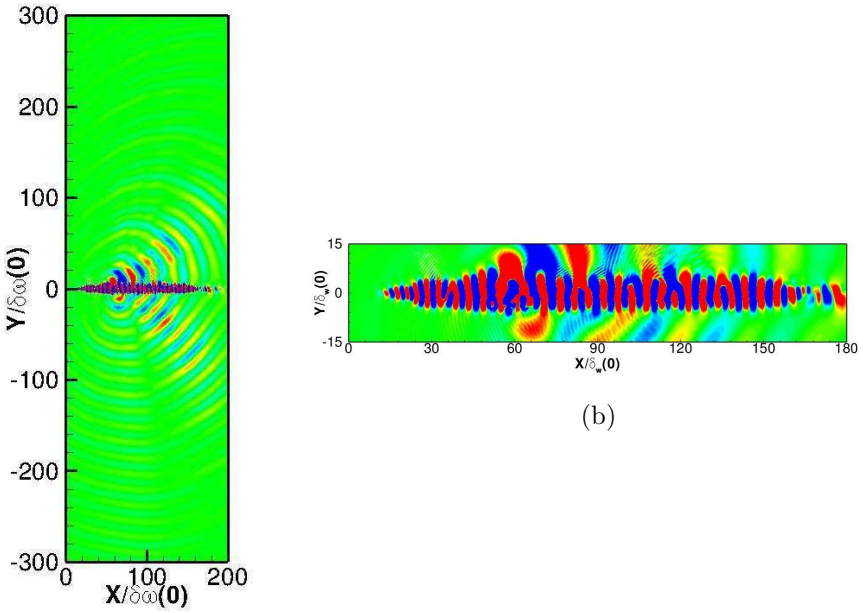

(a)

(b)

Figure 3.28: Real part of the pressure fluctuations for Koopman mode at $2f_0$. Levels are shown from 5 Pa to 5 Pa. (b) A zoom in of this mode inside the near-field region.

α_r as a function of the angular frequency ω_r varying from $f_0/2$ to $2f_0$, shown in figure 3.32. At the same time, we use the compressible Rayleigh equation in (3.16) to describe the instability waves of the shear layer. The stability analysis is performed on the actual mean profile measured from the DNS rather than the hyperbolic tangent profile. Note that Rowley, Colonius & Basu [95] found a good agreement between the linear stability calculations with respect to the DNS mean flow velocity profiles and the DNS in his investigation of cavity flow oscillation. In our case, we proceed in two regions separately: one is in the principal exponential growth region of f_0, say $0 < x/\delta_\omega(0) < 20$, one is in the region where $f_0/2$ dominates: $30 < x/\delta_\omega(0) < 36$. The isocontours of the temporal growth rate σ and wavenumber α_r as a function of the frequency and the streamwise location inside the first region, are depicted in figure 3.33 and 3.34, respectively. During the first region, nearly all the maximum temporal growth rates tends towards the value of angular frequency ≈ 0.88 corresponding to the value of f_0. The value agrees quite well with $\omega_r \approx 0.83$ derived from the figure 3.32. The most unstable instability waves develop at the frequency f_0 as the mixing layer evolves downstream. In the second region, figure 3.35 gives the angular frequency of the most unstable instability waves: $f_0/2 \approx 0.4$, which is the dominant mode this time. The wavenumbers from DMD and local stability analyses compare also well. The temporal growth rates are found to decrease with respect to the streamwise station, this can be explained by the saturations of their instability waves. The behaviours of these waves can be validated by the mean streamwise velocity plot in the near-field region of the mixing layer, shown in figure 3.37. The thickness of the layer is basically seen to double in the vicinity of the locations where the pairings occur. This nonparallelism of the mixing layer confirm our choice of the stability analysis on the real mean flow. Based on the above examinations, we can conclude that the Koopman modes responsible to describe the dynamics of large-scale vortical structures are accurately calculated by the DMD analysis.

3.3.2 Reconstruction of the flow dynamics through the DMD analysis

Until now, we have demonstrated that the DMD analysis was capable of describing accurately the coherent structures associated with the Koopman modes. In this section, we wish to reconstruct the entire shear layer dynamics in both the near and far fields. Considering the non-orthogonality of the Koopman modes, an orthogonal projection onto the Koopman modes basis will be employed, as used in the linear global modes analysis. By increasing gradually the number of modes m, we show for instance the time traces of the pressure fluctuations at the pairing location $(x, y) = (64\delta_\omega(0), 0)$ during 3 pairing periods (figure 3.38). It is seen that the difference between DNS and DMD calculations becomes smaller when the number of modes m involved in the recovery procedure is increased. In particular, the temporal evolution of the pressure $p'(t)$ can be almost recovered by the DMD analysis with 50 modes superimposed on the zero-frequency mode (Cheung & Lele [26]). This mean flow correction is the mode at zero frequency, which has been shown to play an important role in the flow dynamic and thus should be taken into account (Noack *et al.* [87] and Sipp & Lebedev [103]). Besides, we have verified that the addition of the base flow to this zero-frequency mode yields the real mean flow. Furthermore, the need

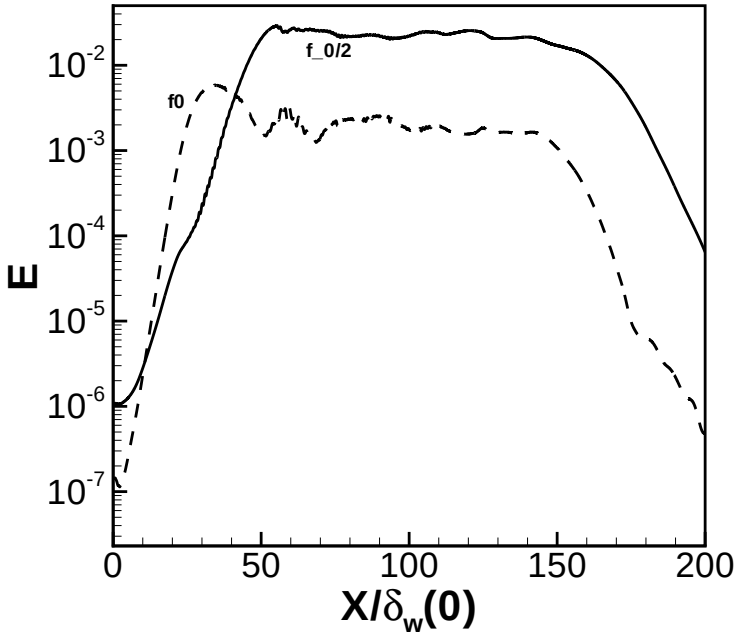

Figure 3.29: Streamwise evolution of energies E of the dominant modes at $f_0/2$ and f_0. Modal energy for the fundamental mode f_0 in dashed lines, the first subharmonic mode $f_0/2$ in solid line.

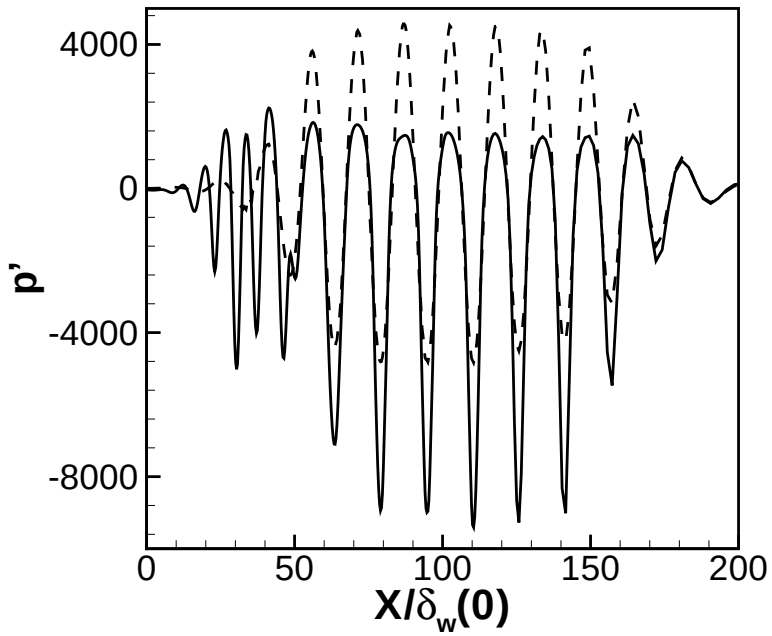

Figure 3.30: Streamwise evolution of the fluctuating pressure $p'(x)$ along the centerline $y = 0$ for the Koopman mode $f_0/2$. Perturbations from DNS are shown in solid line, perturbations from DMD are depicted in dashed line.

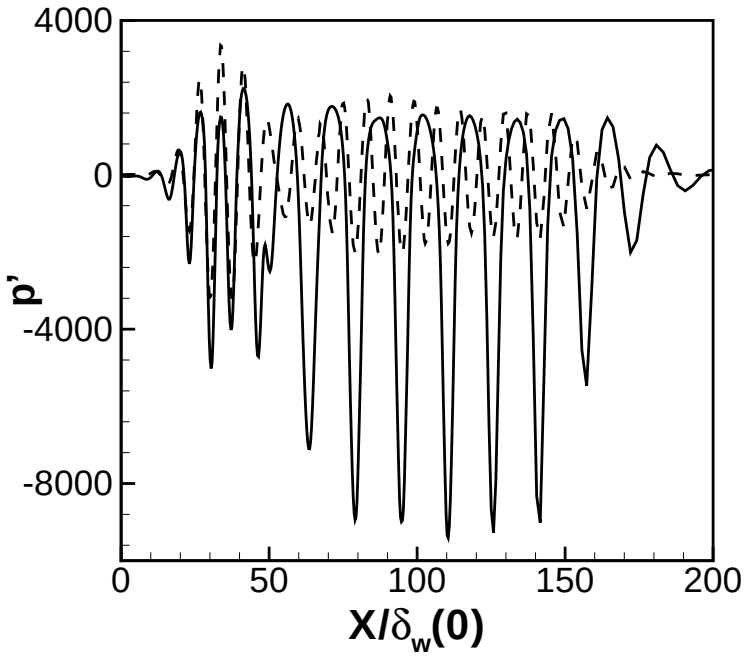

Figure 3.31: Streamwise evolution of the fluctuating pressure $p'(x)$ along the centerline $y = 0$ for the Koopman mode f_0. Perturbation from DNS are shown in solid line, perturbations from DMD are depicted in dashed line.

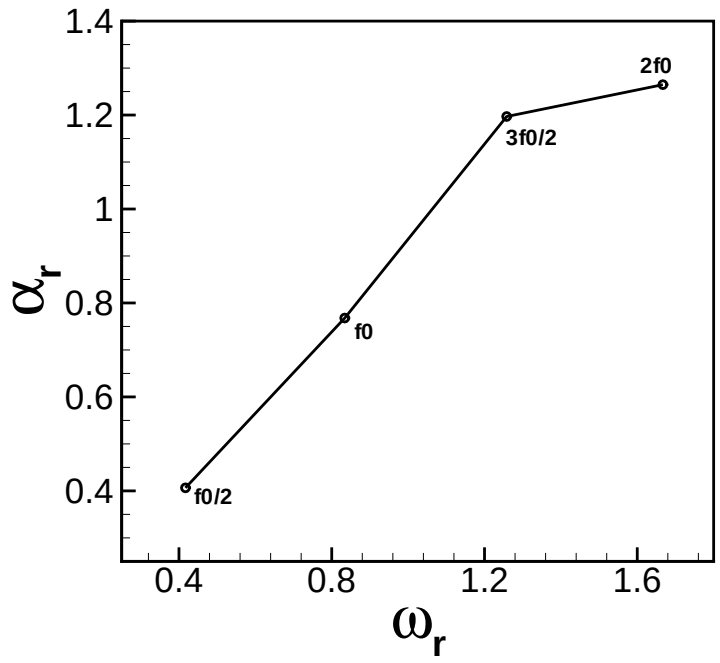

Figure 3.32: The wavenumber α_r is plotted as a function of the angular frequency ω_r. The four dominant modes are indicated in circles.

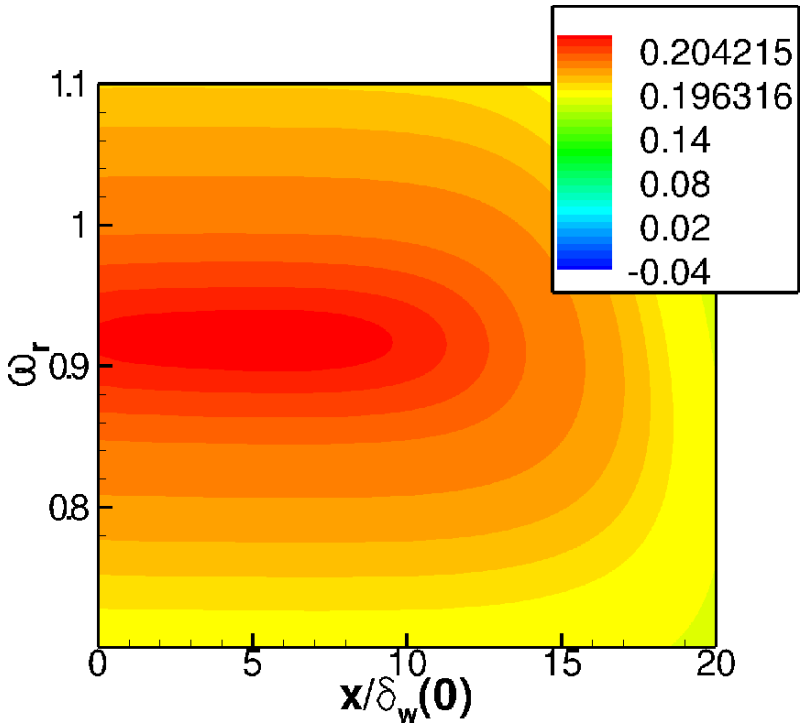

Figure 3.33: Isocontours of temporal growth rate σ as a function of the angular frequency ω_r and streamwise position $x/\delta_\omega(0)$.

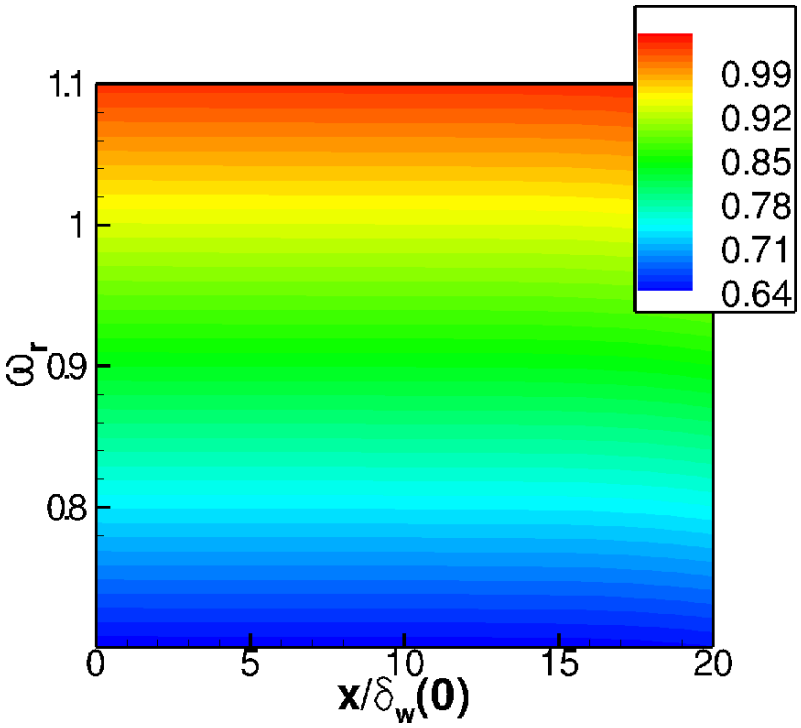

Figure 3.34: Contours of constant wavenumber α_r as a function of the angular frequency ω_r and streamwise position $x/\delta_\omega(0)$.

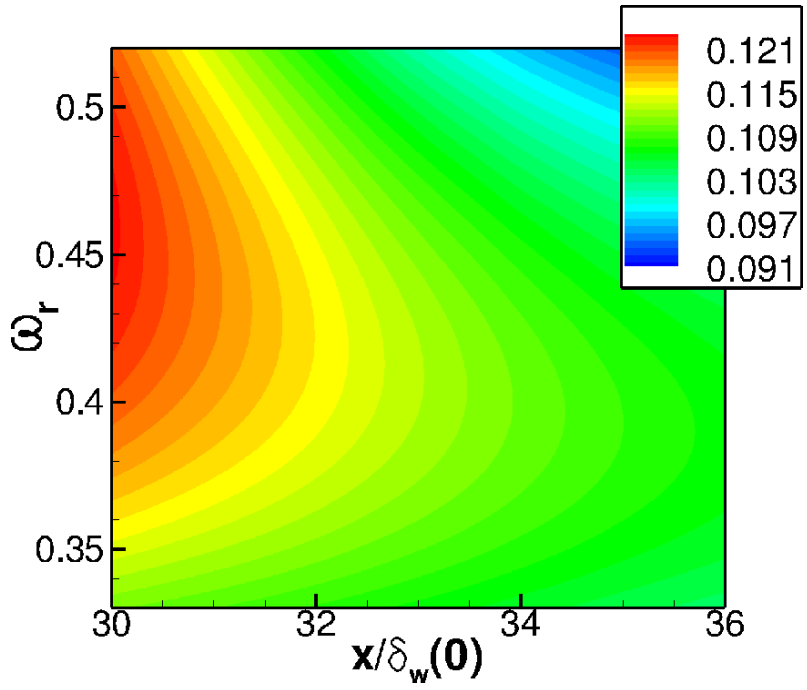

Figure 3.35: Contours of constant temporal growth rate σ as a function of the angular frequency ω_r and streamwise position $x/\delta_\omega(0)$.

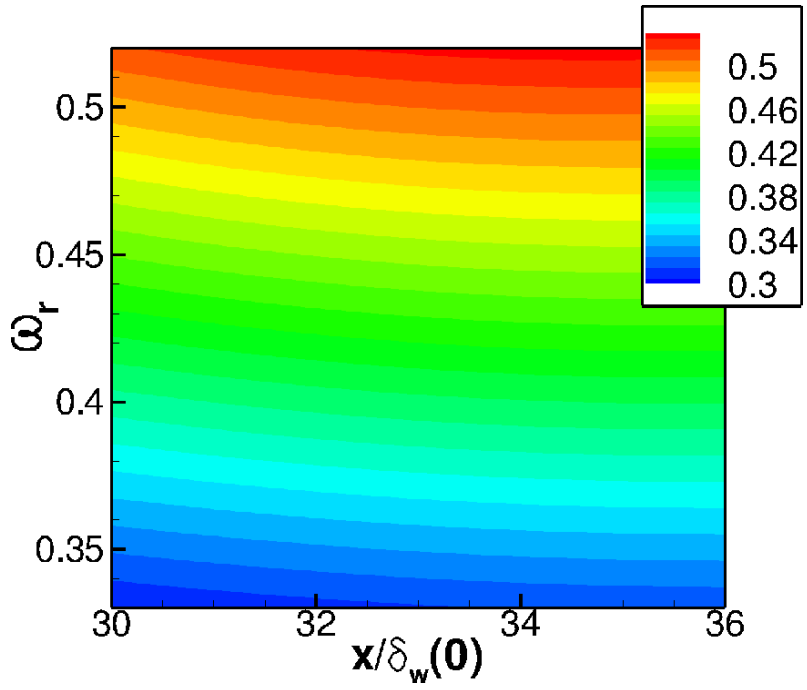

Figure 3.36: Isocontours of wavenumber α_r as a function of the angular frequency ω_r and streamwise position $x/\delta_\omega(0)$.

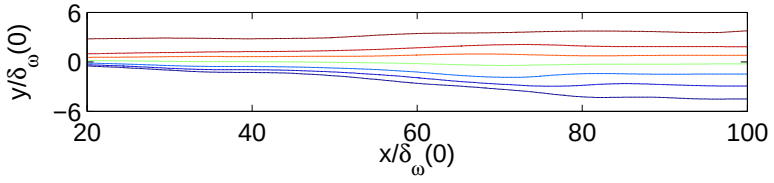

Figure 3.37: Mean streamwise velocity contours in near-field mixing region. Contour values are 44, 52, 68, 100, 132, 148, 152 m/s.

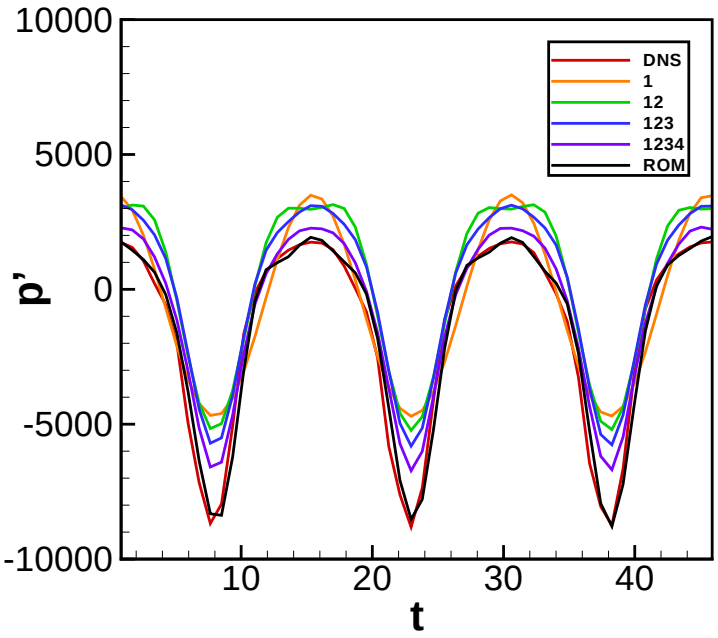

Figure 3.38: Time history of the pressure fluctuations $p'(t)$ at the pairing location $(x, y) = (64\delta_\omega(0), 0)$. In red, from DNS calculation; in orange, mode 1; in green, mode 1 and 2; in blue, mode 1, 2 and 3; in violet, mode 1,2, 3 and 4; in black, with 50 modes.

to account for the higher harmonics and modal interaction becomes apparent to recover the full underlying flow dynamics.

Moreover, the influence of the number of modes m on the flow dynamics reconstruction can be ascertained by defining a residual r that is based on the difference between the projected quantity $\mathbf{q}'$ whatsoever the density, velocity or pressure fluctuations, and the initial snapshot of perturbations $\mathbf{q}'_0$ obtained from DNS:

$$\mathbf{r} = \frac{\| \mathbf{q}' - \mathbf{q}'_0 \|}{\| \mathbf{q}'_0 \|} \tag{3.19}$$

The residuals r with respect to the streamwise velocity and pressure fluctuation are thus plotted in figures 3.39 and 3.40, respectively. The residuals are observed to drop significantly with the increase of the number of the modes. Especially, the two plots fall abruptly when adding the 22-th mode to the reconstruction procedure. There is no specific meaning for this mode. This phenomenon may be understood by the fact that sometimes to obtain a better projection additional information shall be added to the spatial support of the Koopman modes basis. Satisfactory results for 50 modes are obtained: $r \approx 10^{-4}$ for the streamwise velocity perturbations u' and $r \approx 10^{-2}$ for the pressure perturbations p'. Beyond 50 modes, the residuals reach a plateau where no further improvement

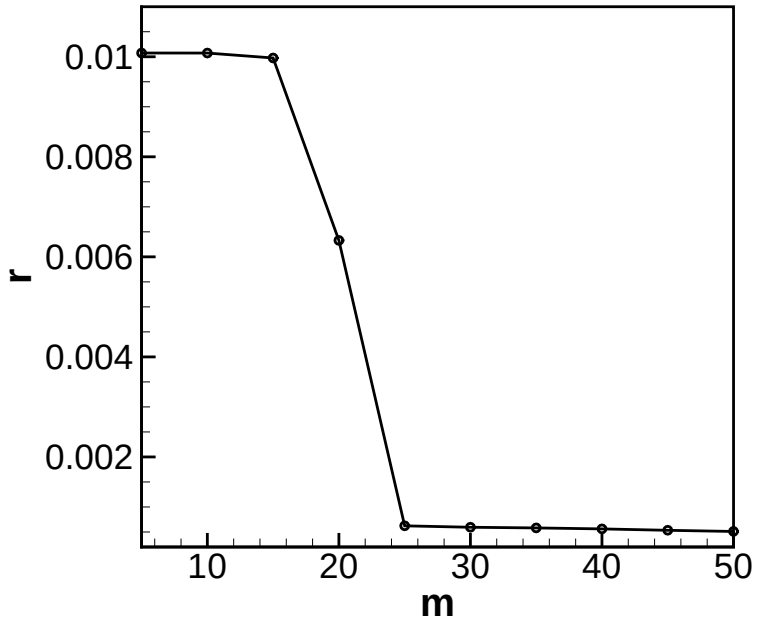

Figure 3.39: Residual history of the streamwise velocity fluctuation u' as a function of number of Koopman modes m used in the projection.

is present with additional modes. Therefore, 50 modes will be used hereafter in the following investigation.

As before, we first examine the ability of the DMD analysis to capture the hydrodynamic motions in the near field. A qualitative assessment of the vortex pairing mechanism is provided by the total spanwise vorticity plots at four successive equidistant instants during one period in figure 3.42. When the results from the nonlinear DMD calculations (figure 3.41) are compared against their directly computed counterparts, we see that both the roll-up and vortex pairing events seem to be quite well predicted by the DMD analysis. Cross-sections of the fluctuating pressure along the centerline ($y = 0$) in figure 3.43 provides a more quantitative examination of the spatial hydrodynamic behaviour of the mixing layer. Moreover, the temporal behaviour can be illustrated by plotting the fluctuating pressure at the center of the computational domain $(70\delta_\omega(0), 0)$ during five pairing periods in figure 3.44. From these figures, we can conclude that both the spatial and temporal behaviours of the mixing layer in the near-field are well predicted by the DMD computation.

We have examined the aerodynamic behaviour provided by the DMD computation. Now, it is of interest to investigate the acoustic behaviour prediction in the far-field. The pressure perturbations from DNS serving as the reference is plotted in figure 3.45 (a). The projected fluctuating pressure from DMD is depicted in figure 3.45 (b). We see that the acoustic patterns are very similar by using the same levels and that acoustic waves emanate from the same

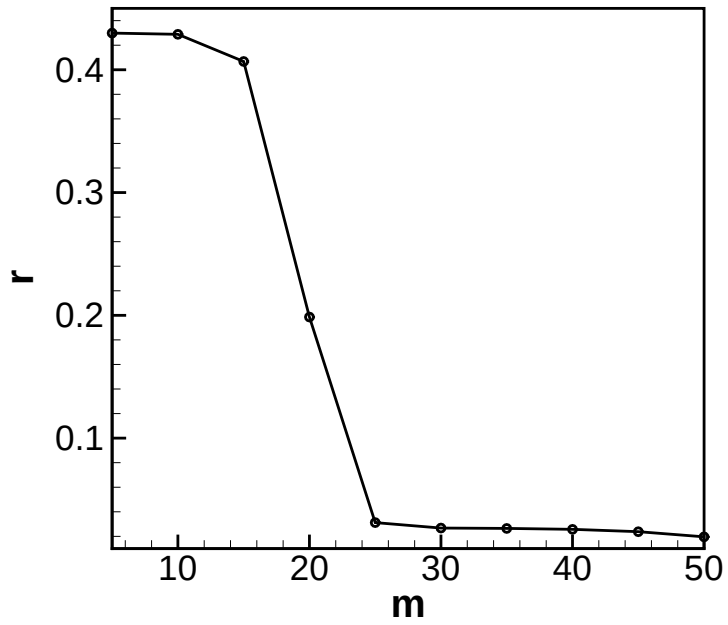

Figure 3.40: Residual history of the pressure fluctuation p' as a function of number of Koopman modes m used in the projection.

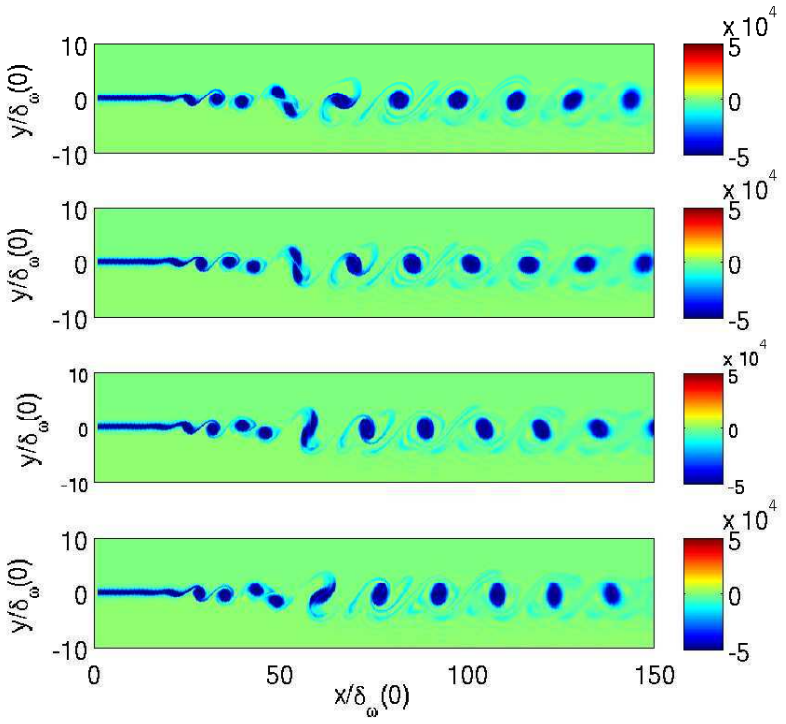

Figure 3.41: Follow-up of the vortex pairing at four successive equidistant instants during one pairing period in the near-field mixing region from DNS. Total spanwise vorticity is shown. Levels from -5×10^4 /s to 5×10^4 /s.

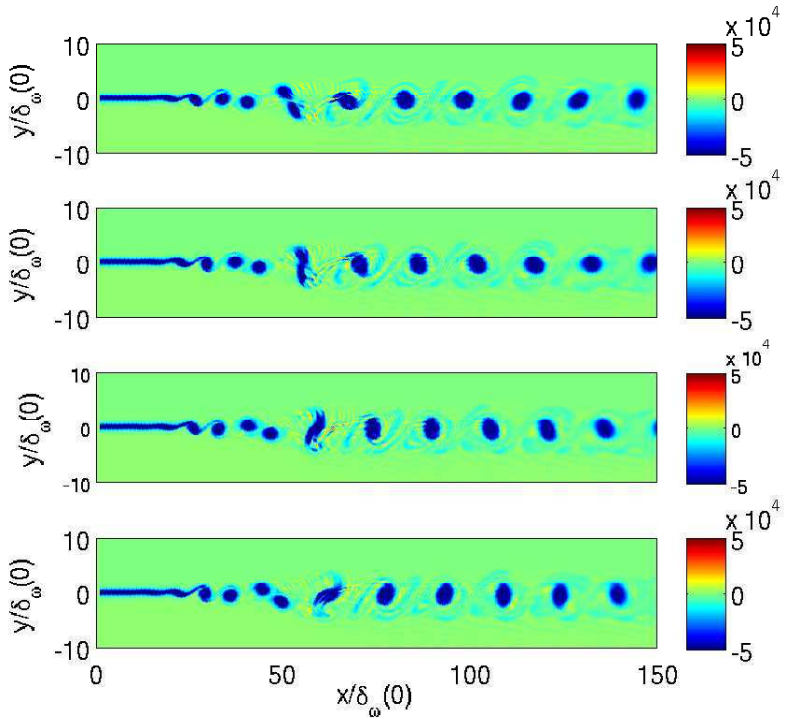

Figure 3.42: Follow-up of the vortex pairing at four successive equidistant instants during one pairing period in the near-field mixing region from DMD. Total spanwise vorticity is shown. Levels from -5×10^4 /s to 5×10^4 /s.

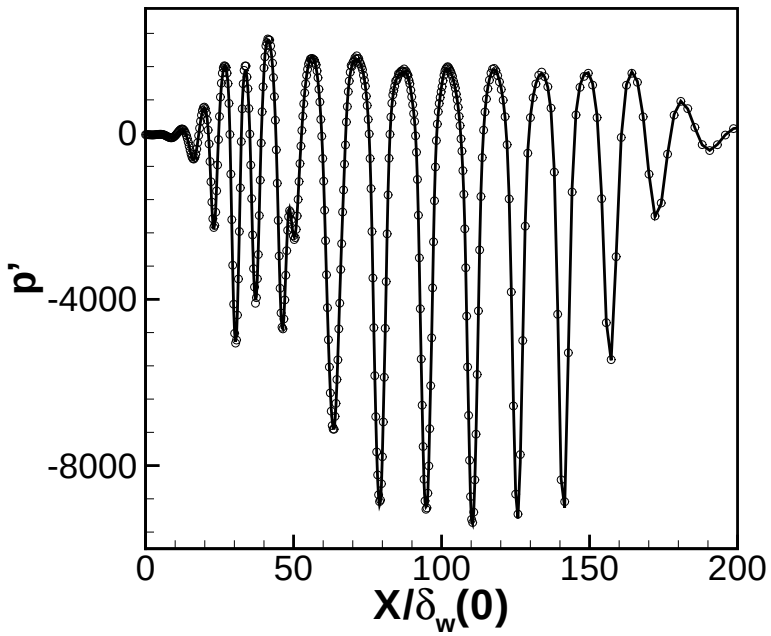

Figure 3.43: Cross-section of the pressure perturbations $p'(x)$ at the centerline $y = 0$. Perturbations from DNS are shown in solid line, perturbations from DMD are depicted in circles.

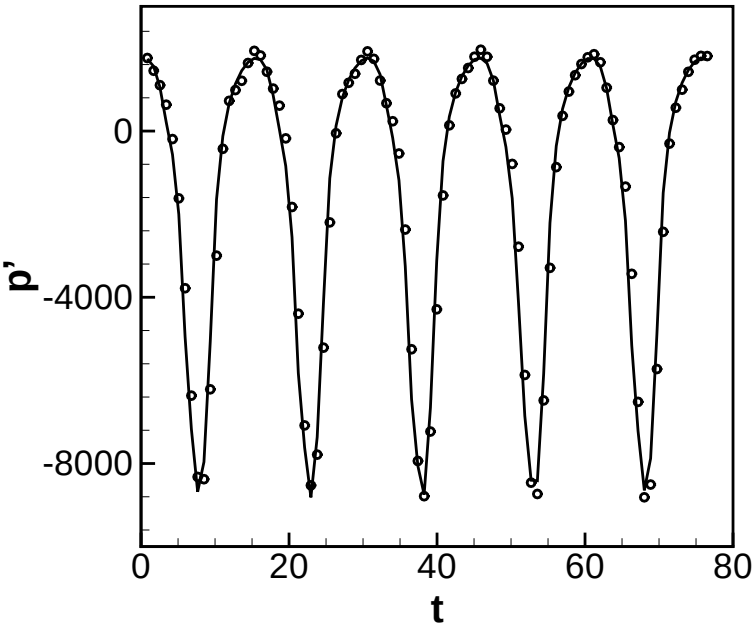

Figure 3.44: Cross-section of the pressure fluctuation $p'(t)$ at the center of the domain $(70\delta_\omega(0), 0)$ during five pairing periods. Perturbations from DNS are shown in solid line, perturbations from DMD are depicted in circles.

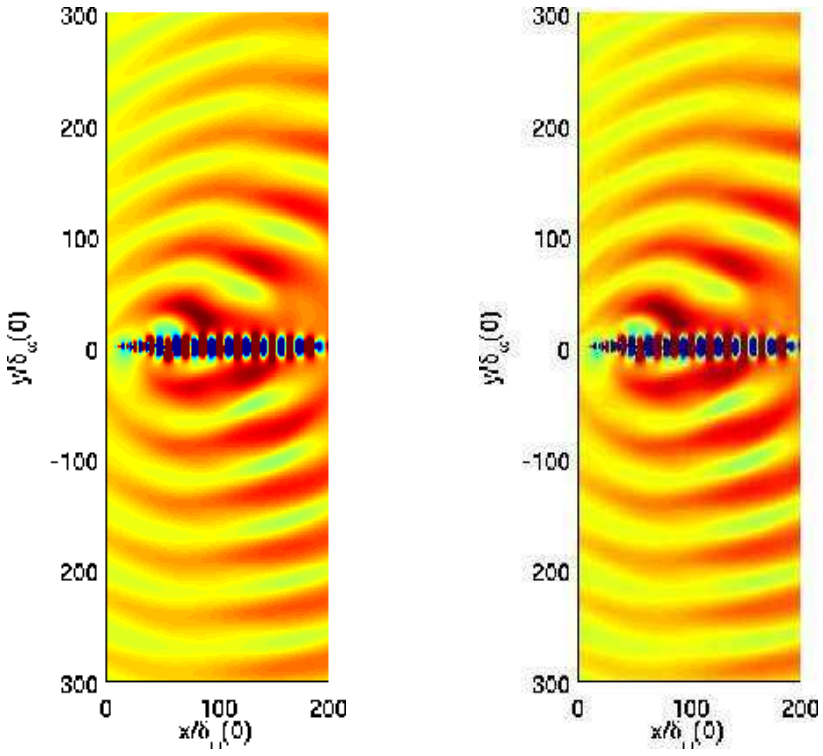

Figure 3.45: (a) Acoustic far field from DNS. (b) Acoustic far field from DMD. Pressure fluctuations are shown in the physical domain. Levels from -150 Pa to 150 Pa in both figures.

apparent source location: $(x, y) = (64\delta_\omega(0), 0)$. The direction and intensity of acoustic waves can be further illustrated by plotting the sound pressure levels (SPL). The r.m.s. values of the fluctuating pressure used in the SPL evaluation is advanced in time during one pairing period. By interpolating the values of p'_{rms} at the equidistant points on an arc of radius $110\delta_\omega(0)$ from the apparent source location $(x, y) = (64\delta_\omega(0), 0)$. From figure 3.46, the DMD reconstruction is in good agreement with the DNS both in term of magnitude and direction of the acoustic fronts in the two streams.

This acoustic behaviour is further explored by considering cross-sections of the pressure p' in the x domain. In figure 3.47, the streamwise evolution of the pressure is depicted in the far field, say $y = 110\delta_\omega(0)$. We see that the DMD computation predicts well the pressure radiated to the far field, while the predictions from nonlinear PSE calculation conducted by Cheung & Lele [26] in their study of acoustic radiation of compressible mixing layers diverged from their direct calculation by an order of magnitude. Similarly, cross-sections of the pressure in y domain at various streamwise stations are also plotted. Three positions are studied: at a point upstream of the vortex pairing location, the cross-stream pressure $p'(y)$ is shown in figure 3.48. The direct calculation and

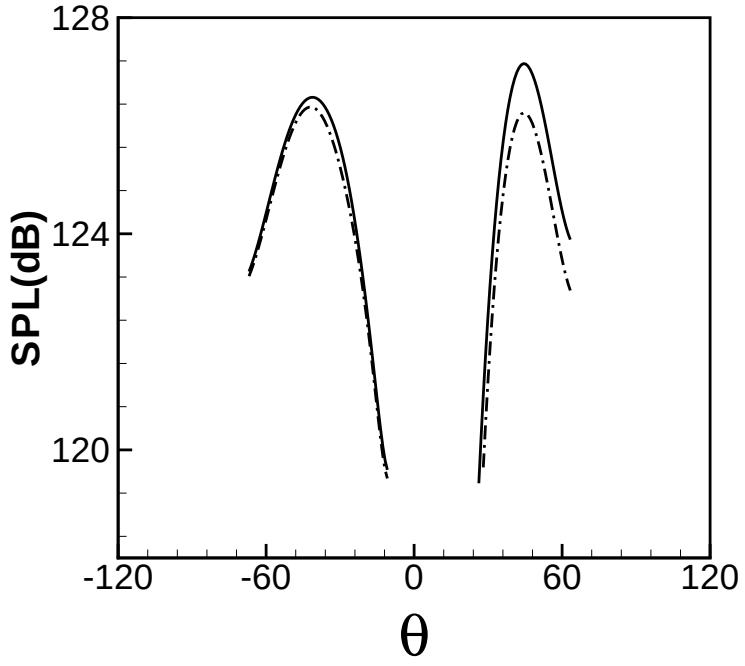

Figure 3.46: Far-field directivity for a radius at $110\delta_\omega(0)$ from the noise source located at $x = 64\delta_\omega(0)$ and $y = 0$ from DNS (solid line), from DMD (dashed line).

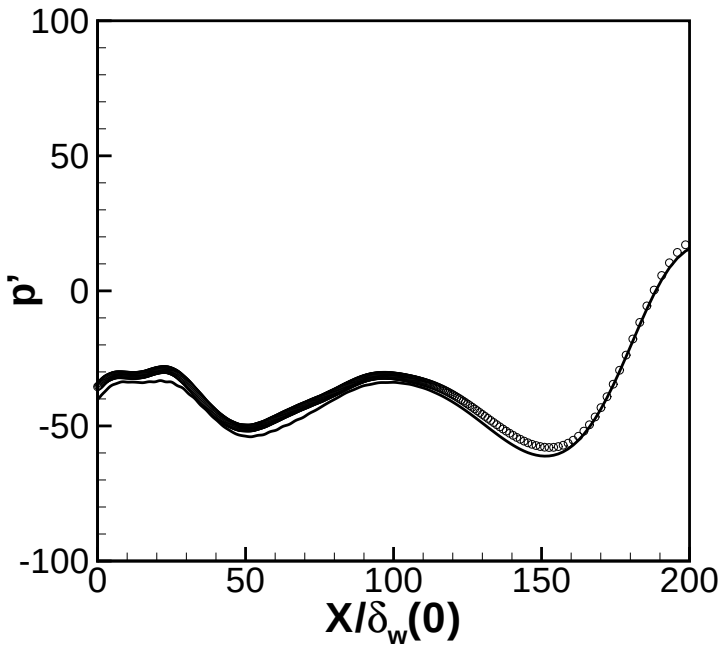

Figure 3.47: Streamwise evolution of the pressure perturbations $p'(x)$ at $y = 110\delta_\omega(0)$. Perturbations from DNS are shown in solid line, perturbations from DMD are depicted in circles.

DMD calculation both agree in the near field region ($|y| < 20$). Then, near the vortex pairing location, the cross-stream pressure $|p'(y)|$ is considered at $x = 64\delta_\omega(0)$ (figure 3.49). The far-field behaviour of the pressure agrees well between the two methods of calculation. At last, further downstream of the vortex pairing location, for instance at $x = 120\delta_\omega(0)$ in figure 3.50 the DMD projection and direct calculations of the far field coincide. Given the considerations of $p'(y)$ at these three representative locations, DMD method seems to capture well the acoustic behaviour of the mixing layer. Again, the pressure calculated by nonlinear PSE in Cheung & Lele [26] was reported approximately two orders of magnitude smaller than their direct calculations further downstream of the vortex pairing location. Finally, the temporal behaviour of pressure perturbations in the far-field region ($y = 110\delta_\omega(0)$) is plotted in figure 3.51. The pressure signal is seen to be fairly comparable to its directly computed counterpart.

3.3.3 Acoustic radiation from combined DMD-acoustic analogy

In the previous sections, the accuracy of the DMD analysis in predicting correctly the shear layer dynamics and the resulting acoustic radiation were assessed. In this section, inspired by the work of Kierkegaad *et al.* [62] in which they used a set of global modes as source data to obtain the far-field acoustic

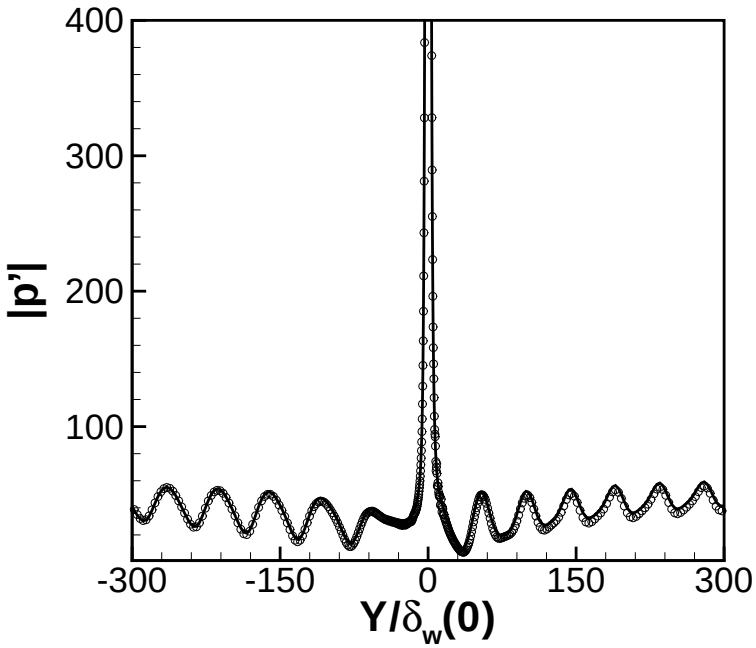

Figure 3.48: Cross-stream fluctuating pressure $|p'(y)|$ around the roll-up location: $x = 30\delta_\omega(0)$. Perturbations from DNS are shown in solid line, perturbations from DMD are depicted in circles.

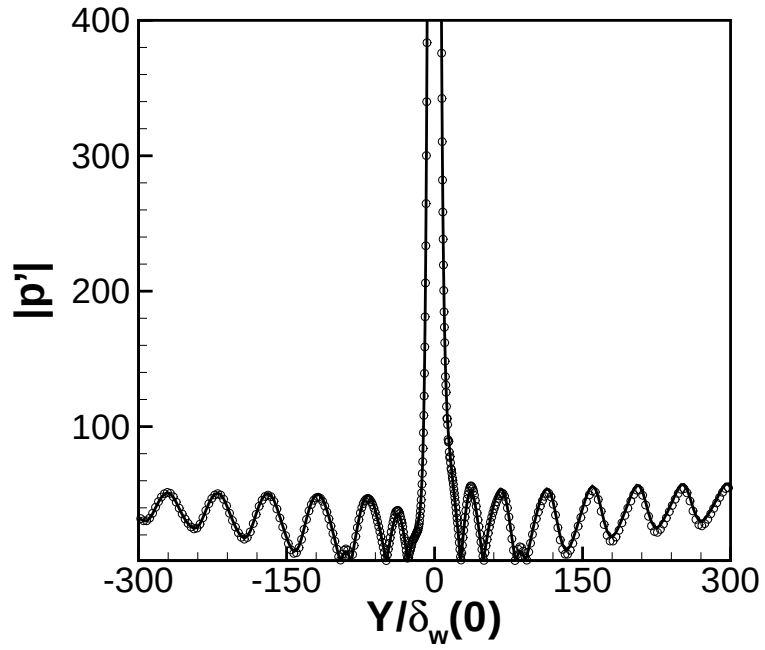

Figure 3.49: Cross-stream pressure $|p'(y)|$ at the vortex pairing location: $x = 64\delta_\omega(0)$. Perturbations from DNS are shown in solid lines, perturbation from DMD are depicted in circles.

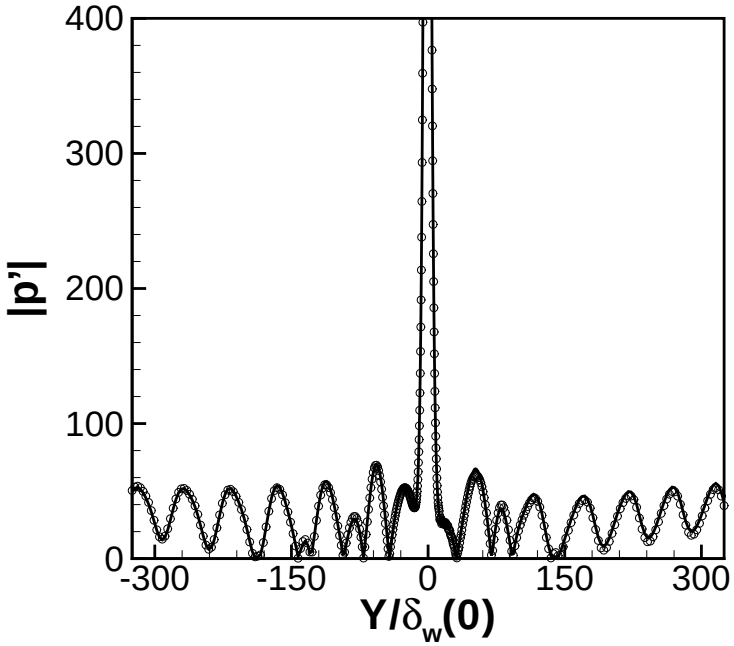

Figure 3.50: Cross-stream pressure $|p'(y)|$ at a point further downstream of the vortex pairing location: $x = 120\delta_\omega(0)$. Perturbations from DNS are shown in solid line, perturbations from DMD are depicted in circles.

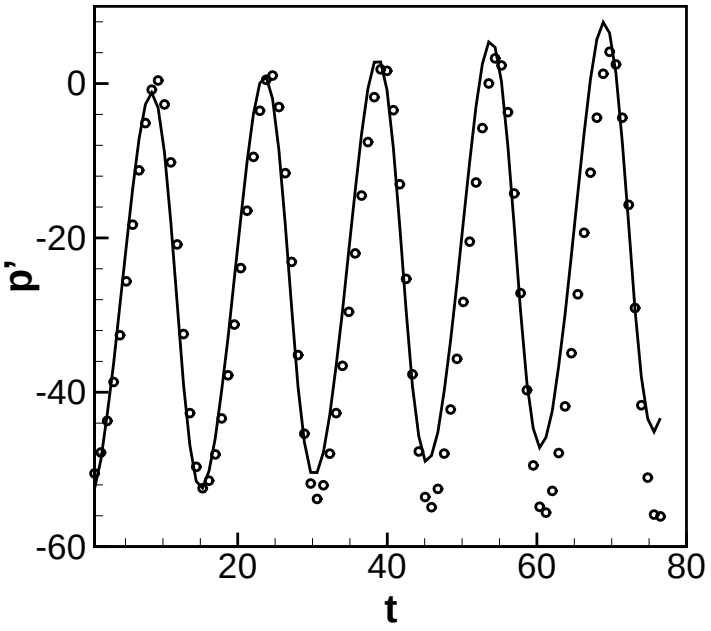

Figure 3.51: Temporal evolution of the pressure fluctuation $p'(t)$ taken at $x = 64\delta_\omega(0)$, $y = 110\delta_\omega(0)$. Perturbations from DNS are shown in solid line, perturbations from DMD is depicted in circles.

prediction, we will combine the DMD approach with an acoustic analogy, and properly capture the acoustic wave propagation. The acoustic field is obtained by solving an acoustic analogy with necessary source terms determined from the near-field data of the DMD analysis. First of all, we should verify the accuracy of the source terms information in the near-field. To this end, we perform a DMD analysis only inside the near-field subdomain. The subdomain used here is identical to that has been used for the acoustic analogy from DNS data in section 3.1. We proceed as the DMD analysis in the entire domain. 300 snapshots are saved in the subdomain. The choice of the inner product has been shown to have no effect on the computation. We thus adopt the incompressible inner product for simplicity. When varying the number of snapshots N from 100 to 300, dominant values of the angular frequencies are listed in Table 3.3. Peak frequencies are found to remain nearly the same with the increasing number of snapshots. Also, these frequencies peak at the rather similar locations compared to Table 3.2. The number 300 will be used hereafter. The eigenvalues as well as the energy spectra for $N = 300$ are then shown in figure 3.52 (a) and (b), respectively. These plots are very similar to those obtained from the DMD computation in the full domain. That is, four most energetic Koopman modes are identified as before: $f_0/2$, f_0, $3f_0/2$ and $2f_0$. These modes are then projected onto the initial DNS snapshot as (3.18). The projected modes are shown in figures 3.53, 3.54, 3.55 and 3.56. The spatial structures seem to follow those obtained from the DMD analysis performed in the entire domain by using the same levels. The spatial and temporal evolutions of the instability waves in the mixing layer are further examined by comparing the results from the DNS and the DMD computations. The first comparison in figure 3.57 depicts the reconstructed roll up and vortex pairing events during one pairing period. The results resemble closely those computed directly by the DNS, shown previously in figure 3.41. The second comparisons shown in figures 3.58 and 3.59 plot the streamwise and temporal evolutions of the fluctuating pressure inside the near-field region. Once again, both DMD and direct calculations agree in the spatial and temporal evolutions in the near-field subdomain. Given these comparisons, we see that in the near-field region of the flow, the coherent structures associated with Koopman modes are well predicted by the DMD analysis performed over only the near-field domain. We therefore attempt to capture the acoustic wave propagation generated by these structures in this so-called combined DMD-acoustic analogy approach. The acoustic grid resolution in the observation region is fixed as in the acoustic analogy from DNS. The source input data from the DMD computation is stored during one pairing period in the subdomain. The obtained acoustic radiation patterns is shown in figure 3.60 (b), and agree qualitatively with figure 3.60 (a) from the directly computed mixing layer. In addition, the vortex sound generation mechanism is well identified.

To further explore the acoustic behaviour, the far-field directivity is evaluted as determined by (3.2). In figure 3.61 the acoustic pressure in the far field is plotted against the angle between the observation point at a distance of $110\delta_\omega(0)$ from the apparent source origin. The directivity is strongly peaked near $\theta \approx 45^\circ$ and $\theta \approx -41^\circ$ in the high- and low-speed streams respectively. When compared to the equivalent directivity plots from the direct calculations, the agreement is satisfactory. We therefore conclude that the Koopman modes obtained from the DMD analysis in the subdomain describe well the instability waves responsible for the acoustic radiation, which have been validated by the

N	$f_0/2$	f_0	$3f_0/2$	$2f_0$
100	0.416	0.832	1.247	1.663
150	0.416	0.834	1.251	1.667
200	0.418	0.838	1.249	1.664
250	0.417	0.835	1.252	1.665
300	0.417	0.834	1.258	1.667

Table 3.3: Dominant values of angular frequency ω_r as the number of snapshots N is increased from 100 to 300 using the incompressible inner product.

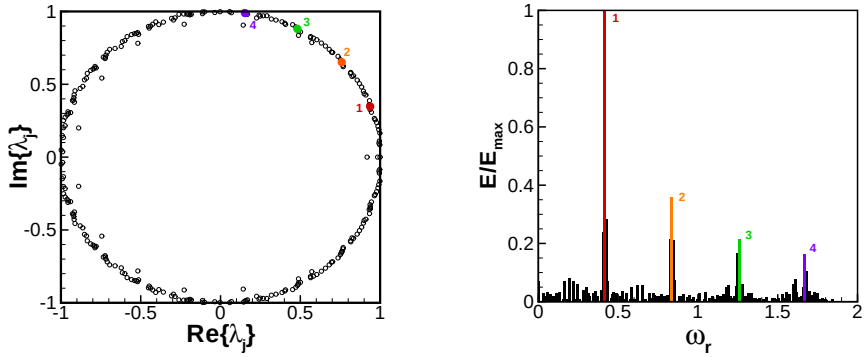

(a) (b)

Figure 3.52: DMD analysis performed over the near-field subdomain using 300 snaphots: (a) Ritz values λ_j. (b) Energy spectrum of the Koopman modes at each angular frequency ω_r. In both figures, the Ritz values associated with the most energetic modes are marked with 1, 2, 3 and 4, respectively.

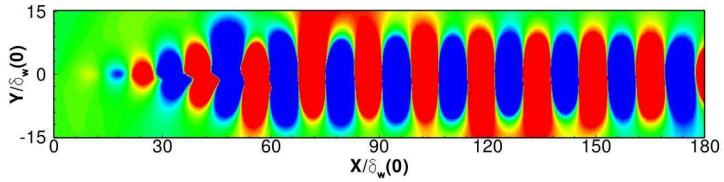

Figure 3.53: The Koopman mode at $f_0/2$ using the pressure fluctuations. Levels from -80 Pa to 80 Pa.

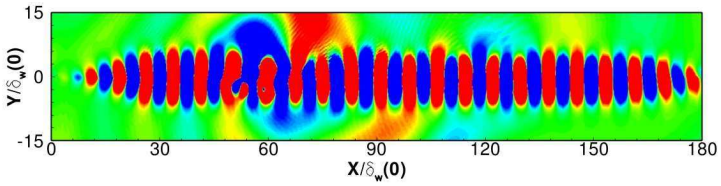

Figure 3.54: The Koopman mode at f_0 using the pressure fluctuations. Levels from -30 Pa to 30 Pa.

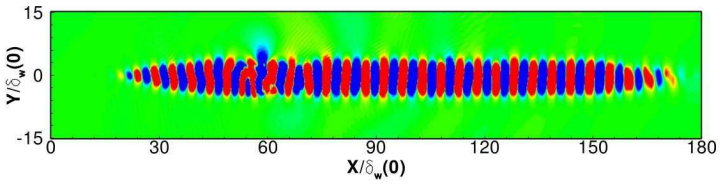

Figure 3.55: The Koopman mode at $3f_0/2$ using the pressure fluctuations. Levels from -20 Pa to 20 Pa.

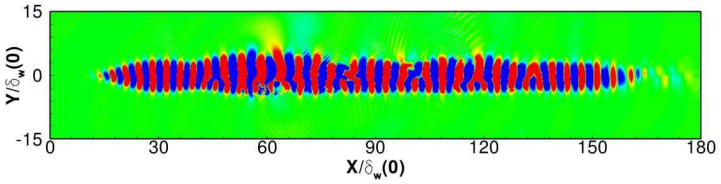

Figure 3.56: The Koopman mode at $2f_0$ using the pressure fluctuations. Levels from -5 Pa to 5 Pa.

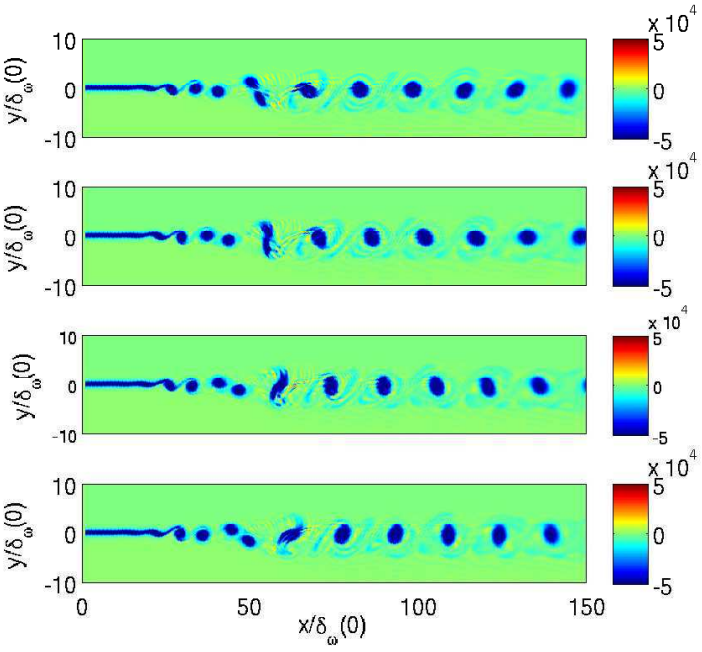

Figure 3.57: Follow-up of the vortex pairing in the near-field mixing region from DMD. Total spanwise vorticity is shown. Levels from -5×10^4 /s to 5×10^4 /s.

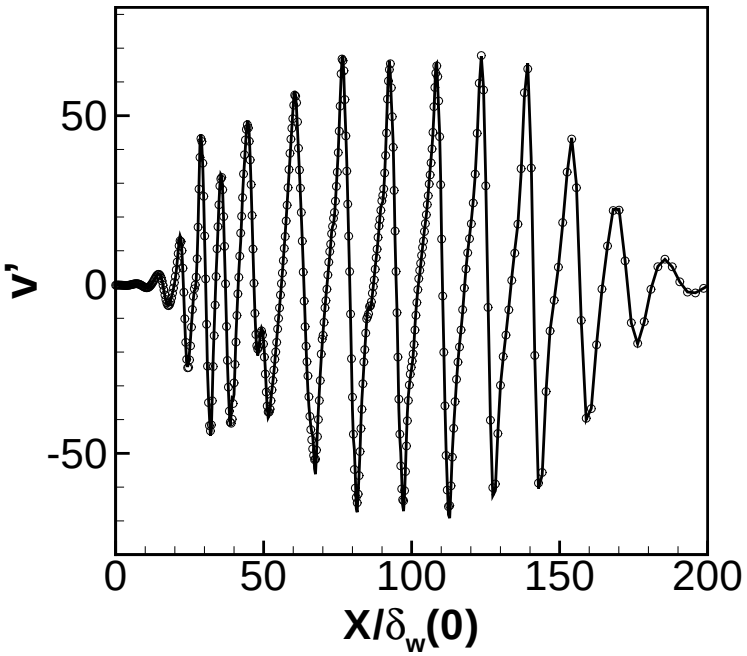

Figure 3.58: Streamwise development of the velocity perturbations $v'(x)$ along the centerline $y = 0$. Perturbations from DNS are shown in solid line, perturbations from DMD are depicted in circles.

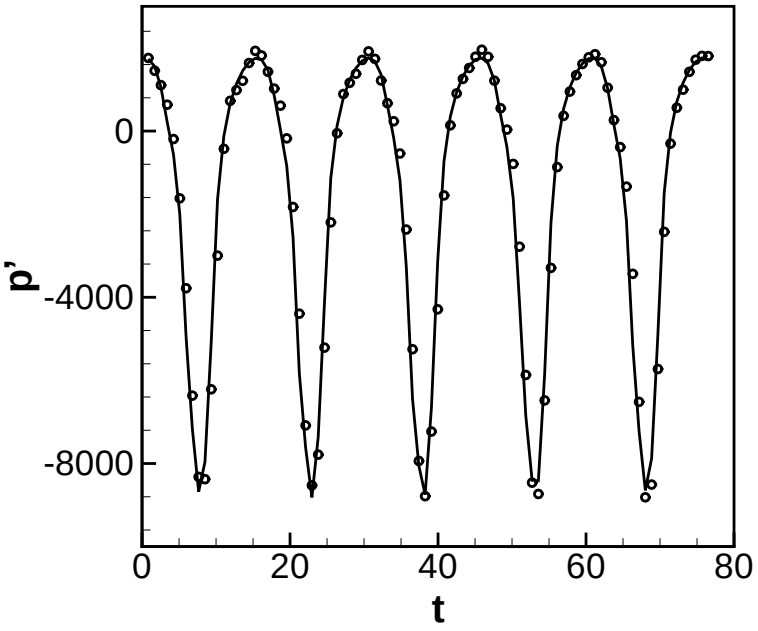

Figure 3.59: Temporal evolution of the pressure fluctuation $p'(t)$ taken at the center of the computational domain $(70\delta_\omega(0), 0)$. Perturbations from DNS are shown in solid line, perturbations from DMD are depicted in circles.

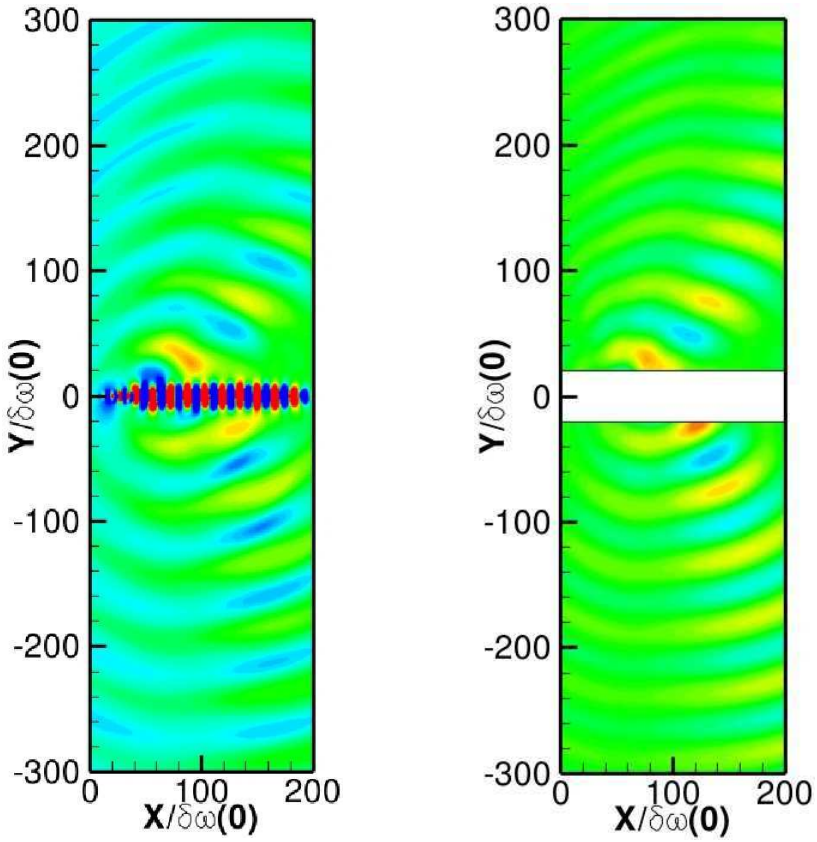

Figure 3.60: (a)Fluctuating pressure from DNS. (b) Far-field acoustic predictions. Real part of the pressure perturbation using the acoustic analogy. Levels from -100 Pa to 100 Pa in both figures.

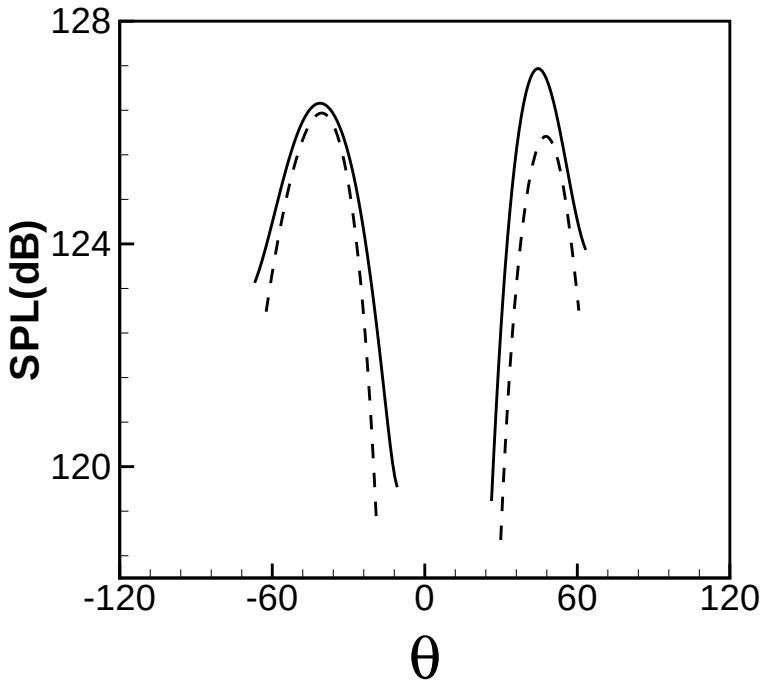

Figure 3.61: Far-field directivity for a radius at $110\delta_\omega(0)$ from the noise source located at $x = 64\delta_\omega(0)$ and $y = 0$ from DNS (solid line), using the acoustic analogy from DMD (dashed line).

acoustic analogy. The DMD method provides a relevant tool to capture the underlying flow dynamics. For the purpose of examining the radiated sound field and thus its link to the coherent structures in the near field, a DMD analysis within a spatial framework appears appropriate because of the spatial evolution of the linear acoustic wave propagation in the far field.

3.3.4 DMD analysis within a spatial framework

In this section, we are interested in the capability of the DMD method within the spatial framework based on the data gathered by DNS to capture the underlying flow dynamics. As noted in chapter 2, the snapshot sequence may be represented in space instead of in time. To better reveals acoustic characteristics of the mixing layer, such as the wavelength, the directivity, our investigation is performed over the polar coordinates (R, θ) rather than the Cartesian coordinates (x, y). The priviliged direction x is then the radial direction R of the propagating acoustic waves, the propagator is then $\mathcal{B}(\Delta R)$. The passage from the polar to Cartesian coordinates is achieved by applying a second-order spline interpolation. The center of the polar coordinates is chosen located near the apparent source location: $(64\delta_\omega(0), 0)$. In this way, the extraction of the snapshots are performed in $(\theta - t)$- plane between two consecutive raidal direc-

tion along R. The spatial DMD analysis proceed in the top and bottom parts of the computational domain. The extracted zones are shown in black line in figure 3.62. The zone in the top domain extends over $60 \leq R/\delta_\omega(0) \leq 240$, $35° \leq \theta \leq 70°$, and the zone extracted from the bottom domain extends over $60 \leq R/\delta_\omega(0) \leq 240$, $-100° \leq \theta \leq -15°$. Each of the extracted zones can cover essentially 3 wavelengths and the principal angles of the directivities. In both computations, a regular distance of $\Delta R = 1.818$ between two consecutive snapshots is considered. The spatial spectra resulting from the top and bottom domains are displayed in figure 3.63, in which the spatial growth rates σ of the acoustic waves are plotted versus the wavenumber α_R. For both cases, all of the Koopman modes are seen to attenuate spatially, and the least damped modes in the two domains are indicated with a vertical dashed line in the spectra. The wavenumber associated with these modes is $\alpha_R = 0.1$, and their wavelength is given by $\lambda = 2\pi/\alpha_R = 2\pi/0.1 = 60$. This wavelength seems to be close to that of the principal emerging propagating acoustic waves, shown in figure 3.62. The corresponding Koopman modes are shown in figures 3.64 (a) and 3.65 (a) by plotting the density perturbations in $(\theta - t)$- plane. The spatio-temporal evolutions of acoustic fluctuations in the far field are thus clearly illustrated. One may observe that the slope of these perturbations is non zero but constant along the time, which gives an angular velocity of the acoustic perturbations for a given wavenumber α_R: $d\theta/dt$. This is due to convection effects of the acoustic waves and refraction effects by the velocity gradient in the near-field shear layer. Similar behaviour is observed in the bottom part with the opposite sign of the angular velocity. Furthermore, the dominant frequencies of the acoustic waves are obtained by Fourier transforming the density fluctuations ρ' in time. Figures 3.64 (b) and 3.65 (b) show that both values peak near $\omega_r \approx 0.41$ which corresponds to the frequency of $f_0/2$. The directivity of the maximum magnitude of the acoustic waves peaks around $\theta \approx 50°$. This may be attributed to the main direction of the acoustic waves propagation in a global viewpoint, that is to say, inside the focused zones shown in figure 3.62. From a local point of view, the spatio-temporal evolution of the acoustic perturbations is illustrated by considering three different radial locations: $R/\delta_\omega(0) = 60$, $R/\delta_\omega(0) = 150$ and $R/\delta_\omega(0) = 240$ inside the bottom domain, as shown in figure 3.66 (a), (b) and (c), respectively. We may observe that the velocity of the propagation remains nearly the same and the directivity of acoustic waves varies with the considered location. In either case, this represention in space and time gives us a general information about the main direction of acoustic waves, then this is in qualitative agreement with the directivities previously evaluated at the pairing location and a certain distance from this source obtained from DNS and DMD computations. The relationship between the spatial structures in the far field and in the near-field is then established. Through the above DMD analyses in two distinct approaches, the dynamics of the mixing layer has been well described by the extracted Koopman modes. A fraction of the flow dynamics captured in the near field is sufficient for the entire flow reconstruction.

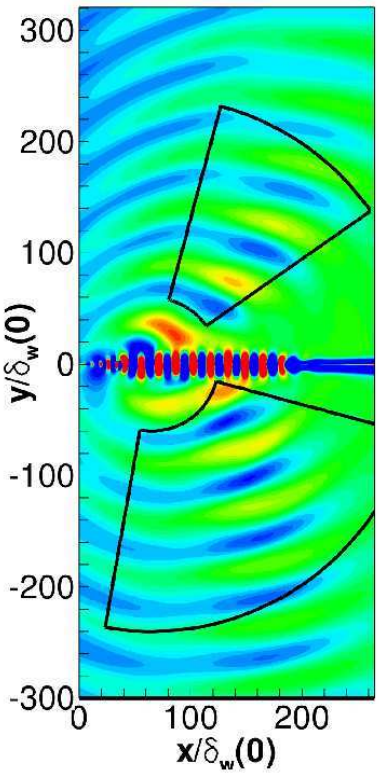

Figure 3.62: Extracted zones used in the spatial DMD analysis are shown in black lines.

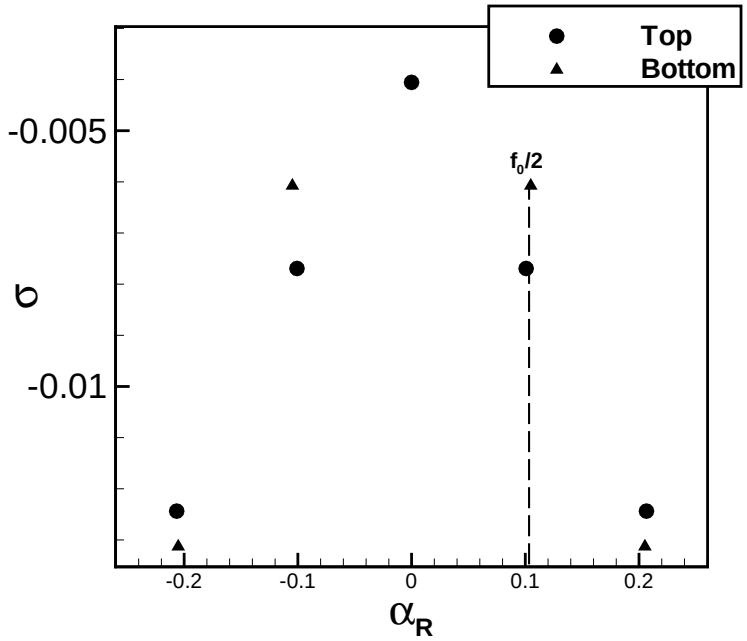

Figure 3.63: Spatial spectra from the spatial DMD analysis performed in top and bottom domain are shown in filled circles and triangles. The spatial growth rate σ is plotted versus the wavenumber α_R. The modes with the wavenumber $\alpha_R \approx 0.1$ correspond to the mode $f_0/2$ (dashed line).

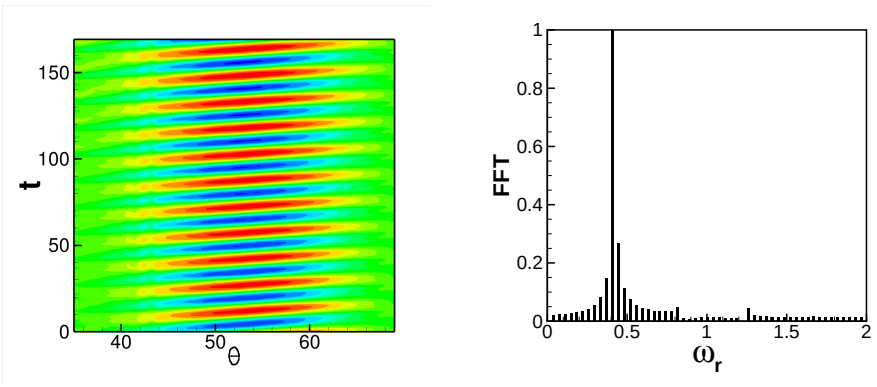

(a) (b)

Figure 3.64: (a) Spatial DMD analysis performed in the top domain: the dominant frequency is $f_0/2$, we associate this spatial structure with $f_0/2$. Density perturbations are plotted as a function of the angle θ and time t. (b) The dominant frequency detaches near $f_0/2$ through the Fourier transformed density fluctuations in time.

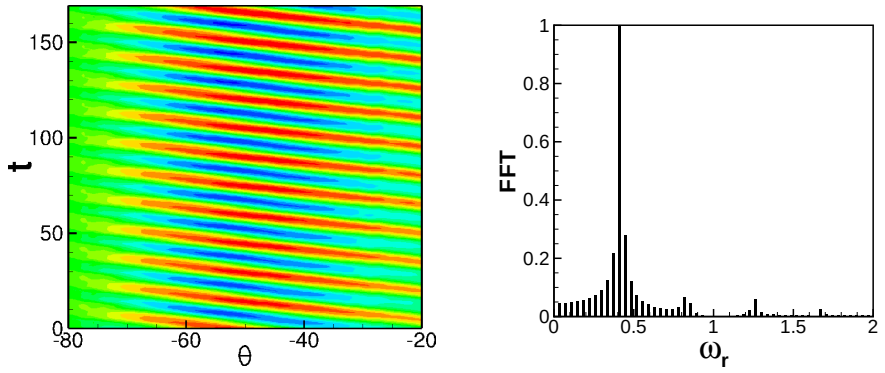

(a) (b)

Figure 3.65: (a) Spatial DMD analysis performed in the bottom domain: the dominant frequency is $f_0/2$, we associate this spatial structure with $f_0/2$. Density perturbations are plotted as a function of the angle θ and time t. (b) The dominant frequency detaches near $f_0/2$ through the Fourier transformed density fluctuations in time.

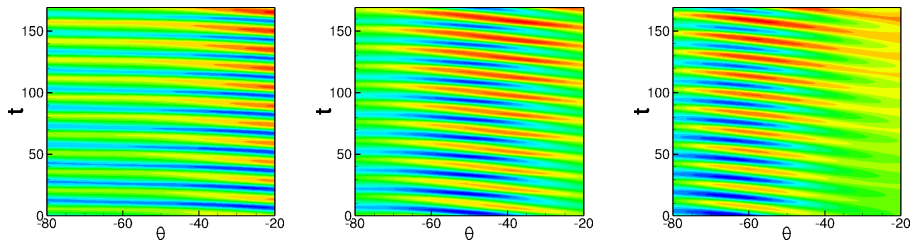

(a) (b) (c)

Figure 3.66: Space-time evolution of the acoustic perturbations considered at (a) $R/\delta_\omega(0) = 60$; (b) $R/\delta_\omega(0) = 150$; (c) $R/\delta_\omega(0) = 240$ in the bottom domain.

Chapter 4

Double vortex pairings

In the previous chapter, the noise produced by only one single vortex pairing in the mixing layer has been investigated. We indicated that the nonlinear DMD analysis could accurately predict both the near-field hydrodynamic behaviour and the far-field acoustic radiation in the temporal and spatial approach. It is worth noting that the shear layer dynamics is predominantly very complex because of its strong dependence of the external noise. In this chapter we wish to obtain a more complex flow configuration. Following Colonius, Lele & Moin [30], we can obtain double vortex pairings by exciting the mixing layer with a combination of 4 frequencies. The results from the DNS will be first presented. Then, a fully nonlinear DMD analysis within both a temporal and spatial framework will be accomplished. We will see if the DMD method is an appropriate tool for the prediction of the underlying flow dynamics in a more complex situation.

4.1 Direct computation

The flow parameters for this computation remain the same as in the one single pairing case: the convective Mach number remains $M_c = 0.176$. Inspired by the work of Colonius, Lele & Moin [30], the simulation is designed such that four modes of the mixing layer could be simultaniously excited, that is, the fundamental frequency f_0 and its three subharmonics: $f_0/2$, $f_0/4$ and $f_0/8$. The excitation is achieved by introducing the following perturbations on the streamwise and cross-stream velocity components at every time-step:

$$\begin{cases} u'(x,y) = \dfrac{(y-y_0)}{\Delta y_0} U_c f(t) \exp\left[-\ln 2 \dfrac{(x-x_0)^2+(y-y_0)^2}{{\Delta y_0}^2}\right] \\ \\ v'(x,y) = -\dfrac{(x-x_0)}{\Delta y_0} U_c f(t) \exp\left[-\ln 2 \dfrac{(x-x_0)^2+(y-y_0)^2}{{\Delta y_0}^2}\right] \end{cases} \tag{4.1}$$

where $(x_0, y_0) = (1.5\delta_\omega(0), 0)$ corresponds to the forcing location $i = 6$, and $\omega_0 = 2\pi f_0$ is the angular frequency of the fundamental mode. The half-width of the Gaussian function is $\Delta y_0 = 3\Delta y_{min}$, and the combination of the frequencies $f(t)$ is applied as follows

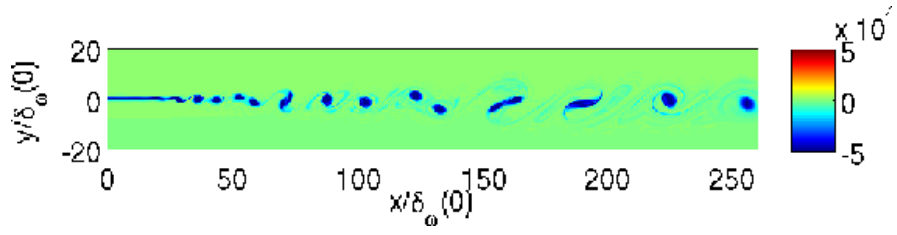

Figure 4.1: Vorticity field in the near-field sheared region. Levels: min: -5×10^4 /s, max: 5×10^4 /s.

$$f(t) = \left[\alpha_1 \sin(\omega_0 t) + \alpha_2 \sin(\frac{\omega_0}{2}t + \beta_1) + \alpha_3 \sin(\frac{\omega_0}{4}t + \beta_2) + \alpha_4 \sin(\frac{\omega_0}{8}t + \beta_3)\right]$$

Based on our empirical tests, the amplitudes of these four frequencies and the phase shifts of the subharmonics relative to the phase of the fundamental have been ajusted such as to obtain two different vortex pairings. The amplitudes are $\alpha_1 = 2\times10^{-4}$, $\alpha_2 = 10^{-4}$, $\alpha_3 = 5\times10^{-5}$ and $\alpha_4 = 2.5\times10^{-5}$, respectively, and the phase differences are: $\beta_1 = \pi/2$, $\beta_2 = \pi$ and $\beta_3 = 3\pi/2$ for $f_0/2$, $f_0/4$ and $f_0/8$, respectively. The computational domain should be long enough to take into account additional second pairings further downstream. It extends to $x/\delta_\omega(0) = 250$ in the streamwise direction resolved with 801 grid points, not including the sponge zone. An instantaneous vorticity field after the saturated regime in the mixing near-field region is shown in figure 4.1. Not only the roll up and the first fixed vortex pairings are exhibited, three subsequent pairs of larger vortices are also present further downstream. Figure 4.2 shows the resulting radiated sound by plotting the fluctuating pressure in the far field. Even though acoustic patterns appear less clear compared to the single pairing case, we can tell however the primary mechanism of sound generation remains the vortex pairings. An interference of acoustic waves seems to appear because of the different sound sources in the shear layer.

4.2 Nonlinear model: DMD analysis

For this double vortex pairing case, we perform directly a DMD analysis in a nonlinear approach. Both temporal and spatial analyses will be considered to extract the underlying dynamic information from the flow field.

4.2.1 DMD analysis within a temporal framework: coherent structures extraction

300 snapshots of instantaneous density, velocity and pressure fluctuations at a sampling rate $\Delta t = 1.36\times10^{-5}$ s are recorded during the direct simulation after the saturated regime. As noted earlier, the choice of the norm has negligible impact on the results of computation because of the low Mach number of the underlying flow. In practice, we use the norm based on the standard

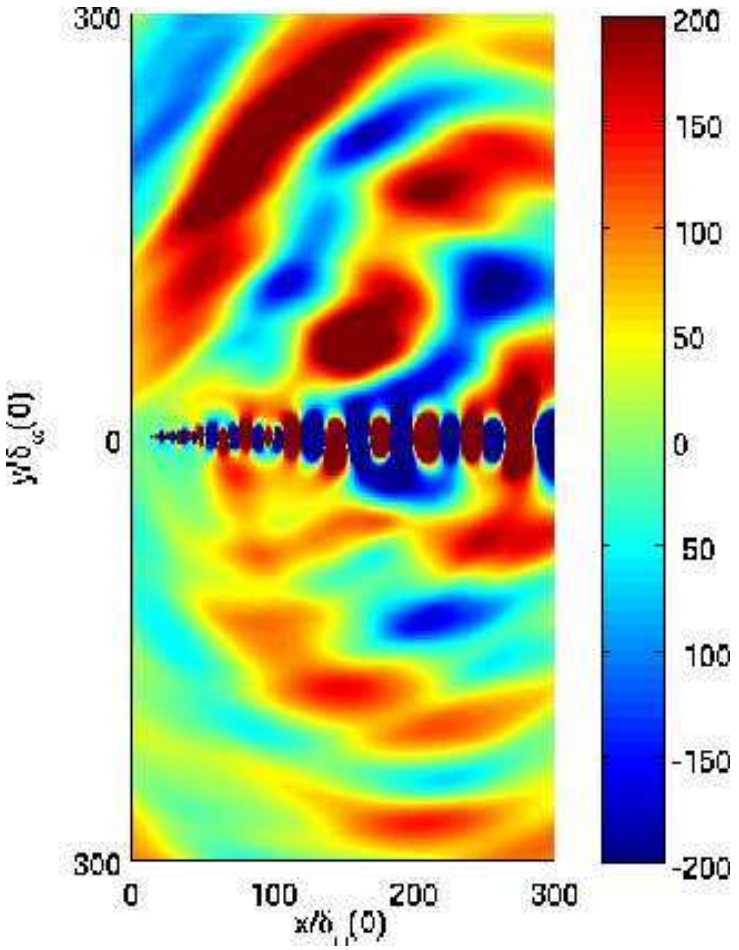

Figure 4.2: Far-field fluctuating pressure from the DNS calculation. Levels from −300 to 300 Pa.

N	$f_0/4$	$f_0/2$	f_0	$3f_0/4$	$3f_0/8$	$f_0/8$
100	0.207	0.415	0.622	0.828	0.308	0.115
150	0.207	0.415	0.624	0.830	0.308	0.110
200	0.207	0.414	0.623	0.830	0.309	0.110
250	0.207	0.415	0.622	0.828	0.308	0.110
300	0.206	0.415	0.622	0.830	0.309	0.109

Table 4.1: Dominant values of angular frequency ω_r as the number of snapshots N is increased from 100 to 300 using the incompressible inner product.

incompressible inner product. To examine the eventual influence of the number of snapshots N in the input data sequence, 5 cases are carried out as N is increased from 100 to 300. Dominant values of angular frequencies are noted down in Table 4.1. We see that with the increasing N, these peak values are found to remain the same approximately. Thus, we will use a maximum of 300 snapshots in the following computation. The eigenvalues for $N = 300$ and the extracted Koopman modes are depicted in figures 4.3. Figure 4.3 (a) shows that the saturated regime is reached because nearly all the Ritz values are found to lie on the unit circle $|\lambda_j| = 1$. From figure 4.3 (b), the eigenmode energy plot calculated from (3.3) provides the four dominant modes containing the maximum energies: $f_0/2$, $f_0/4$, f_0, $3f_0/4$, $3f_0/8$, $f_0/8$ marked 1, 2, 3, 4, 5 and 6, respectively. Note that only the positive parts of eigenvalues are shown owing to their complex conjugate pair character. Since three forcing frequencies $f_0/2$, $f_0/4$, $f_0/8$ are present, more nonlinear combination between the modes are possible. Here, nonlinear interactions of $f_0/8$ and $f_0/2$ results in $5f_0/8$, also $f_0/4$ and $f_0/8$ results in $3f_0/8$, and so forth. Through the projection of these modes onto the initial DNS snapshot as (3.18), we show the Koopman modes in both the entire and near-field domains in figures 4.4, 4.5, 4.6, 4.7, 4.8 and 4.9, respectively. All modes are seen to participate to the far-field acoustic radiation more or less. Nevertheless, the modes $f_0/4$ and $f_0/2$ contribute more to the sound field than $3f_0/4$ and f_0.

The evolutions of different instability waves in the mixing layer can be examined by measuring the energies for the eigenmodes f_0, $f_0/2$ and $f_0/4$. The energy of the eigenmode is computed as in (3.3) and plotted as a function of streamwise distance, shown in figure 4.10. All these modes go through an initial exponential growth stage, then they saturate near $x = 30\delta_\omega(0)$, $67\delta_\omega(0)$, and $144\delta_\omega(0)$, for f_0, $f_0/2$ and $f_0/4$ respectively. It seems that the roll up takes place when the fundamental f_0 reaches its saturation position, and the acoustic waves at the first two subharmonic frequencies $f_0/2$ and $f_0/4$ emanate from the regions where the pairings occur. This is similar to the observations of Laufer & Yen [63] and Bridges & Hussain [22]. The streamwise evolutions of these waves illustrate as well their spatial behaviours in the shear layer, shown in figures 4.13, 4.11 and 4.12 by plotting the pressure fluctuations as a function of x. Their spatial behaviours match closely the eigenmode energy plots. Through the above discussions, the DMD analysis has been proven to predict correctly both the hydrodynamics and aeroacoustics of the shear layer. In the next section, the mixing layer dynamics will be attempted to be recovered from the DMD analysis.

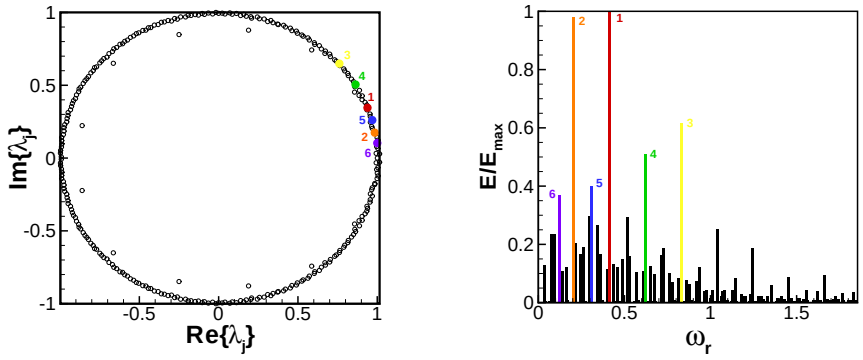

(a) (b)

Figure 4.3: DMD analysis performed over the entire computational domain using 300 snaphots: (a) Ritz values λ_j. (b) Energy spectrum of the Koopman modes at each angular frequency ω_r. In both figures, the Ritz values associated with the most energetic modes are marked with 1, 2, 3, 4, 5 and 6, respectively.

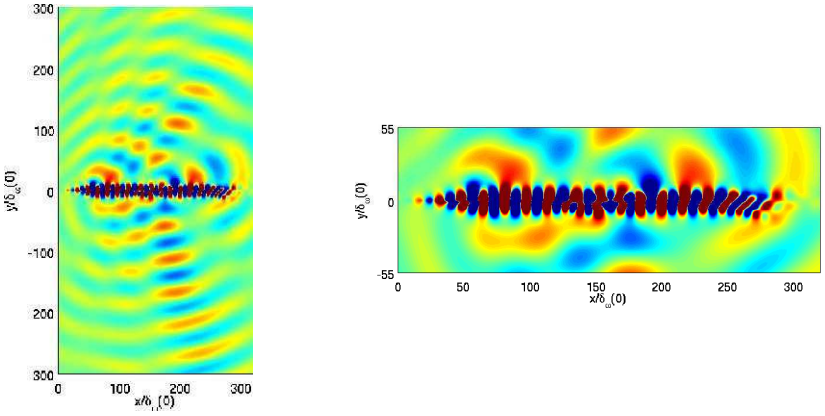

(a) (b)

Figure 4.4: (a) Real part of the pressure fluctuations for Koopman mode at $f_0/2$. (b) A zoom in of this mode inside the near-field region. Levels from -50 Pa to 50 Pa.

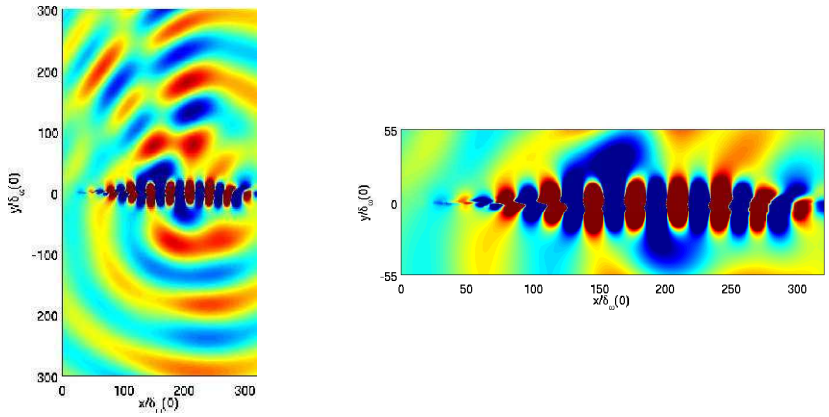

(a) (b)

Figure 4.5: (a) Real part of the pressure fluctuations for Koopman mode at $f_0/4$. (b) A zoom in of this mode inside the near-field region. Levels from -50 Pa to 50 Pa.

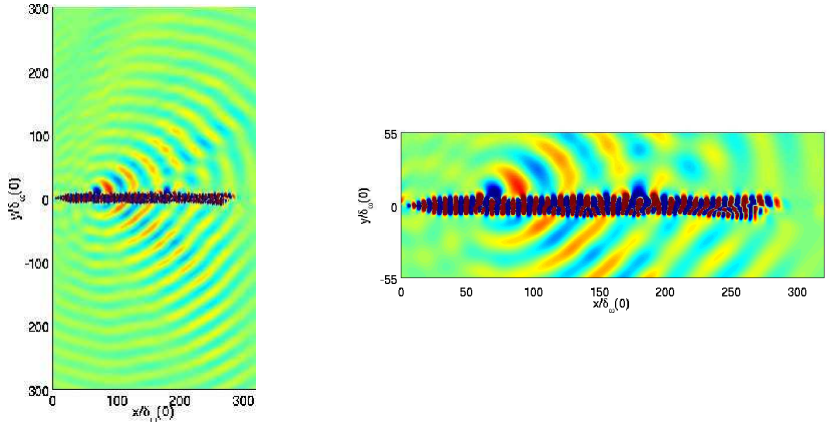

(a) (b)

Figure 4.6: (a) Real part of the pressure fluctuations for Koopman mode at f_0. (b) A zoom in of this mode inside the near-field region. Levels from -10 Pa to 10 Pa.

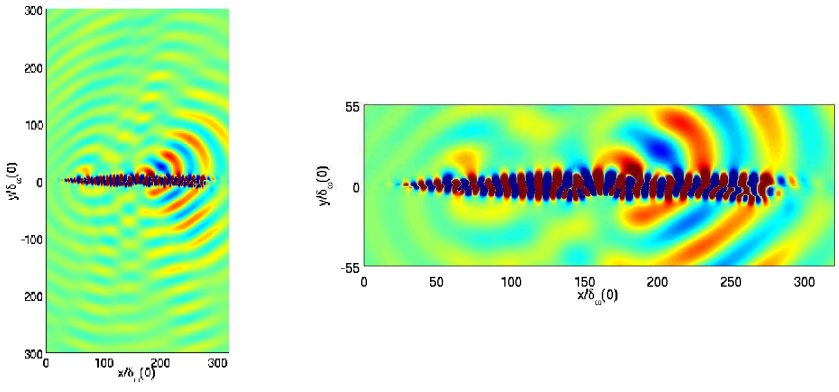

(a) (b)

Figure 4.7: (a) Real part of the pressure fluctuations for Koopman mode at $3f_0/4$. (b) A zoom in of this mode inside the near-field region. Levels from -10 Pa to 10 Pa.

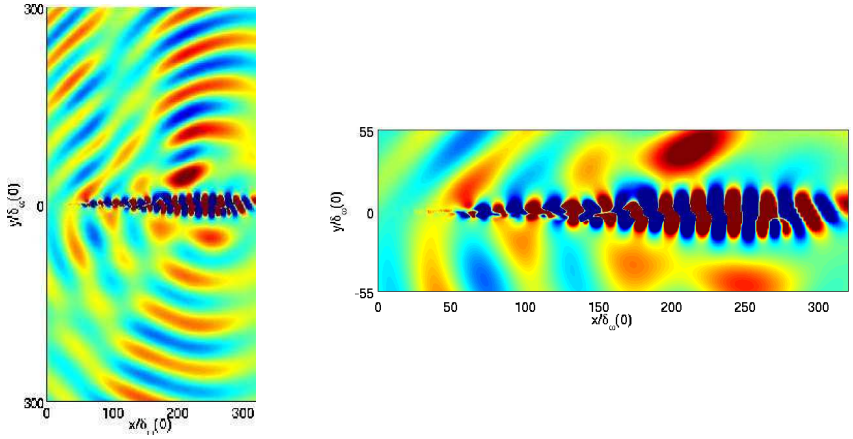

(a) (b)

Figure 4.8: (a) Real part of the pressure fluctuations for Koopman mode at $3f_0/8$. (b) A zoom in of this mode inside the near-field region. Levels from -10 Pa to 10 Pa.

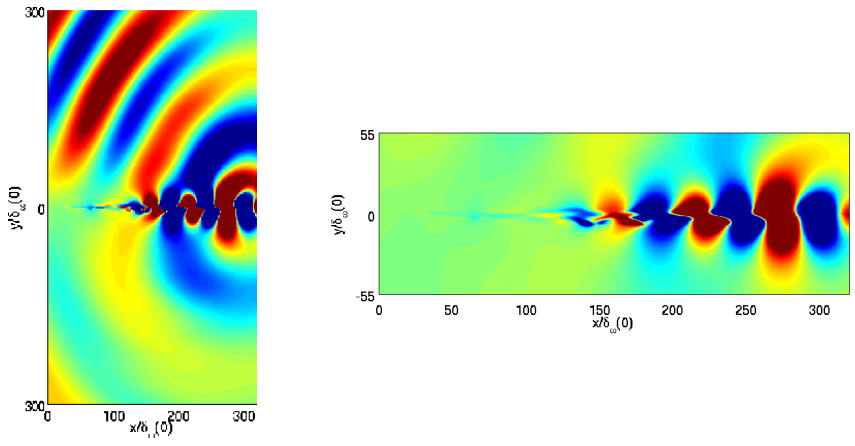

(a) (b)

Figure 4.9: (a)Real part of the pressure fluctuations for Koopman mode at $f_0/8$. (b) A zoom in of this mode inside the near-field region. Levels from -10 Pa to 10 Pa..

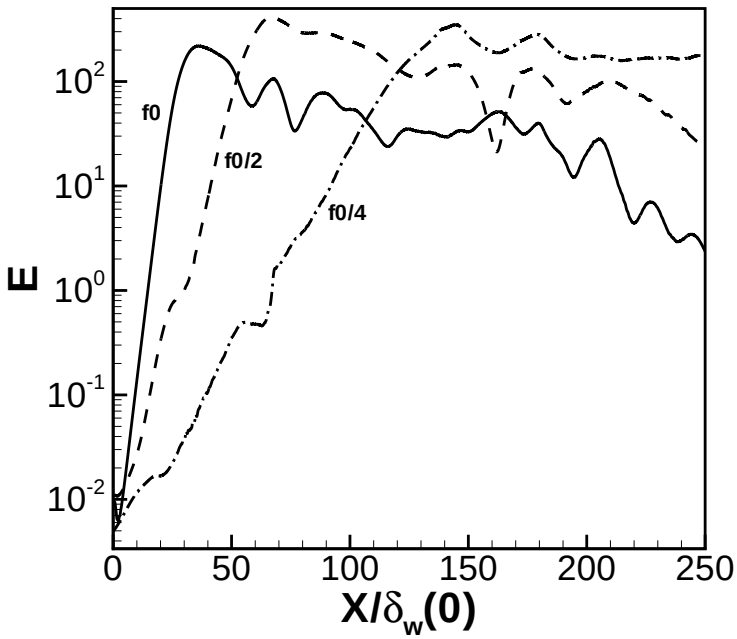

Figure 4.10: Streamwise evolution of energies E of the dominant modes at f_0, $f_0/2$ and $f_0/4$. Integrated modal kinetic energy for the fundamental mode f_0: solid line, the first subharmonic mode $f_0/2$: dashed line, the second subharmonic mode $f_0/4$: dashed-dotted line.

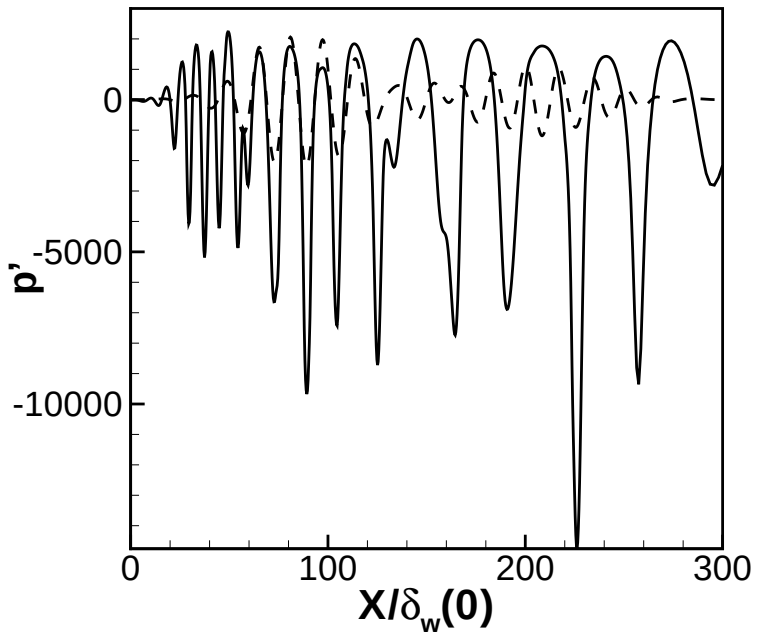

Figure 4.11: Streamwise evolution of the fluctuating pressure $p'(x)$ at $f_0/2$ along the centerline $y = 0$. Perturbations from DNS are shown in solid line, perturbations from DMD are depicted in dashed line.

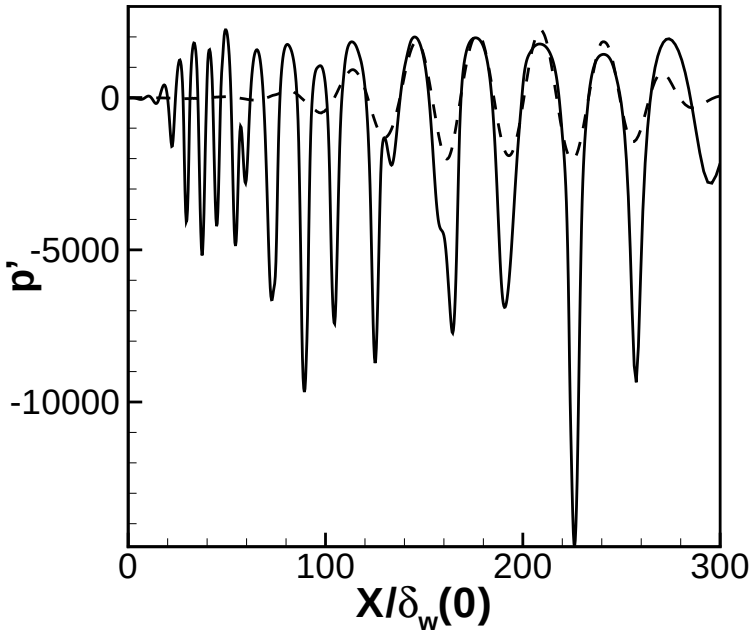

Figure 4.12: Streamwise evolution of the fluctuating pressure $p'(x)$ at $f_0/4$ at $y = 0$. Perturbations from DNS are shown in solid line, perturbations from DMD are depicted in dashed line.

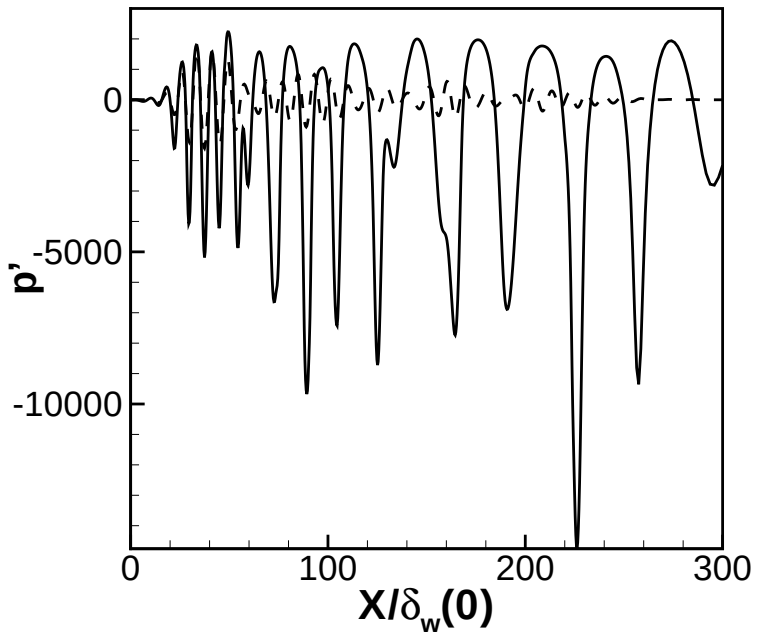

Figure 4.13: Streamwise evolution of the fluctuating pressure $p'(x)$ at f_0 at $y = 0$. Perturbations from DNS are shown in solid line, perturbations from DMD are depicted in dashed line.

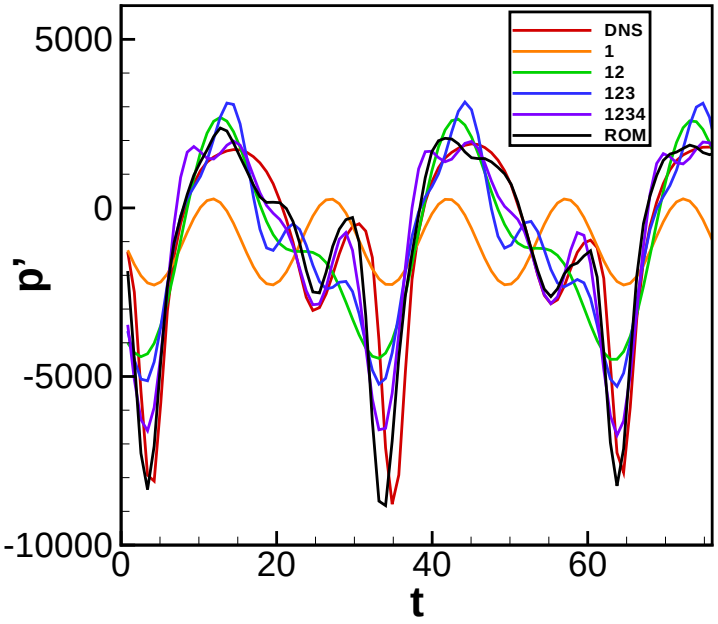

Figure 4.14: Time history of the pressure fluctuations $p'(t)$ along the the centerline $y = 0$. In red, from DNS calculation; in orange, mode 1; in green, mode 1 and 2; in blue, mode 1, 2 and 3; in violet, mode 1,2, 3 and 4; in black, with 80 modes.

4.2.2 Reconstruction of the flow dynamics through the DMD analysis

As mentioned in the single vortex pairing case previously, we perform an orthogonal projection onto the basis of Koopman modes to rebuild the entire flow field. Modes are added continually in the projection procedure. The projection performance can be illustrated by the temporal behaviour of the fluctuating quantities. For example, we show the projected pressure perturbations evolution during 3 periods of $f_0/4$ in figure 4.14. Compared to the computed pressure from DNS, the recovery of the flow dynamics can be achieved with nearly 80 modes. To further explore the influence of the number of modes m on this performance, an estimate of the residual r defined in (3.19) is realized. Residuals r with the respect to u' and p' are plotted in figures 4.15 and 4.16, respectively. We observe that r decrease in both plots as the number of modes m involved in the projection is increased. Up to 80 modes, the residual with respect to the streamwise velocity perturbations u' can pretty much reach 10^{-3}, and with respect to pressure fluctuations p' can achieve basically 10^{-1}. Therefore, 80 modes will be used in the next.

First, we wish to recover the aerodynamic motions of the mixing layer. For that purpose, the vortex pairing mechanism inside the near field is an important

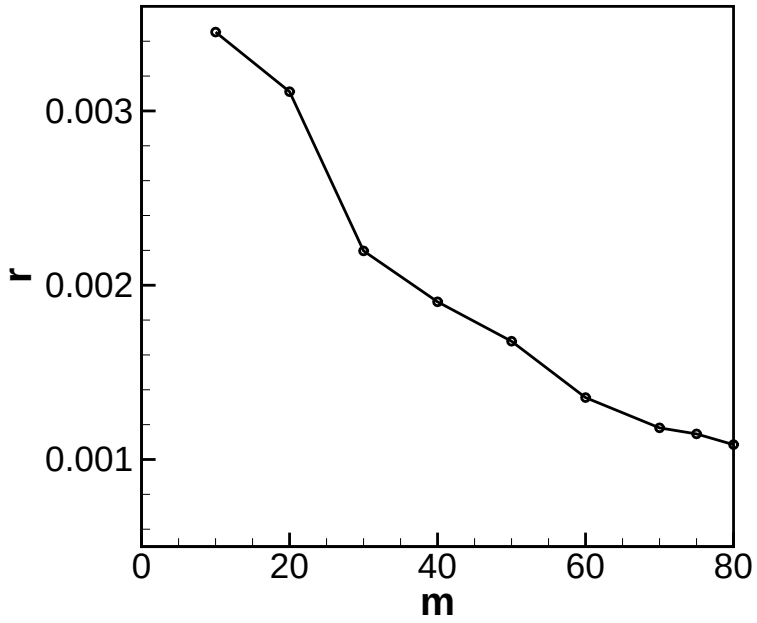

Figure 4.15: Residual history of the streamwise velocity fluctuations u' as a function of number of Koopman modes m used in the projection.

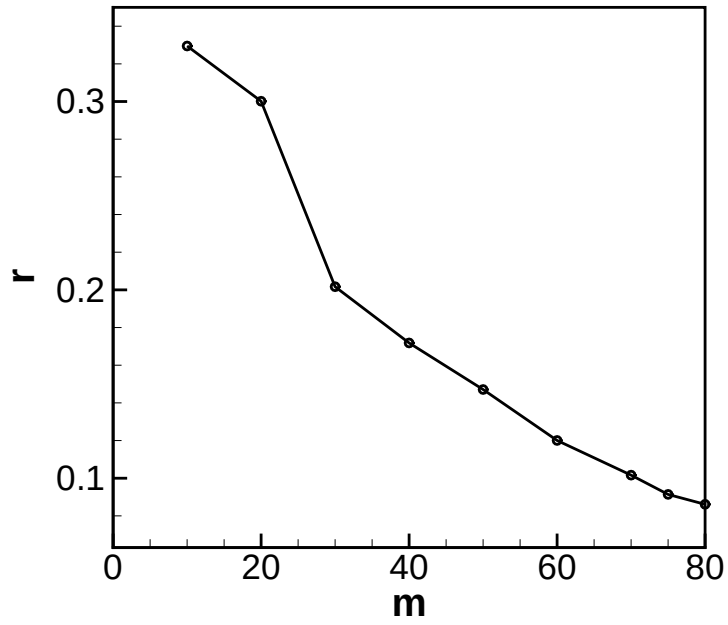

Figure 4.16: Residual history of the pressure fluctuations p' as a function of number of Koopman modes m used in the projection.

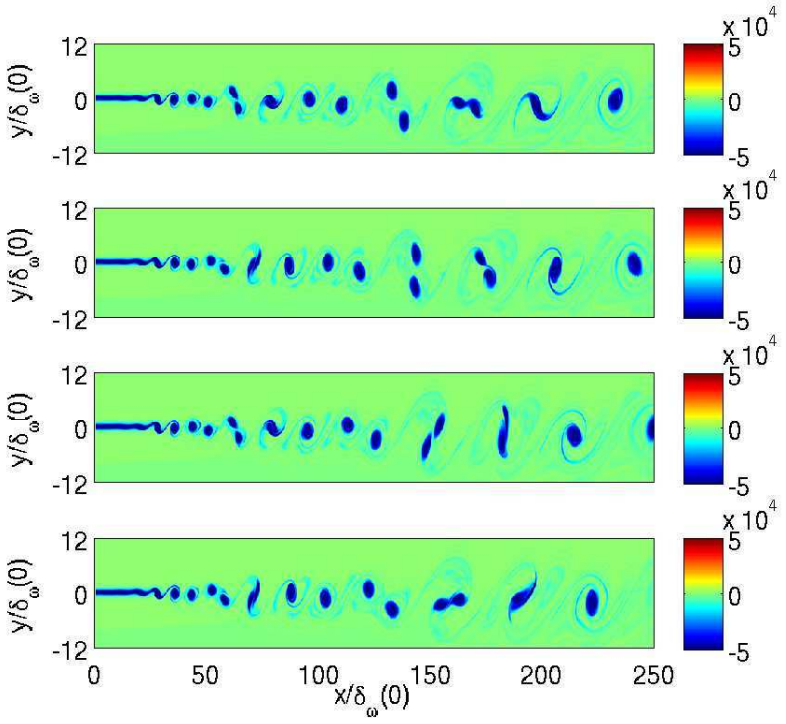

Figure 4.17: Follow-up of the vortex pairing at successive equidistant instants over one period of $f_0/4$ in the near-field mixing region from DNS. Total spanwise vorticity is shown. Levels from -5×10^4 /s to 5×10^4 /s.

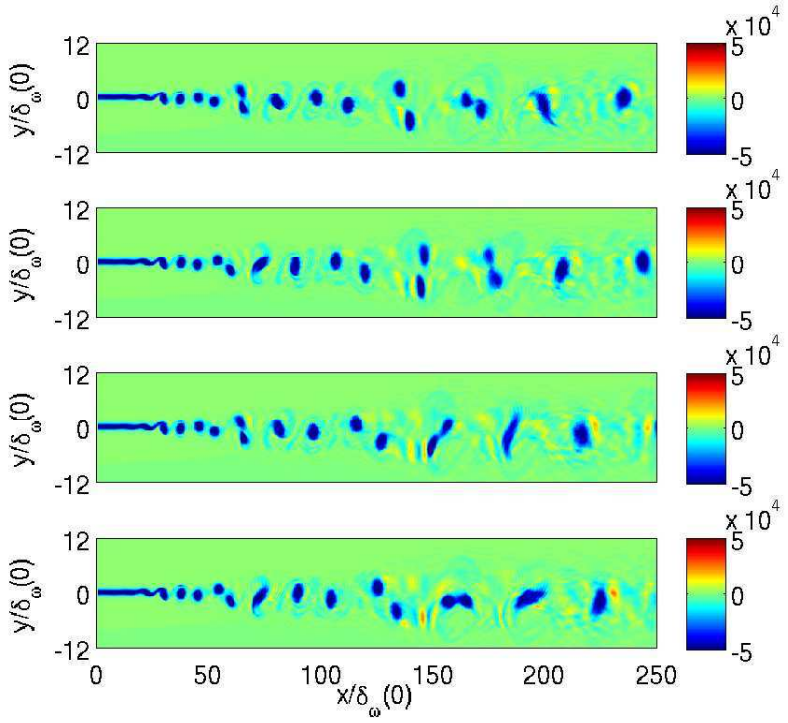

Figure 4.18: Follow-up of the vortex pairing at successive equidistant instants over one period of $f_0/4$ in the near-field mixing region from DMD. Total spanwise vorticity is shown. Levels from -5×10^4 /s to 5×10^4 /s.

point to consider. By fixing exactly the same time period as in DNS, that is, the period corresponds to the second pairing $f_0/4$, the reconstructed total spanwise vorticity field at four successive equidistant instants during this period from the DMD analysis is shown in figure 4.18. When compared to its directly computed counterpart, depicted in figure 4.17, both the roll-up and two vortex pairing events are captured quite satisfactorily by the present temporal DMD analysis. This hydrodynamic behaviour can be further examined by considering the fluctuating pressure evolution in the streamwise direction and in time. Figure 4.19 shows an excellent coherence between the DNS and DMD computations. Pressure perturbations p' that evolves over a total time corresponding to 5 periods of the second subharmonic $f_0/4$ inside the near-field mixing region of the flow, for example, at the center of computational domain, is depicted in figure 4.20. Again, excellent agreement between DMD analysis and DNS are observed.

Then, the far-field acoustic behaviour is investigated both quantitatively and qualitatively. The projected pressure field given by the DMD prediction is shown in figure 4.21 (b). The acoustic interference pattern is in close agreement with that obtained from the DNS, shown in figure 4.21 (a), and illustrate the acous-

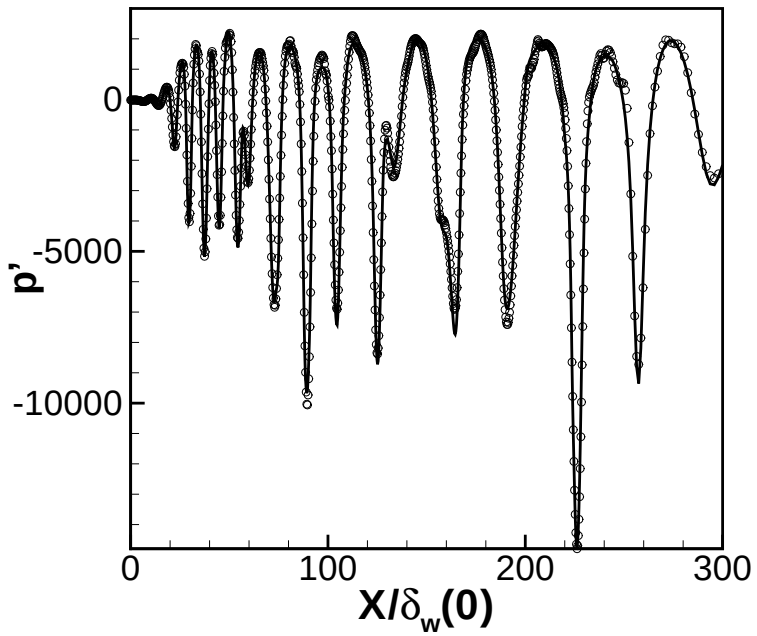

Figure 4.19: Streamwise evolution of the pressure perturbations $p'(x)$ along the centerline $y = 0$. Perturbations from DNS are shown in solid line, perturbations from DMD are depicted in circles.

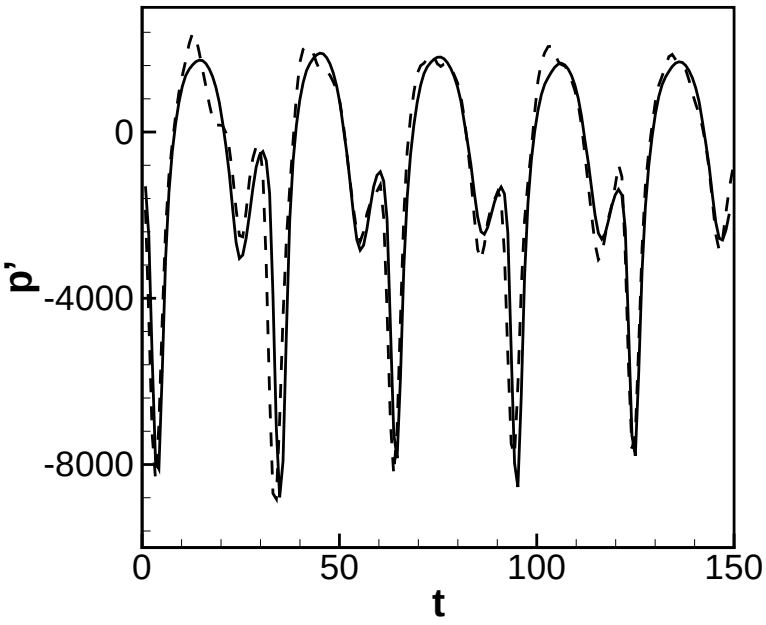

Figure 4.20: Pressure fluctuations p', as a function of time at the center of the domain. Perturbations from DNS are shown in solid line, perturbations from DMD are depicted in dashed line.

tic field resulting from vortex sound generation. Additionally, the amplitudes of the radiated sound can be evaluted by plotting the r.m.s. of the pressure fluctuation along the arc $110\delta_\omega(0)$ away from the source locations. We consider the saturation points as the apparent source locations (Colonius, Lele & Moin [30]). In this double pairing case, two source origins have been identified: $(x, y) = (67\delta_\omega(0), 0)$ and $(x, y) = (144\delta_\omega(0), 0)$. The results from the DNS and DMD is shown in figures 4.22 and 4.23. The peak acoustic intensities are then identified: one is in the direction $\theta \approx 44^\circ$ with the acoustic intensity about 127 dB and 126 dB. A more quantitative comparison can be carried out by plotting the streamwise evolution of the pressure $p'(x)$ at two vertical locations: inside the shear regions of the flow (at $y = 0$) and in the far field ($y = 110\delta_\omega(0)$), shown in figures 4.19 and 4.24. Not surprisingly, in the near-field region of the flow the pressure perturbations $p'(x, y = 0)$ along the centerline are very well predicted by the DMD computation. Nevertheless, in the acoustic field (at $y = 110\delta_\omega(0)$) the prediction from DMD compares favorably with the DNS calculation. The behaviour of the pressure eigenfunction is further explored by considering the cross-sections of the pressure in the y direction at different streamwise locations. At a point upstream of the first vortex pairing location, the fluctuating pressure $|p'(x = 55\delta_\omega(0), y)|$ is considered in figure 4.25. The pressure calculated by DMD agrees perfectly with its directly computed counterpart. The pressure is again plotted around the second vortex pairing position, say $x = 155\delta_\omega(0)$, (figure 4.26), both methods predict the same trend of decay of the pressure eigenfunction. Further downstream of these two vortex pairing locations the DMD prediction and direct computations of the far field begin to diverge, the pressure calculated by DMD is approximately 1.5 orders of magnitude larger than the direct calculation, as shown clearly in figure 4.27. Lastly, the time history of pressure signal in the far-field region (say, $y = 110\delta_\omega(0)$) can be plotted in figure 4.28, we see that the temporal behaviour of the fluctuating pressure can be in large measure captured by the DMD reconstruction.

4.2.3 Coherent structures extraction from the subdomain DMD analysis

In the previous section, we have demonstrated that the DMD performed over the entire flow field is capable of predicting accurately both the aerodynamics and aeroacoustics of the shear layer. The flow field can be totally recovered by a few Koopman modes extracted from the DMD analysis. Since the coherent structures are responsible for the acoustic radiation in the far field, their accurate description is essential to the understanding of the aeroacoustics of the mixing layer. In this section, we will see if the associated Koopman modes can be extracted correctly from the DMD computation only carried out in a portion of the flow field. We first define a subdomain that will be used in this set of calculation. To take the larger wavelength of the second subharmonic into account, we choose a subdomain that extends a little more in the cross-stream section, that is, $-55 < y/\delta_\omega(0) < 55$. We then perform a series of computations when varying the number of snapshots N from 100 to 300. Note that the incompressible inner product is adopted as in the previous section. The peak values of the angular frequency ω_r resulting from these computations are tabulated in Table 4.2. Two observations can be made. First, these values of ω_r are very close to those obtained from the DMD performed in the full domain

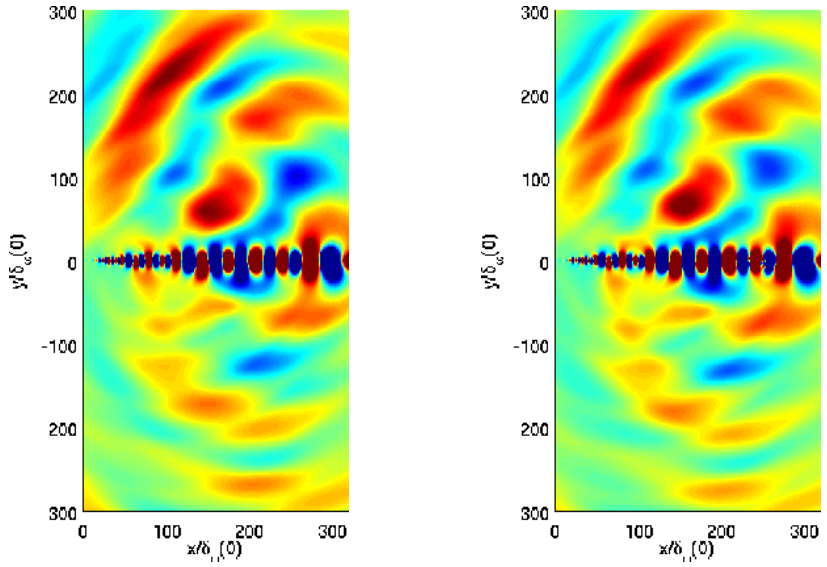

(a) (b)

Figure 4.21: (a) Acoustic field from DNS. (b) Acoustic field from DMD. Pressure fluctuations are shown in the physical domain. Levels from −300 Pa to 300 Pa in both figures.

(see table 4.1). Secondly, the values seem to remain constant even though N is increased. Therefore, the dominant modes are extracted properly by the DMD analysis. The maximum number $N = 300$ will be considered in the following investigation. Figure 4.29 show the eigenvalues and energy spectrum. The most energetic Koopman modes are identified as before: $f_0/2$, $f_0/4$, f_0, $3f_0/4$, $3f_0/8$ and $f_0/8$. The corresponding Koopman modes after projecting them onto the initial DNS snapshot defined in 3.18 are shown in figures 4.30, 4.31, 4.32, 4.33, 4.34 and 4.35 respectively. Similar features are found when compared to the zoom in from the DMD analysis in the full domain. The behaviours of the instability waves in the near-field region are further explored by comparing their spatial and temporal evolutions from the DNS and the DMD calculations. The reconstructed roll up and vortex pairing events during one period of $f_0/4$ is illustrated by plotting the total spanwise vorticity in the mixing region, depicted in figure 4.36. When compared to its directly computed counterpart (see figure 4.17), the roll up and vortex pairing mechanisms are well captured by the DMD computation. Cross-sections of the velocity perturbations $v'(x)$ along $y = 0$ are also plotted to compare the spatial development of the near-field coherent structures (see figure 4.37). We see that the spatial evolution of the coherent structures can be totally predicted by our modal decomposition. Likewise, the temporal evolution of the perturbations, for example, p', during 5 periods of $f_0/4$ at a certain location, say at the center of the domain, matches closely that of the DNS calculation, as shown in figure 4.38. Given these examinations, the DMD method performed both over the full flow field and only a subdomain have proven itself a relevant tool to describe the flow structures representing

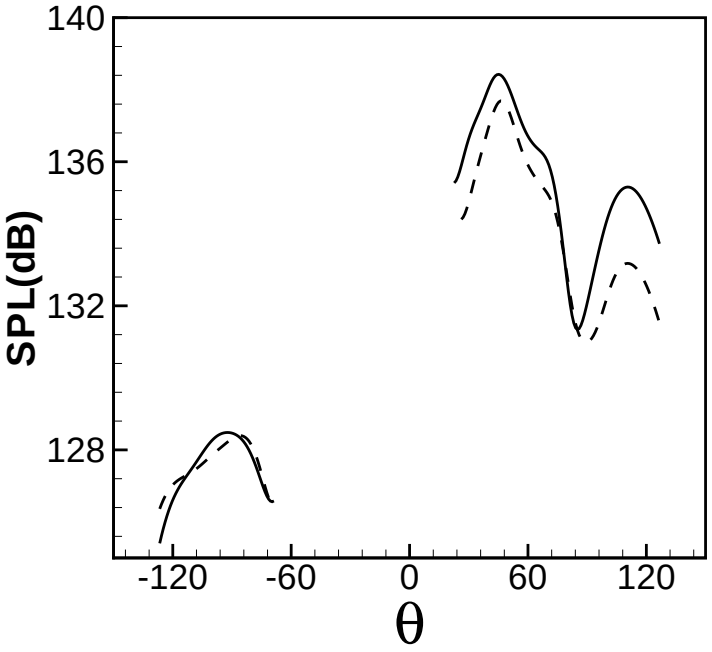

Figure 4.22: Far-field directivity for a radius at $110\delta_\omega(0)$ from the noise source located at $x = 67\delta_\omega(0)$ and $y = 0$ from DNS (solid line), from DMD (dashed line).

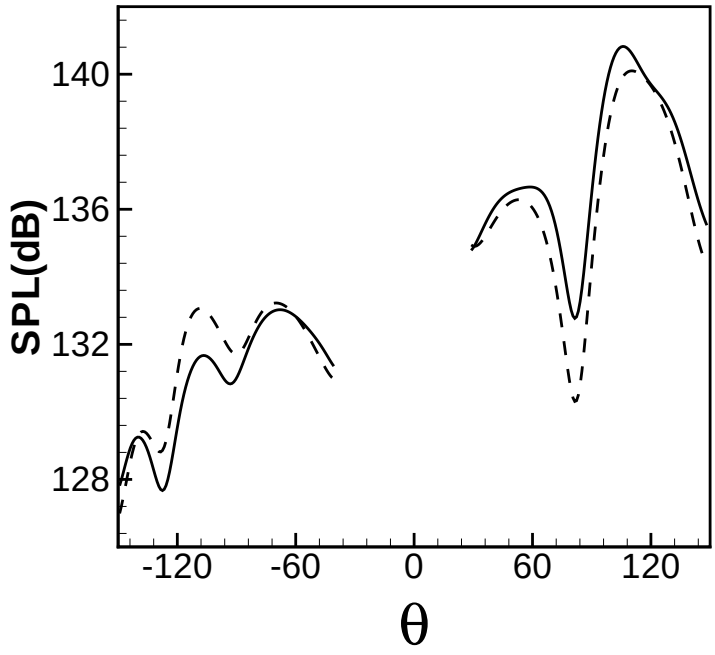

Figure 4.23: Far-field directivity for a radius at $110\delta_\omega(0)$ from the noise source located at $x = 144\delta_\omega(0)$ and $y = 0$ from DNS (solid line), from DMD (dashed line).

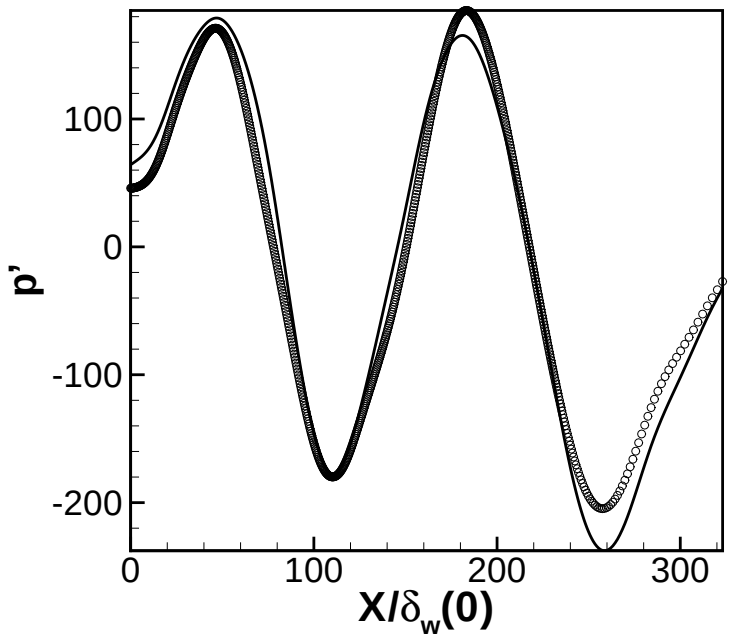

Figure 4.24: Streamwise evolution of the pressure perturbations $p'(x)$ along $y = 110\delta_\omega(0)$. Perturbations from DNS are shown in solid line, perturbations from DMD are depicted in circles.

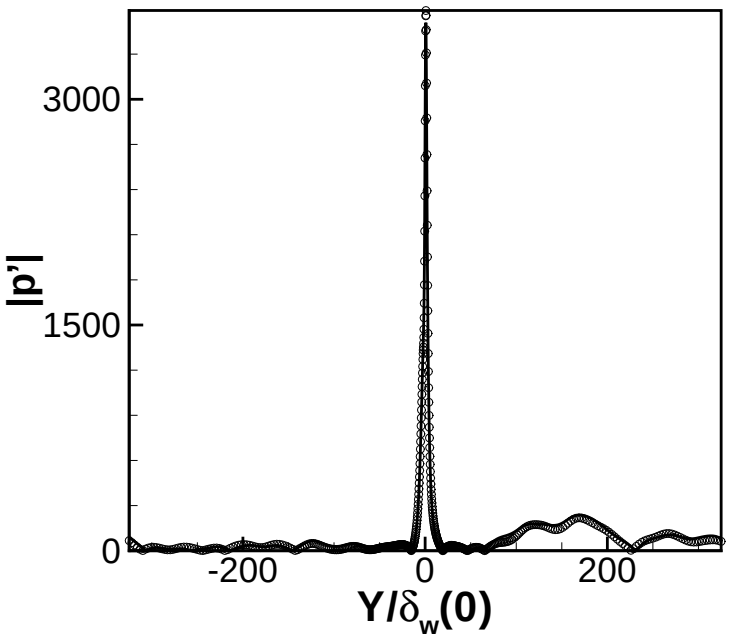

Figure 4.25: Cross-stream pressure perturbations $|p'(y)|$ at the downstream position $x = 55\delta_\omega(0)$. Perturbations from DNS are shown in solid line, perturbations from DMD are depicted in circles.

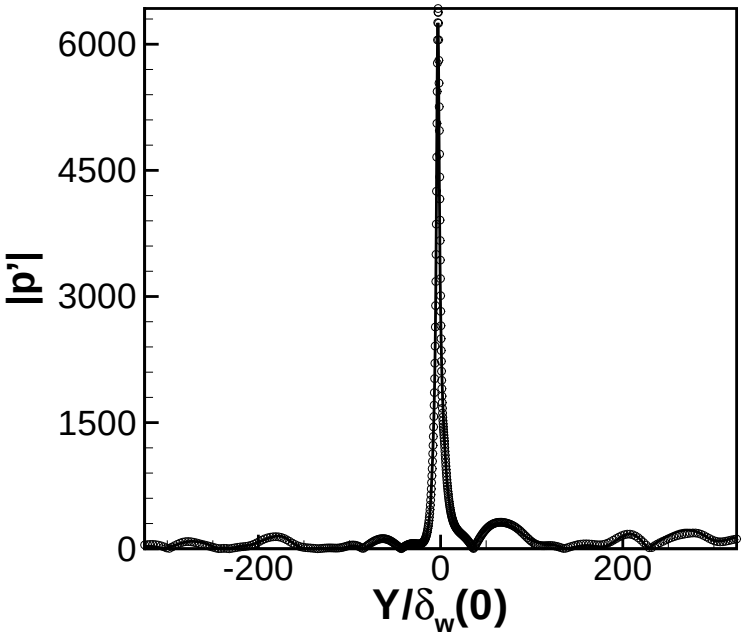

Figure 4.26: Cross-stream pressure perturbations $|p'(y)|$ at the downstream position $x = 155\delta_\omega(0)$. Perturbations from DNS are shown in solid line, perturbations from DMD are depicted in circles.

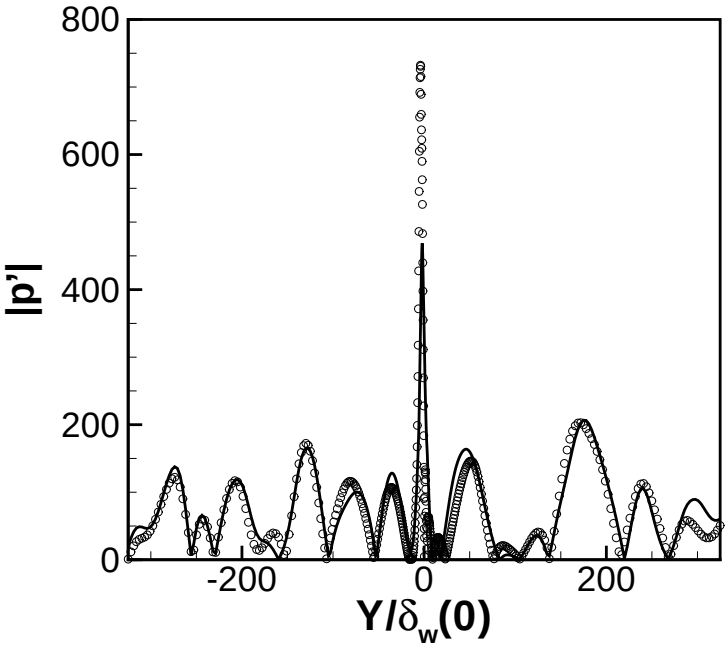

Figure 4.27: Cross-stream pressure perturbations $|p'(y)|$ at the downstream position $x = 218\delta_\omega(0)$. Perturbations from DNS are shown in solid line, perturbations from DMD are depicted in circles.

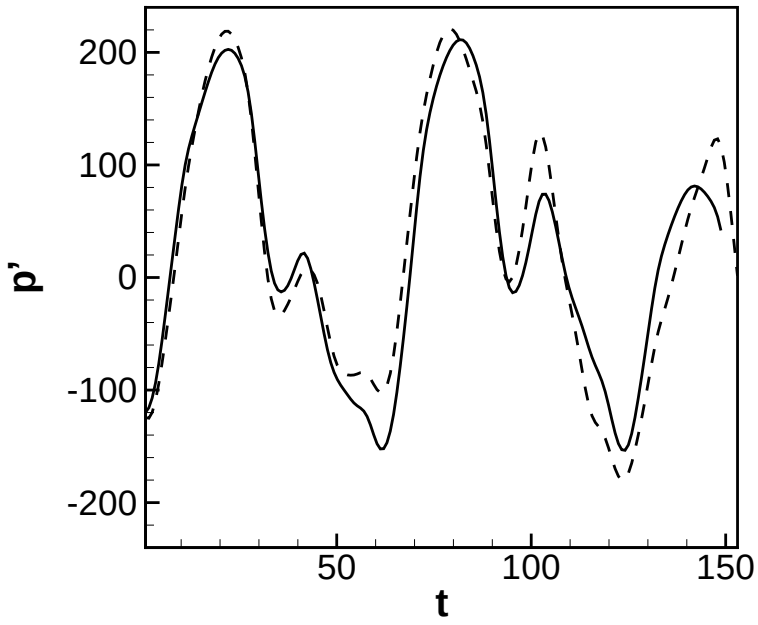

Figure 4.28: Pressure fluctuations p', as a function of time in the far field $x = 67\delta_\omega(0), y = 110\delta_\omega(0)$. Perturbations from DNS are shown in solid line, perturbations from DMD are depicted in dashed line.

N	$f_0/4$	$f_0/2$	f_0	$3f_0/4$	$3f_0/8$	$f_0/8$
100	0.208	0.415	0.622	0.828	0.308	0.120
150	0.207	0.415	0.624	0.830	0.308	0.120
200	0.207	0.414	0.623	0.830	0.309	0.120
250	0.206	0.415	0.622	0.829	0.309	0.121
300	0.206	0.415	0.622	0.830	0.309	0.121

Table 4.2: Dominant values of angular frequency ω_r as the number of snapshots N is increased from 100 to 300 using the incompressible inner product.

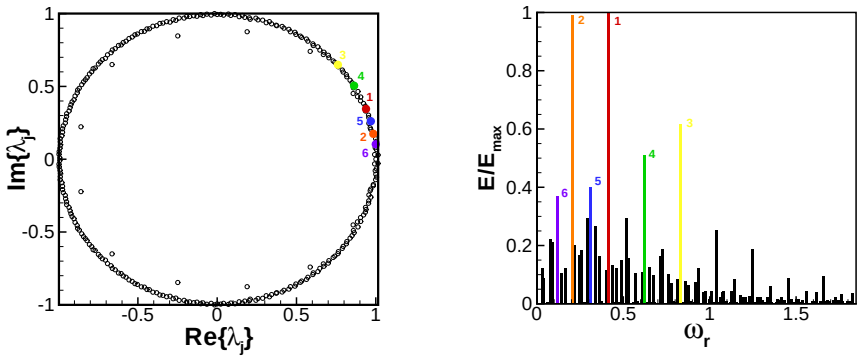

(a) (b)

Figure 4.29: DMD analysis performed over the near-field subdomain using 300 snaphots: (a) Ritz values λ_j. (b) Energy spectrum of the Koopman modes at each angular frequency ω_r. In both figures, the Ritz values associated with the most energetic modes are marked with 1, 2, 3, 4, 5 and 6, respectively.

the dominant dynamical information in the underlying fluid flow.

4.2.4 DMD analysis within a spatial framework

Previously, we have investigated the development of the near-field coherent structures in the flow through the DMD analysis within a temporal framework. Now, as demonstrated in the single pairing case, a DMD analysis within a spatial framework can also be adopted to study the impact of near-field large coherent structures evolution on the far-field. In the present case where two sources coexist, we shall perform the spatial DMD analysis over the top and bottom domains separately, and then for each domain, the two sources are considered in turn. Four zones are then extracted and shown in figure 4.39. More precisely, the zones extracted from the top domain for the first and second source extend over $50 \leq R/\delta_\omega(0) \leq 250$, $20^\circ \leq \theta \leq 100^\circ$ and $40 \leq R/\delta_\omega(0) \leq 315$, $67^\circ \leq \theta \leq 117^\circ$, respectively; the zones extracted from the bottom domain for the first and second source extend over $50 \leq R/\delta_\omega(0) \leq 300$, $-100^\circ \leq \theta \leq -30^\circ$ and $40 \leq R/\delta_\omega(0) \leq 315$, $-118^\circ \leq \theta \leq -50^\circ$, respectively. The centers of each zone associated with the polar coordinates correspond to the appar-

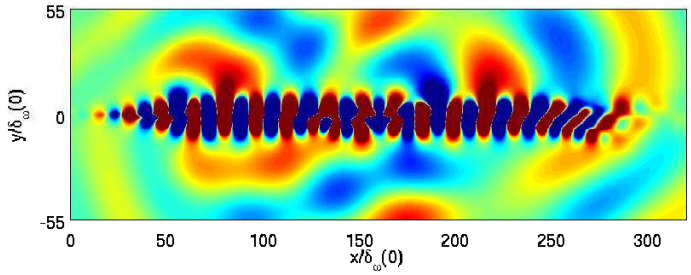

Figure 4.30: The Koopman mode at $f_0/2$ using the pressure fluctuations. Levels from -50 Pa to 50 Pa.

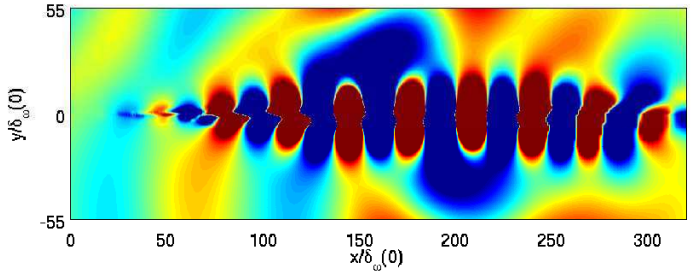

Figure 4.31: The Koopman mode at $f_0/4$ using the pressure fluctuations. Levels from -50 Pa to 50 Pa.

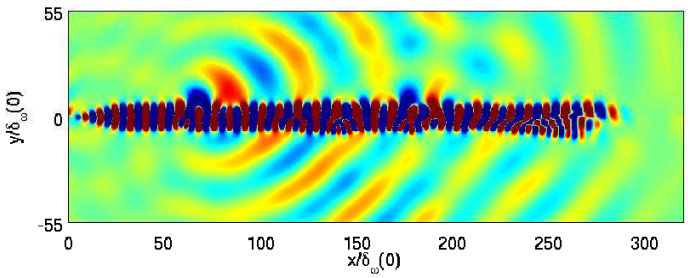

Figure 4.32: The Koopman mode at f_0 using the pressure fluctuations. Levels from -10 Pa to 10 Pa.

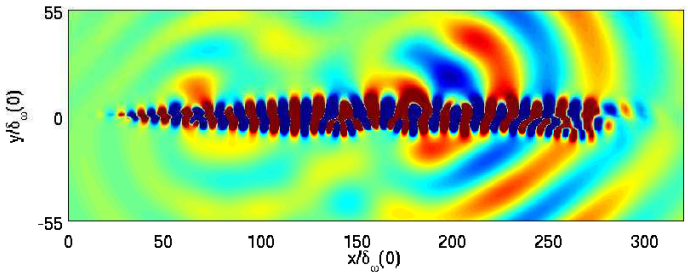

Figure 4.33: The Koopman mode at $3f_0/4$ using the pressure fluctuations. Levels from -10 Pa to 10 Pa.

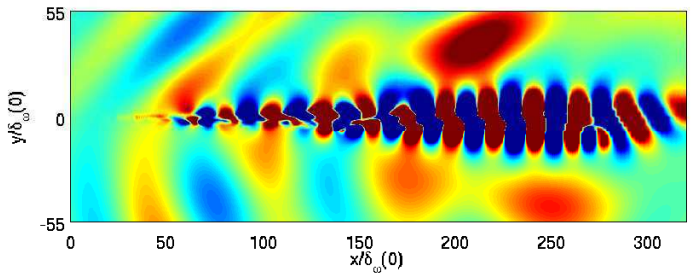

Figure 4.34: The Koopman mode at $3f_0/8$ using the pressure fluctuations. Levels from -10 Pa to 10 Pa.

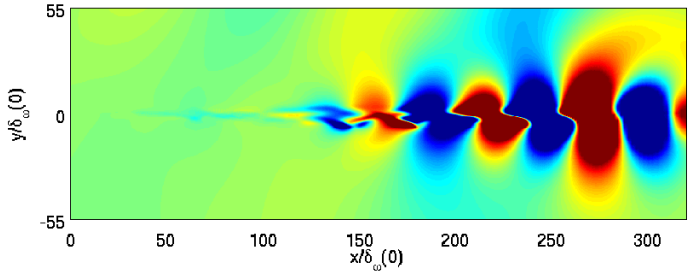

Figure 4.35: The Koopman mode at $f_0/8$ using the pressure fluctuations. Levels from -10 Pa to 10 Pa.

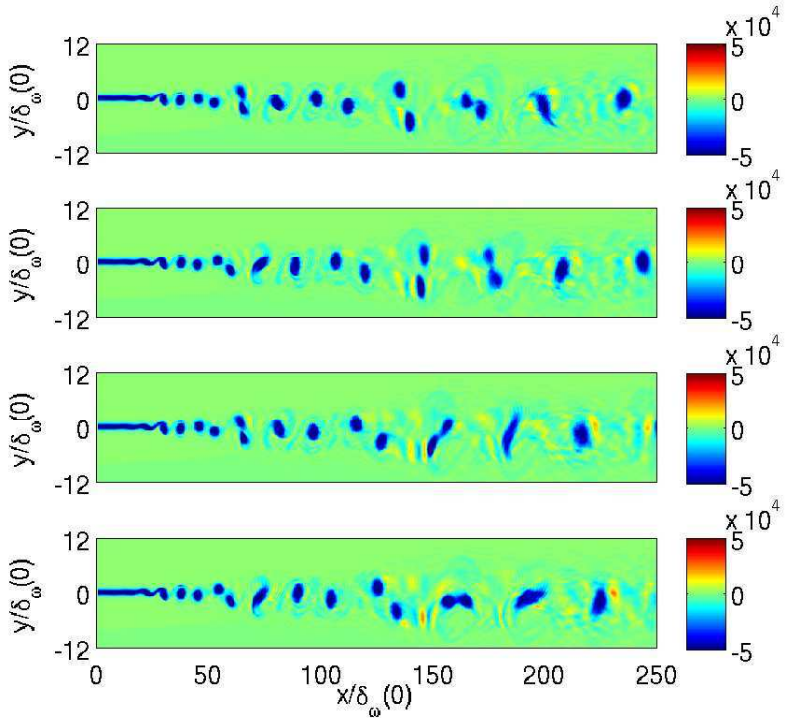

Figure 4.36: Follow-up of the vortex pairing at four successive equidistant instants over one period of $f_0/4$ in the near-field mixing region from DMD. Total spanwise vorticity is shown. Levels from -5×10^5 /s to 5×10^5 /s.

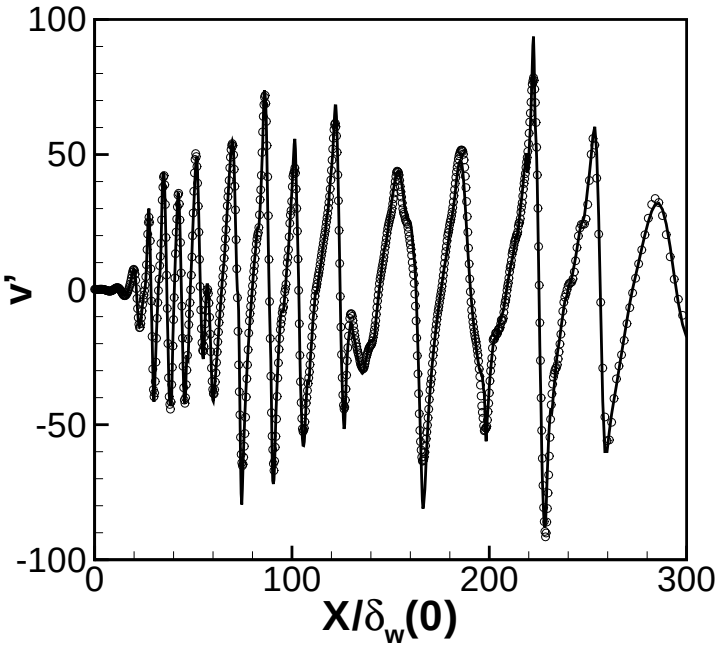

Figure 4.37: Streamwise development of the velocity perturbations $v'(x)$ along the centerline $y = 0$. Perturbations from DNS are shown in solid line, perturbations from DMD are depicted in circles.

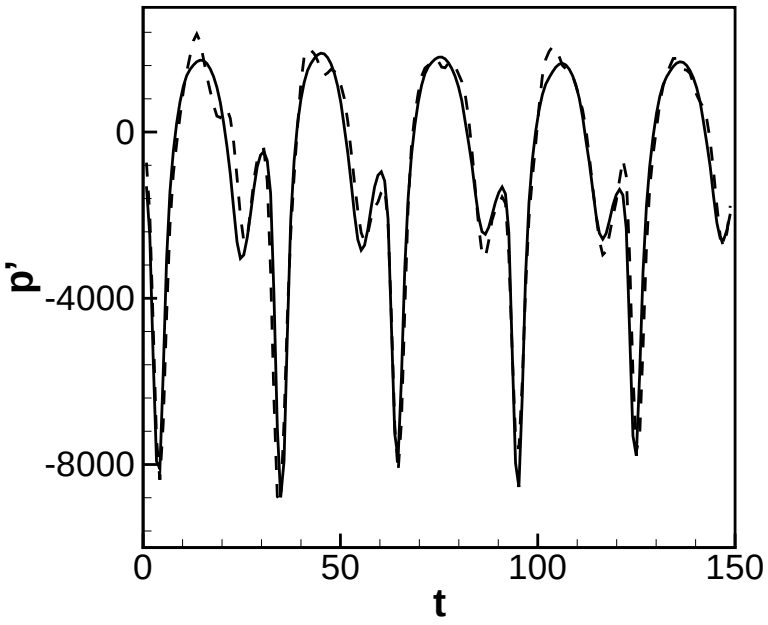

Figure 4.38: Pressure fluctuations as a function of time $p'(t)$ at the center of the subdomain $(128\delta_\omega(0), 0)$. Perturbations from DNS are shown in solid line, perturbations from DMD are depicted in dashed line.

ent source locations: $(67\delta_\omega(0), 0)$ and $(144\delta_\omega(0), 0)$, based on the observations from the DNS and DMD computations. The distance between every two snapshots is considered regular: $\Delta R = 1.818$. The spatial spectra resulting from the DMD analysis in the top domain are shown in figure 4.40. For the first source, only one mode is exhibited. The wavelength is deduced from this figure: $\lambda = 2\pi/\alpha_R = 2\pi/0.1 = 60$, and appears to correspond to the value of wavelength of the main acoustic wave of the first source. Its spatio-temporal evolution is illustrated in figure 4.41 (a) by plotting the fluctuating density ρ' in $(\theta - t)$- plane. By Fourier transforming the density fluctuations in time (see figure 4.41 (b)), we obtain the dominant angular frequency: $\omega_r \approx 0.415$. By contrast, for the second source, two modes detach from the spectra. The associated wavelengths are $\lambda = 2\pi/0.06 = 104$ and $\lambda = 2\pi/0.04 = 160$, respectively. These wavelengths correspond to those of $f_0/4$ and $f_0/8$. Likewise, the space-time behaviours of these two eigenmodes can be shown in figures 4.42 (a) and 4.43 (a), respectively. The peak angular frequencies are $\omega_r \approx 0.207$ and $\omega_r \approx 0.103$, shown in figures 4.42 (b) and 4.43 (b), respectively. These values of frequencies correspond well to the frequencies of the dominant modes: $f_0/4$ and $f_0/8$. In the same way, the spatial DMD analysis is performed over the lower domain, the resulting spectra are shown in figure 4.44. As in the top domain, the eigenmode $f_0/2$ always appears for the first source. However, for the second source, it is no longer $f_0/8$ but $f_0/2$ detaches from the spectra. Their spatio-temporal evolutions are shown in figures 4.45 (a), 4.46 (a) and 4.47 (a), respectively. Furthermore, we apply the Fourier transform at every point of the domain to $f_0/2$ (figure 4.45 (b)) in order to get an interpretation of the entire physical space in Fourier space. We see that the mode $f_0/2$ dominates for the first source. Concerning the directivities of the propagating acoustic waves in the far field, they appear much less net compared to the single pairing case because of the interferences of several waves. However, the spatial DMD analysis provides us with an approximated main direction with respect to each of the sources. Furthermore, one observe as in the single pairing case a constant angular velocity of the acoustic waves because of the convection effects of the acoustic waves and refraction effects by the velocity gradient in the near-field shear layer. Since several spatial structures associated with the dominant frequency emerge in this case, we observe a decrease in the angular velocity. This phenomenon can be explained by the fact that the high-frequency waves are more influential by the refraction effects.

For this double pairing case, we conclude that the DMD analysis within the temporal framework is appropriate to describe the dynamics of the coherent structures in the near field: such as the roll up and vortex pairing processes. The resulting acoustic radiation becomes more complex caused by more than one existing sound source, however, it is quite well captured by the temporal DMD. On the other hand, the spatial DMD analysis has been used to characterize the acoustic waves features in the far field, such as, the directivities, wavenumbers and frequencies, the results are satisfactory. Therefore, the relation between the far-field radiated sound field and the coherent structures in the near field can be established.

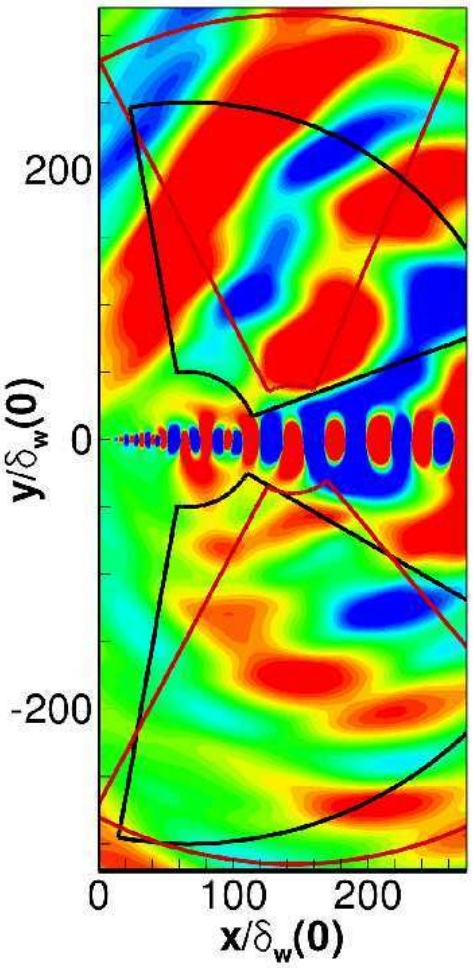

Figure 4.39: Extracted zones used in the spatial DMD analysis for the first source are shown in black lines; for the second source are shown in red line.

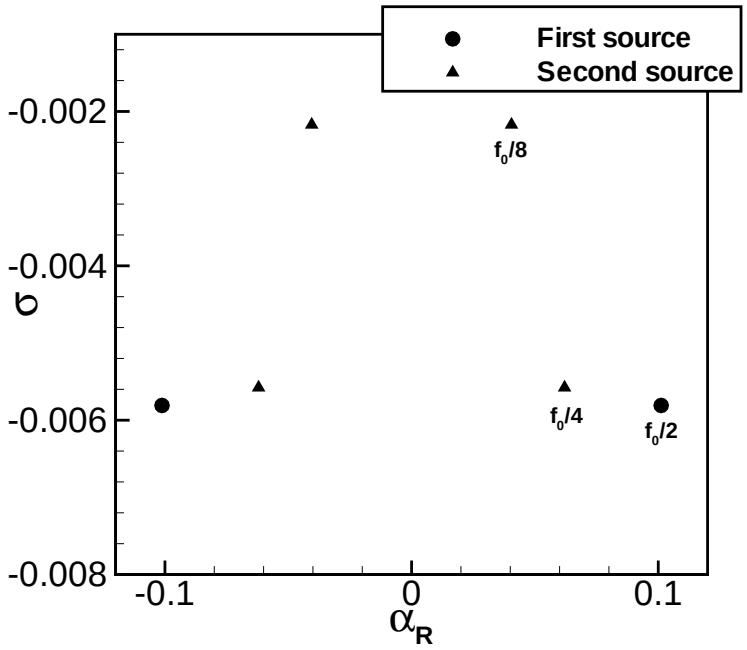

Figure 4.40: Spatial spectra from the spatial DMD analysis performed over the top domain. The spatial growth rate σ is plotted versus the wavenumber α_R. The modes with the wavenumbers $\alpha_R \approx 0.1$, $\alpha_R \approx 0.06$ and $\alpha_R \approx 0.04$ correspond to the mode $f_0/2$, $f_0/4$ and $f_0/8$, respectively.

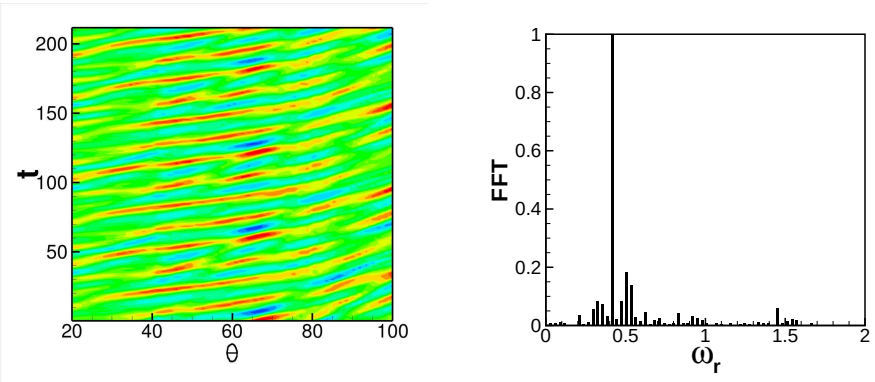

(a) (b)

Figure 4.41: (a) Spatial DMD analysis performed in the top domain for the first source: the dominant frequency is $f_0/2$, we associate this spatial structure with $f_0/2$. Density perturbations are plotted as a function of the angle θ and time t. (b) Fourier transformed in time gives the peak frequency.

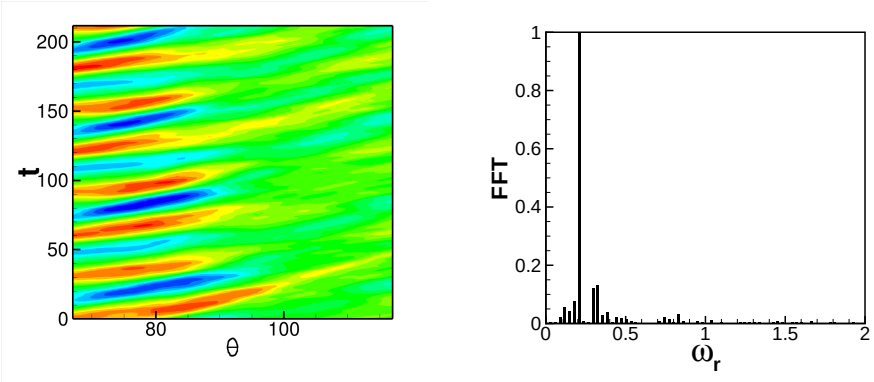

(a) (b)

Figure 4.42: (a) Spatial DMD analysis performed in the top domain for the second source: the dominant frequency is $f_0/4$, we associate this spatial structure with $f_0/4$. Density perturbations are plotted as a function of the angle θ and time t. (b) The dominant frequency detaches near $f_0/4$ through the Fourier transformed density fluctuations in time.

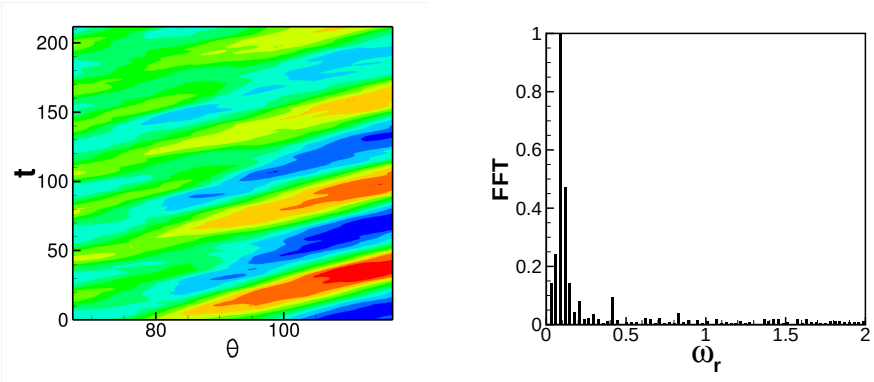

(a) (b)

Figure 4.43: (a) Spatial DMD analysis performed in the top domain for the second source: the dominant frequency is $f_0/8$, we associate this spatial structure with $f_0/8$. Density perturbations are plotted as a function of the angle θ and time t. (b) The peak frequency corresponds to $f_0/8$ through the Fourier transformed density fluctuations in time.

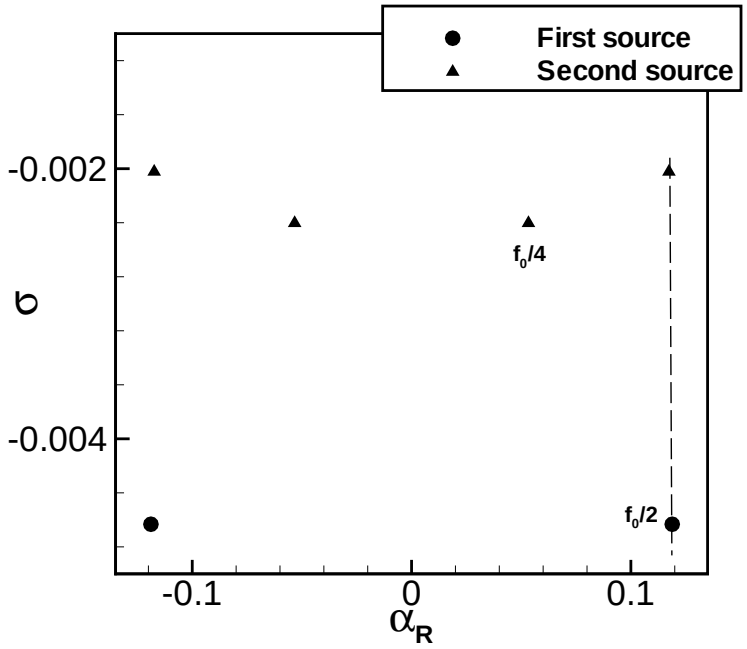

Figure 4.44: Spatial spectra from the spatial DMD analysis performed in the lower domain. The spatial growth rate σ is plotted versus the wavenumber α_R. The modes with the wavenumbers $\alpha_R \approx 0.12$ and $\alpha_R \approx 0.06$ correspond to the mode $f_0/2$ and $f_0/4$, respectively.

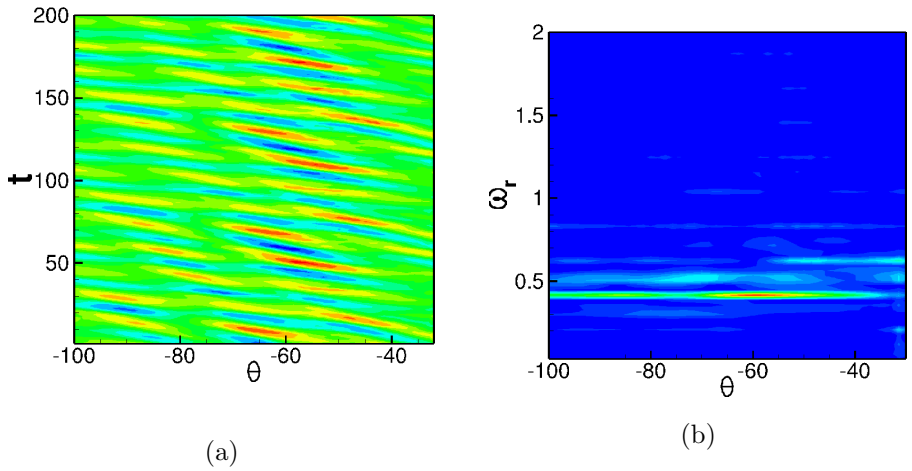

(a) (b)

Figure 4.45: (a) Spatial DMD analysis performed in the lower domain for the first source: the dominant frequency is $f_0/2$, we associate this spatial structure with $f_0/2$. Density perturbations are plotted as a function of the angle θ and time t. (b) The peak frequency corresponds to $f_0/2$ through the Fourier transformed density fluctuations in time.

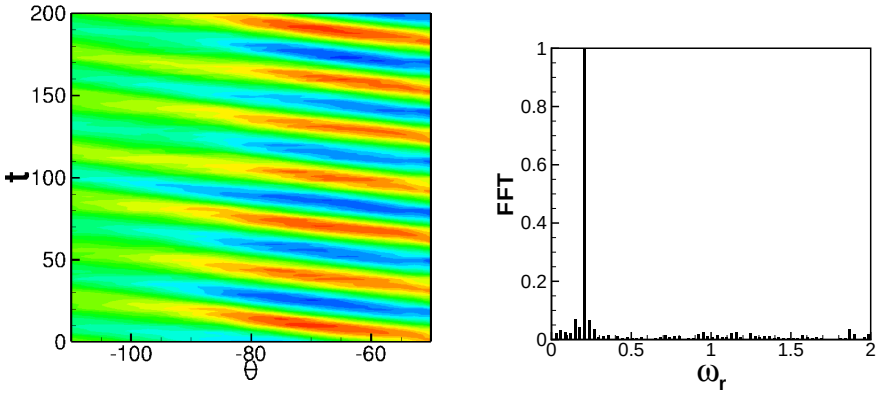

(a) (b)

Figure 4.46: (a) Spatial DMD analysis performed in the lower domain for the second source: the dominant frequency is $f_0/4$, we associate this spatial structure with $f_0/4$. Density perturbations are plotted as a function of the angle θ and time t. (b) The peak frequency corresponds to $f_0/4$ through the Fourier transformed density fluctuations in time.

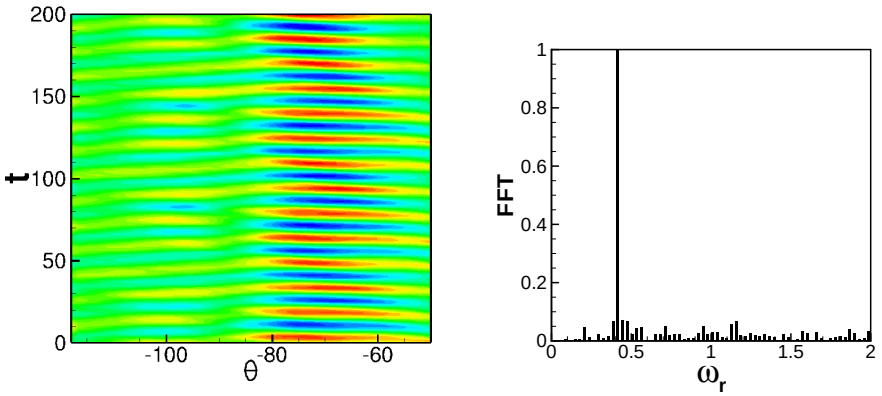

(a) (b)

Figure 4.47: (a) Spatial DMD analysis performed in the lower domain for the second source: the dominant frequency is $f_0/2$, we associate this spatial structure with $f_0/2$. Density perturbations are plotted as a function of the angle θ and time t. (b) The peak frequency corresponds to $f_0/2$ through the Fourier transformed density fluctuations in time.

Chapter 5

Conclusions

This chapter contains an overview of results and some suggestions for future work.

5.1 Summary

A Navier-Stokes compressible solver in perturbative formulation in two and three dimensions has been developed to investigate the far-field noise production of subsonic shear layers. A set of linearized and fully nonlinear simulations serving as a reference have been performed for a compressible two-dimensional mixing layer, also the snapshots extracted from the DNS data were used subsequently in the modal decomposition analyses. Modal decomposition techniques based on snapshots of numerical simulations in both a linear and nonlinear approaches have been developed to describe the coherent structures that are representives of the flow dynamic features and the acoustic radiations. The relevance of these tools have been illustrated on a co-flowing mixing layer examples, which is a typical noise amplifier.

For the case of a linear process, a global stability analysis has been performed to characterize the instability waves behaviours of the flow, such as fundamental frequencies emerged in the underlying fluid flow (e.g. the most unstable frequency). And then, modal decompositions based on the global modes in both temporal and frequency domain was carried out to examine the typical noise-amplifier-type dynamics of the mixing layer. The linear global stability analysis has been shown capable of predicting the characteristic frequencies of the flow. Contrary to the supersonic flows, no sound was predicted by this linear model even with the combined forcing f_0 and $f_0/2$ as in the direct simulations. The global mode decomposition was not sufficient to capture the vortex pairings processes and the resulting acoustic radiation. An additional nonlinear mechanism is then required.

In a nonlinear model, the Dynamic Mode Decomposition (DMD), recently proposed by Schmid *et al.*[98] within both a temporal and a spatial framework have been developed and applied to compressible flows. Two flow configurations are considered: one single vortex pairing case and double pairing case. First, based on a few Koopman modes which represent near-field coherent structures, the vortex pairing processes and the acoustic radiation characteristics of a typi-

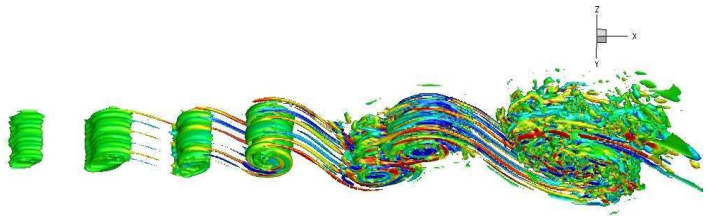

Figure 5.1: Total vorticity field of the three-dimensional coflow mixing layer ([105]). View of an isosurface of the Q-criterion at the value 10^{-5} colored with the streamwise vorticity (levels between $\pm 10^5$ /s).

cal subsonic mixing layer has been completely predicted by a temporal analysis of the DMD. Moreover, the possibility to use subsets of the full numerical simulation has been highlighted. Furthermore, it has been illustrated that the use of snapshots of the near field is relevant to capture coherent structures which are involved in source terms of the Lightill equation. In particular, a Lightill's analogy based on these coherent structures predicts correct directivity and sound pressure levels compared to DNS values.

Secondly, proceeding with the spatial DMD analysis, interesting acoustic characteristics such as the directivities, angular velocities of the acoustic wave propagation varying according to their spatial size and their typical frequencies have been satisfactorily captured. The spatial analysis offered therefore an efficient analysis tool to describe the far-field sound radiation process and their link to the near-field coherent structures. It should be mentioned the general character with respect to these analysis tools: no weakly parallelism assumption. Starting from a relatively simple flow configuration, we are now confident about the performance of our analysis tools to apply to more complex flow configurations.

Finally, one may precise that the Navier-stokes solver in three dimensions has been well validated and applied to the three-dimensional flow cases (see Song [105]). For instance, a numerical simulation in three dimensions has been carried out, here we show a snaphot of the total vorticity using the Q-criterion [59]. We should take into consideration of the expensive cost in computer resources. A difficult task remains the forcing at the inlet of the mixing layer in three-dimensional simulations, which has not often be treated in the literature (e.g. Babuke, Kloker & Rist [4]).

5.2 Suggestion for future work

Throughout this thesis, we have developed a reduced-order model based on the Koopman mode decomposition, howerver, a method commonly used is the POD/Garlerkin ROM. It seems then natural to compare these two decomposition methods. It will be also interesting to test the robustness of the Koopman ROM, for instance, beyong the DNS temporal window.

Furthermore, the modal decomposition method developed in this thesis allows to establish a hierarchy of coherent structures involved in the sound production. A natural evolution of this work should be dedicated by manipulating

such modes in order to significantly reduce the noise production. Control theory regarding sensitivity analysis of aeroacoustic noise radiated from the flow with respect to particular changes induced by local perturbations of mass and energy is a first step to illuminate what type of control is required, and how the original noisy flow can be quieted (Spagnoli & Airiau [106]). Adjoint modes of the Koopman modes derived from an optimization of a functional cost which has to be determined, should give some new insight into noise control.

Work may be dedicated to implementing a full optimal control technique and proposing a relevant functional which provides the measure of the radiated noise. Direct-adjoint iterations relied upon the reduced-order model based on Koopman modes should be useful to minimize the optimization time in order to deduce the forcing leading to an optimal noise reduction (Wei & Freund [118]). More specially, a functional cost associated with a spatial amplification rate determined by a DMD analysis within the spatial framework performed over the far field, might be an interesting idea.

Finally, as noticed in the introduction, although a mixing layer flow appears as an academic flow, it exhibits a wide variety of space and time dynamics, depending upon a wide range of parameters, such as shear intensity, Mach number or heating effects. In particular, we can cite a counterflow mixing layer with a pocket of absolute instability, which could be an enlightening case. In this respect, the Appendix is dedictated to a preliminary analysis of such a flow configuration. We hope that this methodology may be applied to more complex flow configurations, for instance, the supersonic flows where instability wave radiate directly in the linear regime; or else complex three-dimensional flows, for instance, the cavity flows or airfoils...

Appendix

Counterflow mixing layer

It is convenient to characterize the mixing layer by the nondimensional parameter R, called the velocity ratio (Ho & Huerre [51]). R measures the relative magnitude of the shear ΔU with respect to the convection velocity U_c: $R = \Delta U/(2U_c)$. A counterflow mixing layer is produced if $R > 1$, whereas a co-flowing mixing layer is generated if $R < 1$. Contrary to co-flowing mixing layers, typical noise amplifiers which are sensitive to external noise, counterflow mixing layers are known to behave as flow oscillators with a well-defined frequency that is insensitive to low level noise. To describe these two distinct qualitative nature of open flow dynamical behaviours, the concepts of convective and absolute instabilities were developed by Huerre & Monkewitz [56] are often used. In this context, the impulse flow response localized in space and time is considered.

The linear impulse response of the counterflow mixing layer by means of a linear direct numerical simulation. The velocities of the upper and lower stream are -20 m/s and 100 m/s, respectively. Therefore, the velocity ratio is $R = 1.5$, the convection velocity is $U_c = 40$ m/s and the convective Mach number is 0.18. The Reynolds number based on the initial vorticity thickness of the mixing layer $\delta_\omega(0) = 1.6 \times 10^{-3}$m and the velocity difference across the layer ΔU, $Re = \Delta U \delta_\omega(0)/\nu$ is 13692. At initial time, we introduce the following impluse perturbations with minimal initial acoustic transient (Gloerfelt & Le Garrec [45]) at the center of computational domain $(0, 0)$

$$\begin{cases} u' = \gamma U_c y \exp\left[-\dfrac{\ln 2}{(3\Delta y_{min})^2}(x^2+y^2)\right] \\ v' = -\gamma U_c x \exp\left[-\dfrac{\ln 2}{(3\Delta y_{min})^2}(x^2+y^2)\right] \\ p' = \dfrac{\rho_\infty \gamma^2 U_c (3\Delta y_{min})^2}{4\ln 2} \exp\left[-\dfrac{2\ln 2}{(3\Delta y_{min})^2}(x^2+y^2)\right] \end{cases} . \tag{5.1}$$

The amplitude is $\gamma = 10^{-10}$. The half-width of the Gaussian function is $3\Delta y_{min}$. The computational domain extends over $-250 \leq x/\delta_\omega(0) \leq 250$, $-90 \leq x/\delta_\omega(0) \leq 90$, resolved with 801×281 points. The grid in x and y are uniform with minimal spacings $\Delta x_{min} = 0.32\delta_\omega(0)$ and $\Delta y_{min} = 0.16\delta_\omega(0)$, respectively. Numerical sponge zones are implemented at the streamwise and lateral boundaries to absorb outgoing acoustic waves with minimal reflection. The grid is stretched in the sponge zones.

An instability analysis is performed to compare the results obtained from

the above Linearized DNS calculation. Here, we adopt a spatio-temporal point of view, thus $\alpha \in \mathbb{C}$ and $\omega \in \mathbb{C}$. More specially, we are interested in the flow response to a linear impluse localized in space and time. This can be determined by the calculation of the Green function $G(x,t)$, defined as

$$\mathcal{L}G(x,t) = \delta(x)(t) \tag{5.2}$$

with the causality condition: $G(x,t) = 0$ if $t < 0$. Here, $\mathcal{L}$ denotes the operator of the differantial equations, associated with the dispersion relation $\mathcal{D}(\alpha,\omega)$. If we assume the base flow is homogeneous along the propagation direction x, the solution can be sought in the form of normal modes. The formulation in physical space of the Fourier-Laplace transform of the Green function is written as

$$G(x,t) = \frac{1}{4\pi^2}\int_L\int_F \frac{\exp\left[i(\alpha x - \omega t)\right]}{D(\alpha,\omega)} d\alpha d\omega \tag{5.3}$$

where L and F represent the integral contours along ω and α, respectively. We remark that the choice of the contour L should be positioned above all the singularities of the term of the integral (5.3), so as to respect the causality condition (see Huerre & Monkewitz [56] for details). The study of flow response in space and time amounts to the analyse of the behaviour of $G(x,t)$ defined by (5.3). This aspect is detailed in Huerre *et al.* [54].

If the flow is absolutely unstable, the wavepacket created at the initial time is no longer advected away from the source, but grows gradually to contaminate the entire flow. An symptotic study of the integral (5.3) allows to determine the behaviour of G, along each spatio-temporal ray $V = x/t$ by making use of the so-called method of steepest descent. This latter takes the form of a spatio-temporal wave as follows

$$G(x,t) \approx t^{-1/2} \exp i[\alpha^*(V)V - \omega^*(V)]t \tag{5.4}$$

where the couple (α^*, ω^*) verifies

$$\mathcal{D}(\alpha^*,\omega^*) = 0 \text{ and } \frac{\partial \mathcal{D}}{\partial \alpha}(\alpha^*,\omega^*) = V \tag{5.5}$$

with $V = x/t \in \mathbb{R}$. The space-time dynamics of G can be determined by the evolution of the temporal growth rate $\sigma(V)$ following each ray x/t

$$\sigma(V) = \omega_i^*(V) - \alpha_i^* V \tag{5.6}$$

In particular, if $\sigma(x/t = 0) > 0$, then the flow is absolutely unstable. Figure 5.2 (a) shows the temporal growth rate σ as a function of the spatio-temporal ray x/t obtained theoretically by solving the compressible Rayleigh equations. The propagation speeds of the upstream and the downstream fronts can be derived from this figure: $V^- = -0.1$ and $V^+ = 2.1$. They are compared to the values of the edges of the wavepacket by plotting the spatio-temporal diagram of the pressure perturbations resulting from the linearized simulation yielding $V^- \approx -0.105$ and $V^+ \approx 2.04$, shown in figure 5.2 (b). A good agreement between them are observed.

Figure 5.3 shows snapshots of the wavepacket resulting from the impulse perturbations introduced at the center of the domain $(0,0)$. Even without the

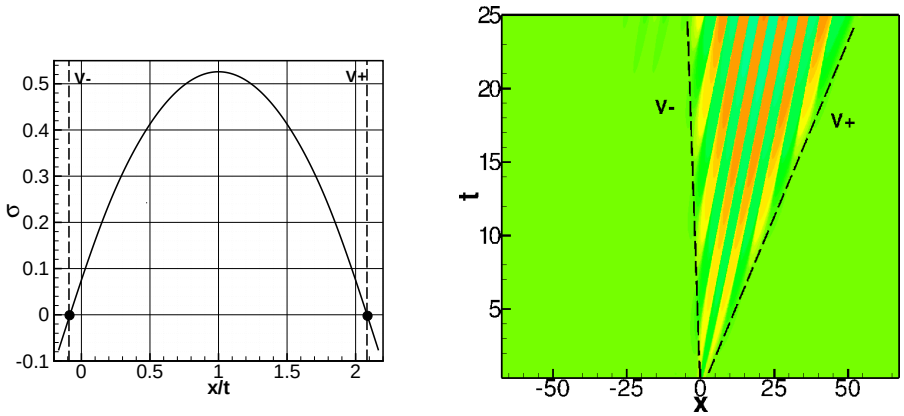

Figure 5.2: (a) Temporal growth rate σ versus the spatio-temporal ray x/t; (b) Spatio–temporal diagrams of the pressure perturbations. The edges of the wavepacket V^- and V^+ are shown in danshed lines.

continued external forcing, the flow is forced by the absolute instabilities that are generated by the initial impulse perturbations, and results in counter-rotating vortices in the upstream and downstream directions. This can be attributed to the main characteristics of an oscillator-type flow that is insensitive to the low-level external noise. We may observe that later several vortices tend to coalesce to form a larger vortex, and so on. This process becomes more and more random, and reaching a saturated regime seems less meaningful. However, we can postulate that a new mechanism of sound generation may be attributed to the vortex pairings in the transient regime before the saturated state.

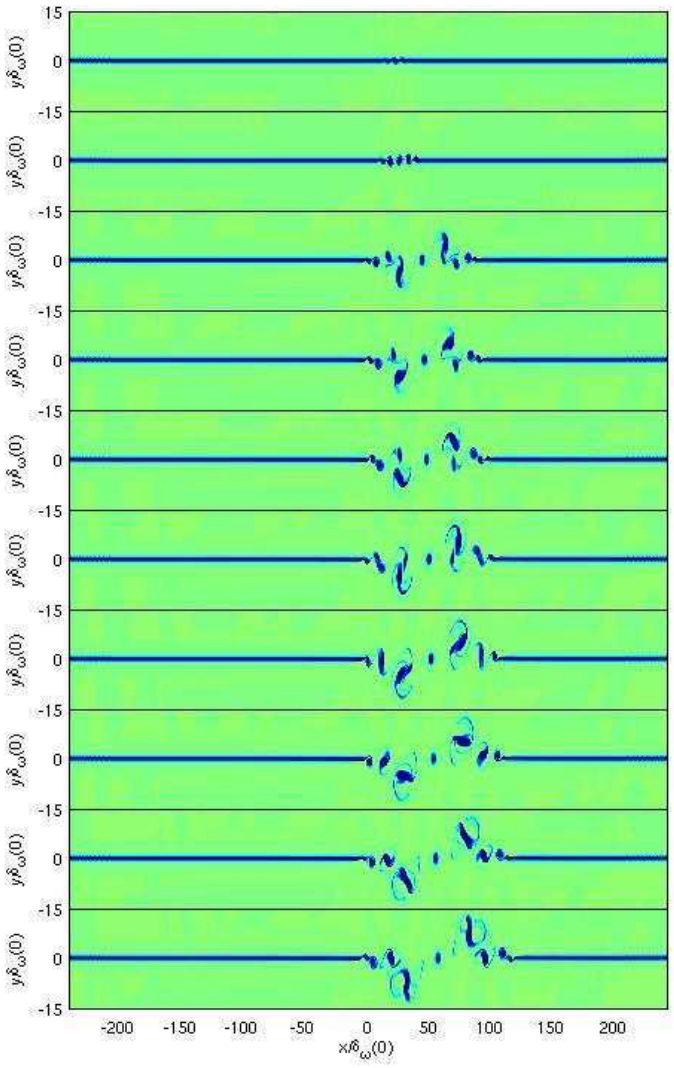

Figure 5.3: Snapshots of the wavepacket resulting from the impulse perturbations initially introduced at $(0, 0)$.

Bibliography

[1] F. Alizard. *Etude de stabilité linéaire globale d'écoulement fortement décollé de couche limite de plaque plane*. PhD thesis, Ecole Nationale Supérieure d'Arts et Métiers, 2007.

[2] F. Alizard and J.-C. Robinet. Modeling of optimal perturbations in flat plate boundary layer using global modes: benefits and limits. *Theor. Comp. Fluid Dyn.*, 1-4(25):147–165, 2011.

[3] N. Aubry, P. Holmes, J. L. Lumley, and E. Stone. The dynamics of coherent structures in the wall region of a turbulent boundary layer. *J. Fluid Mech.*, 192:115–173, 1988.

[4] A. Babucke, M. Kloker, and U. Rist. DNS of a plane mixing layer for the investigation of sound generation mechanisms. *Comput. Fluids*, 37:360–368, 2008.

[5] S. Bagheri. *analysis and control of transitional shear flows using global modes*. PhD thesis, Royal Institute of Technology, 2010.

[6] S. Bagheri, L. Brandt, and D. S. Henningson. Input–output analysis, model reduction and control design of the flat-plate boundary layer. *J. Fluid Mech.*, 620:263–298, 2009a.

[7] S. Bagheri, J. Hoepffner, P. J. Schmid, and D. S. Henningson. Input–output analysis and control design applied to a linear model of spatially developing flows. *Appl. Mech. Rev.*, 62:1–27, 2009.

[8] S. Bagheri, P. Schlatter, P. J. Schmid, and P. J. Henningson. Global stability of a jet in crossflow. *J. Fluid Mech.*, 624:33–44, 2009b.

[9] A. Barbagallo, D. Sipp, and P. Schmid. Closed-loop control of an open cavity flow using reduced-order models. *J. Fluid Mech.*, 641:1–50, 2009.

[10] D. Barkley, H. Blackburn, and S. J. Sherwin. Direct optimal growth analysis for timesteppers. *Int. J. Numer. Meth. Fluids*, 57:1435–1458, 2008.

[11] D. Barkley, M. G. Gomes, and R. D. Henderson. Three-dimensional instability in flow over a backward-facing step. *J. Fluid Mech.*, 473:167–190, 2002.

[12] M. Bergman, L. Cordier, and J.-P. Brancher. Optimal rotary control of the cylinder wake using POD reduced-order model. *Phys. Fluids*, 17:305–314, 2006.

[13] A. Bers. *Space-time evolution of plasma instabilities-absolute and convective*. North-Holland, 1983.

[14] F. P. Bertolotti, T. Herbert, and P. R. Spalart. Linear and nonlinear stability of the Blasius boundary layer. *J. Fluid Mech.*, 242:441–474, 1992.

[15] K. A. Bishop, J. E. Ffowcs Williams, and W. Smith. On the noise sources of the unsupressed high-speed jet. *J. Fluid Mech.*, 50:21–31, 1971.

[16] A. M. Blackburn, D. Barkley, and S. Sherwin. Convective instability and transient growth in flow over a backward-facing step. *J. Fluid Mech.*, 603:271–304, 2008.

[17] C. Bogey. *Calcul direct du bruit aérodynamique et validation de modèles acoustiques hybrides*. PhD thesis, Ecole centrale de Lyon, 2000.

[18] C. Bogey and C. Bailly. A family of low dispersive and low dissipative explicit schemes for flow and noise computations. *J. Comput. Phys*, 194:194–214, 2004.

[19] C. Bogey and C. Bailly. Investigation of downstream and sideline subsonic jet noise using large eddy simulation. *Theor. Comp. Fluid Dyn.*, 20(1):23–40, 2006.

[20] C. Bogey, C. Bailly, and D. Juvé. Numerical simulation of sound generated by vortex pairing in a mixing layer. *AIAA Journal*, 38(12):2210–2218, 2000.

[21] M. Bouthier. Stabilité linéaire des écoulements presque parallèles. *J. Méc*, 11:599–621, 19762.

[22] J. Bridges and F. Hussain. Direct evaluation of aeroacoustic theory in a jet. *J. Fluid Mech.*, 240:469–501, 1992.

[23] R. J. Briggs. *Electron-Stream interaction with Plasmas*. MIT Press, 1964.

[24] F. K. Browand and P. D. Weidman. Large scales in the developing mixing layer. *J. Fluid Mech.*, 76(1):127–144, 1976.

[25] G. L. Brown and A. Roshko. On density effects and large structure in turbulent mixing layers. *J. Fluid Mech.*, 64:775–816, 1974.

[26] L. C. Cheung and S. K. Lele. Linear and nonlinear processes in two-dimensional mixing layer dynamics and sound generation. *J. Fluid Mech.*, 625:321–351, 2009.

[27] J.-M. Chomaz. Transition to turbulence in open flows: what linear and fully nonlinear local and global theories tell us. *Eur. J. Mech. B/Fluids*, (23):385–399, 2004.

[28] J.-M. Chomaz. Global instabilities in spatially developing flows: Non-normality and nonlinearity. *Annu. Rev. Fluid Mech.*, 37:357–392, 2005.

[29] J.-M. Chomaz, P. Huerre, and L. M. Redekopp. A frequency selection criterion in spatially developing flows. *Study In Applied Mathematics.*, 84:119–144, 1991.

[30] T. Colonius, SK. Lele, and P. Moin. Sound generation in a mixing layer. *J. Fluid Mech.*, 330:2761–2778, 1997.

[31] C. Cossu and J-M. Chomaz. Global measures of local convective instabilities. *Phys. Rev. Lett.*, 78(23):4387–4390, 1997.

[32] D. G. Crighton and M. Gaster. Stability of slowly diverging flow. *J. Fluid Mech.*, 77:397–413, 1976.

[33] W. O. Criminale, T. L. Jackson, and R. D. Joslin. *Theory and compressible of hydrodynamic stability.* Cambridge University Press, 2003.

[34] S. C. Crow and F. H. Champagne. Orderly structure in jet turbulence. *J. Fluid Mech.*, 48:547–591, 1971.

[35] N. Curle. The influence of solid boundaries upon aerodynamic sound. *Proc. R. Soc. Lond.*, A 231:505–514, 1955.

[36] M. J. Day, N. N. Mansour, and W. C. Reynolds. Nonlinear stability and structure of compressible reacting mixing layers. *J. Fluid Mech.*, 446:375–408, 2001.

[37] P. G. Drazin and W.H. Reid. *Hydrodynamic Stability.* Cambridge University Press, 1981.

[38] U. Ehrenstein, P.-Y. Passaggia, and F. Gallaire. Control of a separated boundary layer: reduced-order modeling using global modes revisited. *Theor. Comp. Fluid Dyn.*, 25(1):195–207, 2011.

[39] J. B. Freund, S. K. Lele, and P. Moin. Numerical simulation of a Mach 1.92 turbulent jet and its sound field. *AIAA J.*, 38(11):2023–2031, 2000.

[40] P; Freymuth. On transition in a separated laminar boundary layer. *J. Fluid Mech.*, 25:683–704, 1966.

[41] M. Gaster, E. Kit, and I. Wygnanski. Large scale structures in a forced turbulent mixing layer. *J. Fluid Mech.*, 150:23–39, 1985.

[42] X. Gloerfelt. *Bruit rayonné par un écoulement affleurant une cavité: simulaion aéroacoustique directe et application de méthodes intégrales.* PhD thesis, Ecole centrale de Lyon, 2001.

[43] X. Gloerfelt. Compressible proper orthogonal decomposition/Galerkin reduced-order model of self-sustained oscillations in a cavity. *Phys. Fluids*, (115105), 2008.

[44] X. Gloerfelt, C. Bailly, and D. Juvé. Direct computation of the noise radiated by a subsonic cavity flow and application of integral methods. *J. Sound Vib.*, 2003.

[45] X. Gloerfelt and T. Le Garrec. Generation of inflow turbulence for aeroacoustic applications. 14th AIAA/CEAS Aeroacoustics Conference, 5-7 May 2008, Vancouver, Canada, 2008.

[46] X. Gloerfelt and P. Lafon. Direct computation of the noise induced by a turbulent flow though a diaphragm in a duct at low mach number. *Comput. Fluids*, 37:388–401, 2008.

[47] M. E. Goldstein. *Aeroacoustics*. 1976.

[48] Y. P. Guo. Applications of the Ffowcs Williams-Hawkings equations to two-dimensional problems. *J. Fluid Mech.*, 403:201–221, 2000.

[49] C. J. Heaton, J. W. Nichols, and P. J. Schmid. Global linear stability of the non-parallel Batchelor vortex. *J. Fluid Mech.*, 629:139–160, 2009.

[50] T. Herbert and F. P. Bertolotti. Stability analysis of nonparallel boundary layers. *Bull. Am. Phys. Soc.*, 32(2079), 1987.

[51] C. M. Ho and L. S. Huang. Subharmonics and vortex merging in mixing layers. *J. Fluid Mech.*, 119:443–473, 1982.

[52] C. M. Ho and P. Huerre. Perturbed free shear layers. *Annu. Rev. Fluid Mech.*, 16:365–424, 1984.

[53] P. Holmes, J.L. Lumley, and G. Berkooz. *Turbulence, Coherent structures, Dynamical systems and symmetry*. Cambridge University Press, 1996.

[54] P. Huerre, G. K. Batchelor, H. K. Moffatt, and M. G. Worster, editors. *Open shear flow instabilities*. Cambridge University Press, 2000.

[55] P. Huerre and D. G. Crighton. Sound generation by instability waves in a low mach number jet. *AIAA paper*, pages 83–0661, 1983.

[56] P. Huerre and P. A. Monkewitz. Absolute and convective instabilities in free shear layers. *J. Fluid Mech.*, 159:151–168, 1985.

[57] P. Huerre and P. A. Monkewitz. Local and global instabilities in spatially developing flows. *Annu. Rev. Fluid Mech.*, 22:473–537, 1990.

[58] T. L. Jackson and C. E. Grosch. Inviscid spatial stability of a compressible mixing layer. *J. Fluid Mech.*, 208:609–637, 1989.

[59] J. Jeong and F. Hussain. On the identification of a vortex. *J. Fluid Mech.*, 285:69–74, 1995.

[60] R. E. Kelly. On the stability of an inviscid shear layer which is periodic in space and time. *J. Fluid Mech.*, 27:657–689, 1967.

[61] V. Kibens. Discrete noise spectrum generated by an acoustically excited jet. *AIAA J.*, 18:434–441, 1980.

[62] A. Kierkegaard, E. Åkervik, G. Efraimsson, and D. S. Henningson. Flow field eigenmode decomposition in aeroacoustics. *Comput. Fluids*, 37:360–368, 2008.

[63] J. Laufer and T. Yen. Noise generation by low-Mach-number jets. *J. Fluid Mech.*, 134:1–31, 1983.

[64] L. Lesshafft. *Nonlinear global modes and sound generation in hot jets.* PhD thesis, Ecole polytechnique, 2006.

[65] M. J. Lighthill. On sound generated aerodynamically i. general theory. *Proc. R. Soc. Lond.*, A 211:564–587, 1952.

[66] M. J. Lighthill. On sound generated aerodynamically i. turbulence as a source of sound. *Proc. R. Soc. Lond.*, A 222:1–32, 1954.

[67] M. J. Lighthill. Report on the final panel discussion on computational aeroacoustics. *ICASE Rep.*, pages 92–53, 1992.

[68] G. M. Lilley. On the noise from jets. *AGARD*, CP-131, 1974.

[69] C. C. Lin. *The theory of hydrodynamic Stability.* Cambridge University Press, 1955.

[70] J. T. C. Liu. Developing large-scale wavelike eddies and the near jet noise field. *J. Fluid Mech.*, 62:437–464, 1974.

[71] D. P. Lockard. An efficient, two-dimensional implementation of Ffowcs Williams and Hawkings equations. *J. Sound Vib.*, 299 (4):897–911, 2000.

[72] J.L. Lumley. *Stochastic Tools in Turbulence.* Academic Press, 1970.

[73] I. Mezic. Spectral properties of dynamical systems, model reduction and decompositions. *Nonlinear Dyn.*, 41:309–325, 2005.

[74] A. Michalke. On the inviscid instability of the hyberbolic tangent velocity profile. *J. Fluid Mech.*, 19:543–556, 1964.

[75] A. Michalke. Vortex formation in a free boundary layer according to stability theory. *J. Fluid Mech.*, 22:371–383, 1965a.

[76] A. Michalke. On spatially growing disturbance in an inviscid shear layer. *J. Fluid Mech.*, 23:521–544, 1965b.

[77] B. E. Mitchell, S. K. Lele, and P. Moin. Direct computation of the sound from a compressible co-rotating vortex pair. *J. Fluid Mech.*, 285:181–202, 1995.

[78] B. E. Mitchell, S. K. Lele, and P. Moin. Direct computation of Mach wave radiation in an axisymmetric supersonic jet. *AIAA Journal*, 35(10):1574–1580, 1997.

[79] P. A. Monkewitz and P. Huerre. The influence of the velocity ratio on the spatial instability of mixing layers. *Phys. Fluids*, 25:1137–1143, 1982.

[80] P. A. Monkewitz, P. Huerre, and J.-M. Chomaz. Global linear stability analysis of weakly non-parallel shear flows. *J. Fluid Mech.*, 251:1–20, 1993.

[81] A. Monokrousos, E. Åkervik, L. Brandt, and D. S. Henningson. Input–output analysis, model reduction and control design of the flat-plate boundary layer. *J. Fluid Mech.*, 620:263–298, 2009a.

[82] C. J. Moore. The role of shear-layer instability waves in jet exhaust noise. *J. Fluid Mech.*, 80(2):321–367, 1977.

[83] P. J. Morris, L. N. Long, A. Bangalore, and Q. Wang. A parallel three-dimensional computational aeroacoustics method using nonlinear disturbance equations. *J. Comput. Phys*, 133:56–78, 1997.

[84] P. J. Morris, L. N. Long, and T. E. Scheidegger. Parallel computations of high speed jet noise. Greater Seattle, WA, 10-12 May 1999. 5th AIAA/CEAS Aeroacoustics Conference, AIAA Paper.

[85] J. W. Nichols and S. K. Lele. Global modes and transient response of a cold supersonic jet. *J. Fluid Mech.*, 669:225–241, 2011.

[86] B. Noack, M. Schlegel, B. Ahlborn, G. Mutschke, M. Morzynski, P. Comte, and G. Tadmor. A finite-time thermodynamics formalism for unsteady flows. *J. Non-Equilib. Thermodyn.*, 33:103–148, 2008.

[87] B. R. Noack, K. Afanasiev, M. Morzynski, G. Tadmor, and F. Thiele. A hierarchy of low-dimensional models for the transient and post-transient cylinder wake. *J. Fluid Mech.*, 497:335–363, 2003.

[88] D. Papamoschou and A. Roshko. The compressible turbulent shear layer. *J. Fluid Mech.*, 197:453–477, 1988.

[89] P.-Y. Passaggia, U. Ehrenstein, and F. Gallaire. Réduction de modèles et contrôle d'une couche limite décollée. 19ème Congrès Français de Mécanique, 24-18 août 2009, Marseille, France, 2009.

[90] O. M. Phillips. On the generation of sound by supersonic turbulent shear layer. *J. Fluid Mech.*, 9:1–28, 1960.

[91] B. Pier. On the frequency selection of finite-amplitude vortex shedding in the cylinder wake. *J. Fluid Mech.*, 458:407–417, 2002.

[92] A. Powell. Theory of vortex sound. *J. Acoust. Soc. Am.,*, 36(1):179–195, 1964.

[93] M. Rajaee, S. Karlsson, and L. Sirovich. Low-dimensional description of free-shear-flow coherent structures and their dynamical behaviour. *J. Fluid Mech.*, 258:1–29, 1994.

[94] J. J. Riley and R. W. Metcalfe. Direct numerical simulation of a perturbed turbulent mixing layer. *AIAA Paper 80-0274*, 1980.

[95] C. W. Rowley, T. Colonius, and A. J. Basu. On self-sustained oscillations in two-dimensional compressible flow over rectangular cavities. *J. Fluid Mech.*, 455:315–346, 2002.

[96] C. W. Rowley, T. Colonius, and R. M. Murray. Model reduction for compressible flows using POD and Galerkin projection. *Physica D*, 189:115–129, 2004.

[97] C. W. Rowley, I. Mezic, S. Bagheri, P. Schlatter, and D.S. Henningson. Spectral analysis of nonlinear flows. *J. Fluid Mech.*, 641:1–13, 2009.

[98] P. Schmid, L. Li, M. P. Juniper, and O. Pust. Applications of the dynamic mode decomposition. *Theor. Comp. Fluid Dyn.*, 25:249–259, 2011.

[99] P. J. Schmid. Nonmodal stability theory. *Annu. Rev. Fluid Mech.*, 39:129–162, 2007.

[100] P. J. Schmid. Dynamic mode decomposition of numerical and experimental data. *J. Fluid Mech.*, 656:5–28, 2010.

[101] P. J. Schmid and J. L. Sesterhenn. Dynamic mode decomposition of numerical and experimental data. In Bull. Amer. Phys. Soc., 61st APS meeting, p. 208. San Antonio, Texas, USA, 2008.

[102] G. B. Schubauer and H.K. Skramstad. Laminar boundary layer oscillations and transition on flat plate. Technical Report 909, NACA, 1948.

[103] D. Sipp and A. Lebedev. Global stability of base and mean flows: a general approach and its applications to cylinder and open cavity flows. *J. Fluid Mech.*, 593:333–358, 2007.

[104] L. Sirovich. Turbulence and the dynamics of coherent structures, parts i–iii. *Q. Appl. Math.*, XLV (3):561–590, 1987.

[105] G. Song, X. Gloerfelt, and J.-C. Robinet. Sound generation in coflow and counterflow mixing layers. 10ème Congrès Français d'Acoustique, 12-16 avril 2010, Lyon, France.

[106] B. Spagnoli and C. Airiau. Adjoint analysis for noise control in a two-dimensional compressible mixing layer. *Comput. Fluids*, 37:475–486, 2008.

[107] S. Stanley and S. Sarkar. Simulations of spatially developing two-dimensional shear layers and jets. *Theor. Comp. Fluid Dyn.*, 9(2):121–147, 1997.

[108] C. K. W. Tam. Supersonic jet noise. *Annu. Rev. Fluid Mech.*, 27:17–43, 1995.

[109] C. K. W. Tam. Computational aeroacoustics: An overview of computational challenges and applications. *International Journal of Computational Fluid Dynamics*, 18(6):547–567, 2004.

[110] C. K. W. Tam and D. Burton. Sound generation by instability waves of supersonic flows, part 1. two dimensional mixing layers. *J. Fluid Mech.*, 138:249–271, 1984a.

[111] C. K. W. Tam and D. Burton. Sound generation by instability waves of supersonic flows, part 2. axisymmetric jets. *J. Fluid Mech.*, 138:273–295, 1984b.

[112] C. K. W. Tam and Z. Dong. Radiation and outflow boundary conditions for direct computation of acoustic and flow disturbances in a nonuniform mean flow. *J. Comput. Phys*, 4(2):175–201, 1996.

[113] C. K. W. Tam and P. J. Morris. The radiation of sound by the instability waves of a compressible plane turbulent shear layer. *J. Fluid Mech.*, 98:348–381, 1980.

[114] C. K. W. Tam and J. C. Webb. Dispersion-relation-preserving finite difference schemes for computational acoustics. *J. Comput. Phys*, 107(2):262–281, 1993.

[115] N. Trefethen and M. Embree. *Spectra and pseudospectra: the behaviour of nonnormal matrices and operators*. Princeton University Press, princeton edition, 2005.

[116] L. S. Tuckerman and D. Barkley. *Bifurcation analysis for timesteppers. In Numerical methods for bifurcation problems and large-scale dynamical systems*. Springer, 2000.

[117] L. Ukeiley, L. Cordier, R. Manceau, J. Delville, M. Glause, and J. P. Bonnet. Examination of large-scale structures in a turbulent plane mixing layer. part 2. dynamical systems model. *J. Fluid Mech.*, 441:67–108, 2001.

[118] M. Wei and J. B. Freund. A noise-controlled free shear flow. *J. Fluid Mech.*, 546:123–152, 2006.

[119] J. E. Ffowcs Williams and D. L. Hawkings. Sound generated by turbulence and surfaces in arbitrary motion. *Philosophical Transactions of the Royal Society*, A264 (1151):321–342, 1969.

[120] J. E. Ffowcs Williams and A. J. Kempton. The noise from the large scale structure of a jet. *J. Fluid Mech.*, 84:673–694, 1978.

[121] C. D. Winant and F. K. Browand. Vortex pairing, the mechanism of turbulent mixing-layer growth at moderate reynolds number. *J. Fluid Mech.*, 63:237–255, 1974.

Rayonnement acoustique des structures cohérentes d'une couche de mélange

Résumé : Une couche de mélange est généralement considérée comme un prototype d'écoulements libres cisaillés qui se rencontre au sein des nombreux phénomènes naturels et applications industrielles. Le fort développement des méthodes aéroacoustiques, notamment grâce aux progrès des simulations numériques, a permis d'identifier les structures cohérentes qui se développent dans l'écoulement comme les principales sources de bruit. En particulier, l'analyse des instabilités qui se développent dans l'écoulement permet de comprendre la dynamique de ces structures cohérentes. Dans ce cadre, nous proposons de réaliser à travers ce mémoire une analyse de stabilité linéaire globale, afin de comprendre l'émergence de fréquences fondamentales, ainsi qu'une décomposition modale linéaire et non-linéaire, afin de caractériser les structures cohérentes essentiellement responsables du rayonnement acoustique. En outre, nous proposons de développer les méthodes de stabilité linéaire globale en régime compressible ainsi qu'une technique de calcul de structures cohérentes dans le régime non-linéaire basée sur la méthode « DMD ». De tels outils d'analyse sont validés et illustrés sur une configuration académique d'une couche de mélange à co-courant, de type d'amplificateur de bruit. Notamment, deux choix sont adaptés, un simple cas où une seule source est impliquée dans le rayonnement acoustique et un cas plus complexe où deux sources sont présentes. Ainsi il est montré que les analyses DMD temporelle et spatiale sont capables de décrire le comportement des structures cohérentes en champ proche et les caractéristiques des ondes acoustiques en champ lointain. Enfin, les méthodes de décomposition modale s'avèrent être une réduction de modèle pertinente, dans l'objectif d'un contrôle efficace.

Mots clés : stabilité linéaire globale, simulation numérique pour l'aéroacoustique, décomposition modale, réduction modèle.

Sound generation by coherent structures in mixing layers

Abstract : A mixing layer is generally considered as a prototype of free shear flows which occur in a very broad spectrum of applications from natural phenomena to the engineering science. The increasing development of the aeroacoustics, more particularly thanks to the progress in numerical simulations, has allowed to identify the coherent structures which evolve in the flow as the main sound sources. Furthermore, the emergence of the instability waves taking the form of the coherent structures can be characterized by the stability analysis. In this context, we propose through this work to perform a global stability analysis, in order to understand the emergence of fundamental frequencies, as well as a modal decomposition within both a linear and nonlinear framework, to characterize the coherent structures primarily responsible for the sound generation. In particular, we propose to develop the methods of the global stability with respect to the compressible flows as well as a technique of calculation of coherent structures applied to the nonlinear regimes based on the DMD method. Such analysis tools are validated and illustrated on an academic configuration of a co-flowing mixing layer, a typical noise amplifier, from a simple case where a single source is implicated in the acoustic radiation to a more complex case where two sources are present. Both the temporal and spatial DMD are shown capable of describing the characteristics of the coherent structures in the near field and the behaviour of the acoustic waves in the far field. Finally, the methods of the modal decomposition have proven themselves as a relevant model reduction aiming at designing an efficient control strategy.

Keywords : global linear stability, computational aeroacoustics, modal decomposition, model reduction.

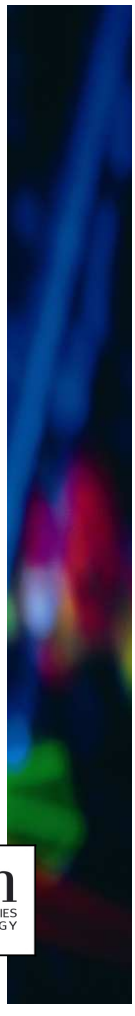

ARTS ET MÉTIERS ParisTech

ParisTech
INSTITUT DES SCIENCES ET TECHNOLOGIES
PARIS INSTITUTE OF TECHNOLOGY